Title
Hyperpolarized Xenon Magnetic Resonance Imaging of Combustion Processes

Author
Mustonen, J. Peter

Publication Date
2012

Hyperpolarized Xenon Magnetic Resonance Imaging of Combustion Processes

by

J. Peter Mustonen

A dissertation submitted in partial satisfaction of the
requirements for the degree of
Doctor of Philosophy

in

Chemistry

in the

GRADUATE DIVISION
of the
UNIVERSITY OF CALIFORNIA, BERKELEY

Committee in charge:
Professor Alexander Pines, Chair
Professor David E. Wemmer
Professor Dmitry Budker

Spring 2012

Hyperpolarized Xenon Magnetic Resonance Imaging of Combustion Processes

Abstract

Hyperpolarized Xenon Magnetic Resonance Imaging of Combustion Processes

by

J. Peter Mustonen

Doctor of Philosophy in Chemistry

University of California, Berkeley

Professor Alexander Pines, Chair

There is considerable interest in new methods to probe the chemistry and thermodynamics of enclosed combustion processes. Hyperpolarized xenon gas magnetic resonance imaging enables sensitive and noninvasive analysis of chemical composition and velocity within enclosed and opaque samples. By taking advantage of both the temperature sensitivity of the chemical shift as well as the inertness of xenon-129, temperature and velocity distribution images of an enclosed flame can be acquired. Previous attempts to analyze high-temperature combustion reactions using nuclear magnetic resonance employed two-dimensional exchange spectroscopy of hyperpolarized xenon and proton single-point imaging. In the present study, a homebuilt, water-cooled probe was fabricated, including electronics that are able to withstand high temperatures (approaching 2000 K). Hyperpolarized xenon is premixed with a combustible gas (methane or dimethyl ether) and meets with pure oxygen at an enclosed diffusion flame centered within a 15-mm (diameter) by 25.4-mm (height) insulated coil. A spin echo pulse sequence with velocity and acceleration compensated phase-encodes, is used to generate temperature-weighted, three-dimensional chemical shift images as well as velocity maps of the flame region. This technique can be applied to studying confined combustion processes such as microturbine engines on microelectromechanical systems devices.

To my parents,
John and Janet Mustonen,
for their support throughout my life.

Contents

List of Figures

List of Tables

List of Symbols

Abbreviations

1D	One-Dimensional
2D	Two-Dimensional
3D	Three-Dimensional
4D	Four-Dimensional
ACQ	Acquisition
AM	Atomic Magnetometry
CFD	Computational Fluid Dynamics
CSI	Chemical Shift Imaging
DAQ	Data Acquisition
DECC	Digital Eddy Current Correction
DME	Dimethyl Ether
DNP	Dynamic Nuclear Polarization
ENC	Experimental Nuclear Magnetic Resonance Conference
EXSY	Exchange Spectroscopy
FID	Free Induction Decay
FLIR	Forward Looking Infrared
FFT	Fast Fourier Transform
FOV	Field of View
GMN	Gradient Moment Nulling
GRAD	Gradient
HP	Hyperpolarized
HVAC	Heating, Ventilation, and Air Conditioning
ID	Inside Diameter
LBNL	Lawrence Berkeley National Laboratory
LED	Light-Emitting Diode
MATLAB	MathWorks' Matrix Laboratory software
MEMS	Microelectromechanical Systems
MFC	Mass Flow Controller
MRI	Magnetic Resonance Imaging
NA	Natural Abundance

NMR	Nuclear Magnetic Resonance
NV	Nitrogen Vacancy
OD	Outside Diameter
PFA	Perfluoroalkoxy
QB3	California Institute for Quantitative Biosciences
RF	Radio Frequency
RT	Room Temperature ($\approx 20\,^{\circ}\mathrm{C}$)
RTD	Resistance Temperature Detector
SCFH	Standard Cubic Feet per Hour
SCFM	Cubic Feet per Minute
SEOP	Spin-Exchange Optical Pumping
SI	International System of Units
SLPM	Standard Liters Per Minute
SNR	Signal-to-Noise Ratio
SPRITE	Single-Point Ramped Imaging with T_1 Enhancement
TE	Echo Time
THEIC	Tris-(2-Hydroxyethyl) Isocyanurate
TMS	Tetramethylsilane
TR	Repetition Time
UCB	University of California, Berkeley
VENC	Aliasing Velocity Parameter for Velocity-Encoding
VnmrJ	Varian's Java-based NMR acquisition and processing software
ZF	Zero-Filled

Symbols

a	complex signal amplitude
a_0	initial acceleration
$\|a\|e^{i\phi}$	complex signal of intensity $\|a\|$ and phase ϕ
A	signed gradient waveform area
B^0	magnitude of main field
C_M	value of matching capacitor
C_T	value of tuning capacitor
δ	chemical shift
δ_i	spatial resolution in i-dimension
δ_ZF	spatial resolution between zero-filled points
e	mathematical constant, $e = 2.71828...$
E	energy
f	frequency (Hz)
FOV_i	field of view in i^th spatial dimension
ϕ	radio frequency phase
ϕ_rec	combined phase shift of NMR signal
G	peak gradient strength
G_i	peak gradient strength of the i^th gradient lobe
γ	gyromagnetic ratio
γ'	shielded gyromagnetic ratio
i	squrare root of -1; index
I	ground-state nuclear spin
I_z	component of spin angular momentum parallel to main field
k	k-space
k_f	frequency k-space in spectroscopic imaging (t)
k_i	k-space dimension corresponding with i^th spatial dimension
L	inductance
λ	decay rate constant, T_2^{-1}
m	gradient moment
m_n	n^th gradient moment
$m(x, y)$	spin density at point (x, y)
M_0	magnitude of equilibrium magnetization
M_{xy}	transverse magnetization
M_z	longitudinal magnetization
μ	magnetic moment
μ_z	component of magnetic moment parallel to main field
n	index
N_pe	number of phase-encodes
N_ro	number of readout samples
N_ZF	number of points in zero-filled space

$\mathfrak{N}$	number of transients
ν	frequency
P	pressure
π	mathematical constant, $\pi = 3.14159...$
$(\pi/2)_\phi$	pulse flip of angle $\pi/2$ and phase ϕ
π_ϕ	pulse flip of angle π and phase ϕ
θ	angle
r	radius
r, θ	spatial coordinates in polar coordinate system
ρ	density
$s(t)$	complex NMR/MRI signal
s_{noise}	component of the signal due to noise
σ	chemical shielding factor; standard deviation
σ'	magnetic shielding correction
σ_n	$(n+1)^{\text{th}}$ virial coefficient of the chemical shift
σ_{ref}	shielding factor of reference sample
σ_{noise}	root-mean-square noise
t	time coordinate
T	temperature; gradient lobe length; variable delay
T_1	spin-lattice relaxation time constant
T_2	spin-spin relaxation time constant
T_2^*	effective spin-spin relaxation time constant, $T_2^* \leq T_2$
τ	$T - 300$ K
v	velocity
v_0	initial velocity
v_i	velocity component along i^{th} spatial dimension
V	volume
ω	angular frequency
ω^0	precession (Larmor) frequency
ω_{osc}	oscillation frequency of tuned circuit in probe
ω_{ref}	spectrometer reference frequency
ω^0_{ref}	Larmor frequency of reference sample
ω^0_{TMS}	TMS Larmor frequency (^{1}H, ^{13}C reference)
$\omega^0_{\text{Xe(ref)}}$	RT HP xenon gas (mixture) Larmor frequency (^{129}Xe reference)
Ω^0	Larmor frequency relative to spectrometer reference
x, y	spatial coordinates in Cartesian coordinate system
x_0	initial position
z	spatial coordinate, usually in the direction of the main magnetic field
Z	atomic number

NOTE: Some naming conventions from Keeler [37], Levitt [39], and Nishimura [46] texts.

VnmrJ Variables & Commands [see Appendix C.1]

at	acquisition time (ms)
d1	recycle delay (s)
dres	measure linewidth and digital resolution (Hz)
enct	encoding time
gacrt	position-encoding gradient step time (µs)
fid	FID file
gaci	peak DAQ value for first lobe of position-encoding gradient in i-dimension
gact	position-encoding lobe duration (µs)
gain	receiver gain (dB)
gems	gradient echo multi slice (pulse sequence)
getsn	get signal-to-noise estimate of a spectrum
gvrt	velocity-encoding gradient step time (µs)
gvt	velocity-encoding lobe duration (µs)
gvi	peak DAQ value for first lobe of velocity-encoding gradient in i-dimension
np	number of data points
nt	number of transients
procpar	parameter file
pw	pulsewidth (µs)
sfrq	transmitter frequency of observe nucleus (MHz)
spuls	single pulse (pulse sequence)
sw	spectral width in directly detected dimension (Hz)
tof	frequency offset for observe transmitter (Hz)
tpwr	transmitter power (dB)
tr	repetition time (ms)

MATLAB Variables [see Appendix C.4]

csimg	CSI data array
img	density data array
min_angle	minimum phase difference
max_angle	maximum phase difference
NaN	not a number
phase_angle	phase difference array
plane	dimensionality of the data
velocity	velocity data array
velplane	velocity dimension
xpos	x-position
ypos	y-position
zpos	z-position

Physical Constants

From CODATA [42]

c	speed of light in vacuum, 2.99792458×10^{8} m s^{-1}
γ_{p}	proton gyromagnetic ratio, 267.5222099(70) rad MHz T^{-1}
$\gamma_{\mathrm{p}}/2\pi$	42.5774821(11) MHz T^{-1}
γ'_{p}	shielded proton gyromagnetic ratio, 267.5153362(73) rad MHz T^{-1}
$\gamma'_{\mathrm{p}}/2\pi$	42.5763881(12) MHz T^{-1}
h	Planck constant, $6.62606896(33) \times 10^{-34}$ J s
$\hbar$	$\hbar = h/2\pi$, $1.054571628(53) \times 10^{-34}$ J s
k_{B}	Boltzmann constant, $1.3806504(24) \times 10^{-23}$ J K^{-1}
μ_{d}	deuteron magnetic moment, $0.433073465(11) \times 10^{-26}$ J T^{-1}
$\mu_{\mathrm{d}}/\mu_{\mathrm{N}}$	deuteron magnetic moment to nuclear magneton ratio, 0.8574382308(72)
$\mu_{\mathrm{d}}/\mu_{\mathrm{p}}$	deuteron-proton magnetic moment ratio, 0.3070122070(24)
μ_{N}	nuclear magneton, $5.05078324(13) \times 10^{-27}$ J T^{-1}
μ_{N}/h	nuclear magneton in MHz/T, 7.62259384(19) MHz T^{-1}
μ_{p}	proton magnetic moment, $1.410606662(37) \times 10^{-26}$ J T^{-1}
$\mu_{\mathrm{p}}/\mu_{\mathrm{N}}$	proton magnetic moment to nuclear magneton ratio, 2.792847356(23)
σ'_{p}	proton magnetic shielding correction, $25.694(14) \times 10^{-6}$

Nuclear Spin [61]

I_{d}	deuteron ground-state nuclear spin, 1
I_{p}	proton ground-state nuclear spin, 1/2
$I_{^{85}\mathrm{Rb}}$	rubidium-85 ground-state nuclear spin, 5/2
$I_{^{87}\mathrm{Rb}}$	rubidium-87 ground-state nuclear spin, 3/2
$I_{^{129}\mathrm{Xe}}$	xenon-129 ground-state nuclear spin, 1/2
$I_{^{131}\mathrm{Xe}}$	xenon-131 ground-state nuclear spin, 3/2

Natural Abundances [55]

$\mathrm{NA}_{^{85}\mathrm{Rb}}$	rubidium-85 natural abundance, 72.17(2)%
$\mathrm{NA}_{^{87}\mathrm{Rb}}$	rubidium-87 natural abundance, 27.83(2)%
$\mathrm{NA}_{^{129}\mathrm{Xe}}$	xenon-129 natural abundance, 26.44(24)%
$\mathrm{NA}_{^{131}\mathrm{Xe}}$	xenon-131 natural abundance, 21.18(3)%

Xenon-129 [see Appendix B.1]

$\gamma_{^{129}\mathrm{Xe}}$	xenon-129 gyromagnetic ratio, $-74.5211(8)$ rad MHz T^{-1}
$\gamma_{^{129}\mathrm{Xe}}/2\pi$	$-11.8604(1)$ MHz T^{-1}
$\gamma'_{^{129}\mathrm{Xe}}$	shielded xenon-129 gyromagnetic ratio, $-73.9963(8)$ rad MHz T^{-1}
$\gamma'_{^{129}\mathrm{Xe}}/2\pi$	$-11.7769(1)$ MHz T^{-1}
$\mu_{^{129}\mathrm{Xe}}/\mu_{\mathrm{N}}$	xenon-129 magnetic moment to nuclear magneton ratio, $-0.777976(9)$
$\mu_{^{129}\mathrm{Xe}}/\mu_{\mathrm{p}}$	xenon-129 to proton magnetic moment ratio, $-0.278560(3)$
$\mu'_{^{129}\mathrm{Xe}}/\mu_{\mathrm{N}}$	shielded xenon-129 magnetic moment to nuclear magneton ratio, $-0.772498(9)$
$\mu'_{^{129}\mathrm{Xe}}/\mu_{\mathrm{p}}$	shielded xenon-129 to proton magnetic moment ratio, $-0.276599(3)$

Units

amg	amagat, 1 amg = 2.6867774×10^{25} m^{-3}
atm	atmosphere
AWG	American Wire Gauge
°C	degree Celsius
DAQ	DAQ unit, a signed short integer
dB	decibel
F	farad
G	gauss, 1 G = 10^{-4} T
Hz	hertz, cycles per second
″	inch
K	degree kelvin
L	liter
m	meter
min	minute
Pa	pascal
ppm	part per million
psia	pound per square inch actual, psia = psig + 14.696
psig	pound per square inch gauge, psig = psia − 14.696
rad	radian
s	second
SCFH	standard cubic foot per hour
SCFM	standard cubic foot per minute
SLPM	standard liter per minute
T	tesla

SI Prefixes

M	10^{6}
k	10^{3}
c	10^{-2}
m	10^{-3}
µ	10^{-6}
n	10^{-9}
p	10^{-12}
f	10^{-15}

Flow Rates

1 SCFH = 0.4719474432 SLPM
1 SLPM ≈ 0.0353147 SCFM
1 SLPM ≈ 2.11888 SCFH
0.10 SCFH ≈ 0.047 SLPM
0.15 SCFH ≈ 0.071 SLPM
0.30 SCFH ≈ 0.142 SLPM
0.30 SLPM ≈ 0.636 SCFH

Frequencies

1 Hz	1 s^{-1}, 1 cycle = 1 s
10 Hz	10 s^{-1}, 1 cycle = 100 ms
100 Hz	100 s^{-1}, 1 cycle = 10 ms
1 kHz	1 ms^{-1}, 1 cycle = 1 ms
10 kHz	10 ms^{-1}, 1 cycle = 100 µs
100 kHz	100 ms^{-1}, 1 cycle = 10 µs
1 MHz	1 μs^{-1}, 1 cycle = 1 µs
10 MHz	10 μs^{-1}, 1 cycle = 100 ns
100 MHz	100 μs^{-1}, 1 cycle = 10 ns
110.6 MHz	110.6 μs^{-1}, 1 cycle ≈ 3.3 ns
300 MHz	300 μs^{-1}, 1 cycle ≈ 3.3 ns
400 MHz	400 μs^{-1}, 1 cycle = 2.5 ns
1 GHz	1 ns^{-1}, 1 cycle = 1 ns
2.87 GHz	2.87 ns^{-1}, 1 cycle ≈ 348 ps
10 GHz	10 ns^{-1}, 1 cycle = 100 ps
100 GHz	100 ns^{-1}, 1 cycle = 10 ps
1 THz	1 ps^{-1}, 1 cycle = 1 ps

Acknowledgments

I spent my entire life living in and around Boston, Massachusetts before moving out to Berkeley. I grew up in Walpole and went to Walpole High School before studying at Harvard University where I got my degree in biochemical sciences, while also performing research as an intern at Biopure Corp. I then spent five exciting years at TransForm Pharmaceuticals, Inc. in Lexington before heading to graduate school. Moving to Berkeley was a big change for me. Not only was I leaving my home, where my family and friends were, but also a great company and my beloved sports teams (my dad and I share Red Sox season tickets). However, the move to Berkeley felt right from the beginning, and the welcoming environment of the Pines Lab certainly made the transition easier.

The new class of graduate students joining Alex's lab with me was a big one, with Ngoc Do, Hattie Ring, Tom Teisseyre, Thomas Theis, and I, all becoming Pinenuts in the fall of 2007. I fondly remember our first year, getting up to speed on all things magnetic resonance, struggling through months of magnet duty, and helping to move the lab from the dungeon of Hildebrand Hall across University Drive to our new digs and natural light in QB3's Stanley Hall. We enjoyed our time together, working through problem sets in Prof. Steve Conolly's MRI class during the spring, and plowing through Malcolm Levitt's "Spin Dynamics" during the summer. In between we got to enjoy our first Experimental Nuclear Magnetic Resonance Conference, as the entire lab made the trip to Asilomar for the 49th ENC.

I would attend and enjoy three more ENCs during my tenure at Berkeley: the 50th anniversary at Asilomar, where Alex chaired the outstanding session "Beyond Nuclear Magnetic Resonance," which featured some of his brilliant friends, as well as the 51st and 52nd in Daytona Beach and Asilomar respectively. ENC was always a great time; Asilomar is beautiful and such a wonderful place to meet new scientists within our field. ENCs were also great opportunities to bond as a group. Spending a week with the other Pinenuts, often in close quarters and with plenty of beer and wine at the vendor suites, was always sure to generate some stories. I was also able to attend EUROMAR 2011 in Frankfurt, Germany, where the work presented in this dissertation won the EUROMAR Poster Prize.

The annual Pinenut ski trip tradition was started while I was at Berkeley. Tom Teisseyre and I (and later Hattie Ring) worked each year to set up a weekend for us all to take off right after Friday group meeting for the scenic beauty and excellent skiing at Lake Tahoe. Each of my last three years at Berkeley I was fortunate enough to get a student season pass to Kirkwood Mountain Resort, so I enjoyed skiing there as often as possible, usually with my friend Erik Hosler from the Leone Lab.

Us Pinenuts also spent a lot of time at trivia nights at Henry's, with our "Stache of the Titans" being very successful. Along with Paul Ganssle, Scott Seltzer, Dan Kennedy, and Claudia Avalos, we were able to make it to the final round in San Francisco and do quite well. We also had a very successful volleyball team led by Nick Graziani. When I joined the lab I was sad to hear that we did not have a softball team. I had been the captain of my softball team for five years at TransForm, and wanted to keep playing, so I joined up with a team of theoretical chemists including Keith Lawler, Westin Kurlancheek, Eric Sundstrom, and Greg Dallinger. This team was not very competitive, but it was a lot of fun, with many a late night spent at Kip's after the game. When I became the captain, I was able to merge the team with the group of Pinenuts who wanted to play softball.

I joined the Graduate Life Committee (GLC) in my first year and offered to help with ChemKeg, a Department of Chemistry tradition held every Friday afternoon. I became very involved with helping the student chairs of the GLC, Sarah Hubbard, and later Jordan Rose Figura, run the other social events as well, including the infamous College of Chemistry Holiday Parties. I later took over as student chair, and was able to extend the GLC's impact to academic matters as well as departmental recruiting. I would like to thank the faculty representatives on the GLC for their help over the years: Prof. Heino Nitsche, Prof. Judith Klinman, Prof. Jeff Long, and especially Prof. Phill Geissler and Dr. Michelle Douskey. Good luck to Allison Pymer as the new GLC student chair.

The work presented here could not have been successful without the assistance of undergraduate researcher Doug Shin, who made a huge impact on the project, notably with his skill in the machine shop. Good luck Doug at MIT, and I hope to see you around. I would also like to thank Nick Graziani and Xin Zhou for helping me get up to speed on hyperpolarized xenon, imaging, and MATLAB, and Thomas Theis for his help early on in the project.

Prior to the combustion project, I also worked on the "Phase 1" magnetometer with David Michalak, Chip Crawford, Marcus Donaldson, Hattie Ring, and Scott Seltzer, and I would like to thank them all for their help in understanding low-field magnetic resonance and optics. I would later return to low-field, working on the diamond nitrogen vacancy projects with David Trease, Chang Shin, Claudia Avalos, Daniel Kennedy, and Haijing Wang, and I thank them for making my work on this new and exciting project fulfilling.

I would like to thank all the other graduate students in the lab who I did not work directly with, but who were always supportive, great friends, and colleagues: John Franck, Scott Burt, Elad Harel, Jeff Paulsen, Nick Halpern-Manners, Tyler Meldrum, Monica Smith, Ngoc Do, Tom Teisseyre, Paul Ganssle, Matt Ramirez, John Blanchard, Dan Baum, Phuong Dao, Anna Parker, Emilee Sena, Clancy Slack, and Franz Schilling. Thanks also to our outstanding postdocs: Louis Bouchard, Leif Schroeder, Micah Ledbetter, Gwendel Kervern, Xi Meng, Todd Stevens, Mark Butler, Aleks Kijac, and Lindsay Sperling. I have also been able to see the outstanding contributions from Berkeley undergraduate researchers Rees Garmann, Sean Osterday, Misha Berger, and Jinny Sun.

A huge thanks to Prof. Alex Pines, Prof. Dima Budker, Prof. Dave Wemmer, and Dr. Vik Bajaj for their invaluable mentoring over the years and for continuing to ensure that the research performed in the lab is cutting-edge, exciting, well-funded, and successful. Special thanks to Alyse Jacobson for her help, advice, and conversation over the years. The group would not run so smoothly without her administrative efforts. Thanks also to Gail Odom for her assistance, and to Ditsa Pines for hosting entertaining Pinefests each autumn.

Berkeley would not have been as much fun without my friends Bogdan Negru & Christine Koh, Erik Hosler & Becca Stahl, Hattie & Andrew Ring, Tawnya & Jacob Flick, Thomas Theis & Courtney Rivard, Ian Ryu, and Geoff Feld among others. Thanks for all the fun times skiing at Tahoe, hiking and camping in Yosemite National Park, going to Cal football games, competing in "Iron Chef," learning to rock climb, playing tennis, sharing Sichuan food and dim sum, visiting wine country, etc. I will really miss you all!

Lastly I would like to thank my family for supporting me throughout my career as a scientist. They encouraged me to pursue an industrial scientific internship directly after high school, which ended up being an enriching four-year experience at Biopure during my years at Harvard. They also strongly supported my decision to come to Berkeley, even though it meant I would be 3,000 miles away from them. Fortunately, they were kind enough to come out to visit on several occasions and even dragged me along on trips to China and Yellowstone National Park. As much as I love the Bay Area, it has been tough to be so far away and I am looking forward to heading back to Boston for the next chapter in my life. Thanks for the memories Berkeley!

Chapter 1

Xenon-129 MRI of Combustion

1.1 Motivation

There is considerable interest in the development of new techniques for multidimensional *in situ* imaging of combustion reactions in traditional (macroscopic) and microfabricated combustion devices [18]. The ability to acquire spatial and temporal maps of reactant density, temperature, and flow velocity in flames would enable optimization of combustion parameters during development and in-line reaction monitoring of the final products. Nuclear magnetic resonance imaging (MRI), which can produce multidimensional, high-fidelity images noninvasively, is well-suited to this task, particularly since it allows imaging of inside of opaque vessels.

The signal intensity in nuclear magnetic resonance (NMR) is proportional to the nuclear spin density, and therefore magnetic resonance images are maps of local concentration of the nucleus of interest. The ^{129}Xe nucleus can be hyperpolarized (HP) by spin-exchange optical pumping [65], improving sensitivity by several orders of magnitude. The NMR chemical shift of ^{129}Xe is temperature-dependent [1, 34], and this property can be exploited by using chemical shift imaging (CSI) to generate qualitative temperature maps [56, 57]. Quantitative velocity information can also be encoded [28] using gradient pulses designed to sensitize the spin dynamics to velocity while simultaneously canceling the effects of acceleration [7]. Detection in MRI can also be performed remotely [43] and at low magnetic fields [68], enabling higher sensitivity, better spatial resolution, and portability.

1.1.1 Applications

The list of potential applications where MRI could make an impact on the analysis of combustion is extensive. The properties of interest in these systems include: concentration of reactants and products, temperature distribution, diffusion and mixing properties, and flow velocity. The applications where traditional analytical methods (Sections 1.1.2 and 1.1.3) are unsuitable are the best targets for study. This includes enclosed or confined combustion, where the reaction takes place within an opaque vessel that does not permit the passage of optical or mechanical probes. Microscale combustion systems, where high spatial resolution is paramount, and any system requiring three-dimensional (3D) imaging are also areas where MRI could improve upon the existing techniques. Some types of combustion that are of interest at the moment are smoldering combustion, catalytic combustion, analysis of fuel components, flames in microchannels, and microturbines designed for microelectromechanical systems (MEMS) devices.

Smoldering combustion analyses focus on the transition from a forward-moving smolder front to a flame [4]. Analysis of smoldering combustion using MRI could be possible if the flame front moved slowly enough to stay in the experimental field of view (FOV) during the acquisition time. MRI is a not an instantaneous measurement, and even low resolution images can take minutes to acquire; ideally not much should change during the acquisition. However, other techniques to study smoldering combustion, such as ultrasound [63], also require long scan times, and the methods for measuring temperature (visible imaging, infrared imaging, and thermocouples) are all limited to the surfaces. Flowing HP xenon through a smoldering reaction would enable imaging of the foam itself. The existing containment devices used to study smoldering combustion are metallic, and therefore unsuitable for high frequencies. They would require redesign in a non-conductive material for studies to move forward.

Catalytic oxidation is another area of study that includes pyrolysis for the production of nanostructures within flames [6]. This reaction takes place at high temperatures and requires third-generation synchrotron radiation for analysis due to the dilute growth conditions and rapid kinetics. A cheaper, noninvasive technique like MRI could enable more extensive multidimensional analyses of this process. MRI of catalysis on platinum or palladium catalysts would require remote or low field detection due to the presence of the metal structures.

The desire for smaller and more efficient devices for portable power generation engines has driven investigations into hydrogen combustion at the microscale [19]. Hydrogen was chosen due to its low adiabatic flame temperature (< 1500 K), low equivalence ratio [18], and fast reaction rate. This has led to the development of millimeter-scale silicon microturbine engines [20] designed to power MEMS devices. The dynamics of hydrogen flames in microchannels have also been investigated [52]. MRI could impact the investigation into the effect of microchannel walls on heat loss and flame propagation within these opaque devices. At the meso-scale, surface heating and internal cooling effects in composite airfoils and turbines are currently studied using particle velocimetry and water MRI [17], neither of which allow *in situ* analysis. By flowing HP xenon as a component of the reaction mixture in these devices, information about the flow velocity and surface interactions can be obtained, and their non-metallic construction facilitates MRI analysis at high field.

The proof of concept system chosen for analysis with HP xenon MRI was an open diffusion flame. This system, while simple to set up, provides a wealth of information. The visualization of fuel components and products, the mixing of fuel and oxidizer at the flame front, the mapping of the temperature distribution, and the quantification of flow velocity are all possible with this system. By separating the flame from the coil by an opaque barrier, the imaging of confined combustion can also be realized.

1.1.2 Measuring Temperature

The distribution of static temperature in a flame is arguably its most important characteristic, and it can be tuned by varying parameters such as flow rates and compositions of the incoming gases. The static temperature in the main region of the flame, where reactions are primarily bimolecular, is well understood. However, once outside this region, temperature models become more complex and variable, owing to the high temperatures and steep gradients involved. Many methods for measuring temperature exist and can be divided into these categories: probe thermometry, radiation thermometry, density thermometry, sonic thermometry, and laser scattering thermometry. These techniques are compared in Fristrom's "Flame Structure and Processes" [21] and will be summarized here.

Probe thermometry includes sensors such as thermometers, thermistors, thermocouples, and resistance temperature detectors (RTD). Each of these techniques is invasive, as the probe must be inserted into the flame during the measurement, and therefore they are incapable of measuring confined flames. The maximum use temperature for thermometers and thermistors is well below flame temperatures (≈ 700 K). Temperature is measured by an RTD across the length of the wire, not at a well-defined point, so they offer poor spatial resolution. Thermocouples for measuring flame temperatures up to 2500 K can be made, and have been the best available high-temperature quantification technique for some time. However, the error due to radiation losses is significant, and precise positioning of the thermocouple junction within the flame is necessary.

Thermometry can also be performed by measuring gas density and using the ideal gas law to determine temperature. This technique works well in high-temperature, low-density systems such as flames and is accurate as long as the molecular weights and concentrations of the constituents are well-known. Several gas density techniques that work on open flames include aerodynamic profiling, X-ray absorption studies, interferometry, and density gradient methods, but they generally require a confocal setup and cannot be employed on confined systems. Likewise, radiation thermometry (optical pyrometry, optical fiber probes, particulate thermometry, line intensity/shape methods) and laser scattering methods (Rayleigh scattering, resonant fluorescent scattering, Raman scattering, multiphoton scattering) are all limited to open systems. Forward looking infrared (FLIR) has been successful in the accurate temperature imaging of surfaces; however, FLIR cannot easily measure temperatures above 1100 K and is incapable of measuring gas temperatures. Temperatures can also be predicted through simulation, such as by computational fluid dynamics (CFD). While this powerful technique provides flexible, multidimensional, *in silico* analysis, it requires experimental confirmation of the predictions.

MRI offers several advantages over each of these techniques. It is noninvasive; no ionizing radiation is necessary for measurement and the system remains unperturbed. It is also multidimensional, without the need for confocal analysis, providing information on constituent density, temperature, and dynamics. MRI does present some limitations as compared with the other techniques described. It is a fairly expensive technique, with large superconducting magnets and, for the present study, sophisticated devices for inducing xenon hyperpolarization. At high magnetic fields, paramagnetic materials cannot be used, and imaging inside of metallic objects is not possible. However, more flexible analyses of combustion by magnetic resonance may be enabled by the use of remote detection [43] or low-field detection using either atomic magnetometers [68] or magnetometers based on the nitrogen vacancy center in diamond [62]. Micropolarizers are also currently being developed by John Kitching at NIST, in collaboration with our group, which operate at low field and produce HP xenon for use in microfluidic analyses.

1.1.3 Measuring Velocity

The visualization of gas transport within combusting systems is also of interest. The flow of gases is controlled by mass flow controllers, flow meters, the control of input pressures, and modifications to the combustion vessel. In order to analyze the effects of these controls on diffusion, mixing, and flow velocities, techniques such as particle velocimetry [48, 71], liquid-state MRI modeling [17], and laser doppler anemometry [16] are employed, none of which offers information about the combusting gases themselves.

Velocimetry can be performed using MRI by encoding velocity information in the moving gas nuclei [45]. By application of appropriate gradient pulses, the spins accrue phase proportional to the component of velocity along the gradient axis. This has been demonstrated in liquid systems [26, 49] and in the gas phase [28, 51]. By combining this information with the density and chemical shift information that MRI also provides, diffusion and mixing can be characterized.

1.2 Combustion NMR/MRI

1.2.1 Previous Studies

One- and two-dimensional NMR spectroscopy of active combustion *in situ* using HP xenon premixed with methane has been demonstrated previously in 2003 [1]. A 33 Hz upfield shift (-0.27 ppm) of the ^{129}Xe peak was observed during combustion. When the combustion was performed over a nanoporous material (Na-X zeolite pellets), regions of varying temperatures resulted, which could be differentiated using two-dimensional exchange spectroscopy (EXSY). In the presence of the zeolite, a -3 ppm shift in the top region of the zeolite was observed, and transfer from this region to the flame region at 29 Hz (-0.26 ppm) was demonstrated. An experiment with high-density xenon was also presented. The authors suggested that this technique could be applied to high-temperature catalyzed combustion in opaque media.

Later, an attempt was made to perform MRI on open methane flames using the Single-Point Ramped Imaging with T_1 Enhancement (SPRITE) [3] pulse sequence in 2005 [22]. This purely phase-encoded pulse sequence uses small tip angles so that the repetition time can be kept low. Proton images of the lit flame do not display any appreciable signal farther than 3 mm from the flame orifice, due to rapid depolarization. CFD simulations were presented to demonstrate that no methane should be present except at the bottom of the lit flame, and they also predicted the temperature and velocity distributions.

Although ^{129}Xe MRI of combustion was discussed and presented [41], no data was published. The ^{129}Xe EXSY study was covered in a 2003 Nature news article by Prof. Jeff Reimer [54], a 2005 review of xenon NMR [5], and a 2005 book chapter on xenon NMR imaging [50].

1.2.2 Area of Interest

The expertise within our research lab in the areas of HP xenon, velocimetry, microfluidics, and parahydrogen made this an attractive project. We chose to target confined combustion in general, and more specifically microscale combustion. Although parahydrogen has been utilized to image catalytic hydrogenation [10], the previous study demonstrating rapid depolarization of protons within the flame was discouraging. Parahydrogen is not an inert probe, and addition of the molecule to oxygen would need to be selective; therefore we did not pursue this approach.

HP xenon has been used in the lab to study gas flow through capillaries and polyurethane foams [15] and to perform velocity mapping around a sphere suspended in a pipe [28, 51]. The exchange rate of ^{129}Xe in cryptophane cages is temperature-dependent, and this has been exploited to determine temperature using the chemical shift [56, 57, 59]. High spectral, spatial, and temporal resolution in microfluidic devices have also been demonstrated using remote detection [29] and compressed sensing [49].

Chapter 2

Introduction to Magnetic Resonance

2.1 Nuclear Magnetic Resonance

A brief introduction to some of the nuclear magnetic resonance (NMR) principles pertinent to the NMR of combustion is presented in this section. Detailed descriptions of NMR can be found elsewhere [31, 37, 39].

2.1.1 The Chemical Shift

Atomic nuclei with non-zero spin have an intrinsic spin angular momentum with an associated magnetic moment. When placed in a magnetic field of magnitude B^0 in the z-direction, the component of the magnetic moment parallel to the field (μ_z) leads to a potential energy of

$$E = -\mu_z B^0. \tag{2.1}$$

The magnetic moment is proportional to the spin angular momentum, with the constant of proportionality known as the gyromagnetic ratio (γ). The spin angular momentum is quantized to $\hbar I_z$, where $I_z = \pm\frac{1}{2}$ for nuclei with ground-state nuclear spin $I = \frac{1}{2}$. The most commonly used nucleus in magnetic resonance imaging (MRI), the proton, as well as ^{129}Xe are each spin-$\frac{1}{2}$ nuclei, with the two energy states separated by:

$$\Delta E = \hbar|\gamma|B^0. \tag{2.2}$$

The ratio of the two populations is governed by the Boltzmann distribution, with polarization

$$\text{polarization} = \frac{\Delta E}{2\,k_{\mathrm{B}}T}, \tag{2.3}$$

and because ΔE is much less than $2\,k_{\mathrm{B}}T$, the population difference at thermal equilibrium is very slight. For ^{129}Xe at 9.395 T and room temperature (RT) the thermal polarization is about 9 ppm (see Appendix A.1.1).

The population difference leads to a bulk magnetization (M_0) of the sample in the direction of the magnetic field (longitudinal magnetization M_z). If the magnetization vector is tipped away from this direction, it will precess about the z-axis at an angular frequency proportional to the field strength, known as the Larmor frequency and defined by:

$$\omega^0 = -\gamma\, B^0. \tag{2.4}$$

The Larmor frequency in units of Hz is found by dividing each side of Equation 2.4 by $2\,\pi$:

$$\frac{\omega^0}{2\pi} = \frac{\gamma}{2\pi}\, B^0. \tag{2.5}$$

The values of $\frac{\gamma}{2\pi}$ for ^{1}H and ^{129}Xe are:

$$\gamma_{\mathrm{p}}/2\pi = 42.577\ \mathrm{MHz\,T^{-1}}, \tag{2.6}$$

$$\gamma_{^{129}\mathrm{Xe}}/2\pi = -11.860\ \mathrm{MHz\,T^{-1}}; \tag{2.7}$$

therefore at the same field strength ^{129}Xe precesses at $\approx 28\%$ of the frequency of ^{1}H and in the opposite direction, and thermal polarization is smaller by the same fraction. The positive precession frequency is a result of the ^{129}Xe magnetic moment being opposite in direction to the spin angular momentum [39].

The precise Larmor frequency of each nuclear spin is determined by the local value of the magnetic field that it experiences, which can differ from B^0. The electronic environment inside the atom or molecule helps determine this value, as electrons generate small magnetic fields that can increase or decrease the field that the nucleus experiences. The electrons are said to shield the nucleus from the external field, with the chemical shielding factor (σ) defined by:

$$\frac{\omega^0}{2\pi} = \frac{\gamma}{2\pi}\, B^0(1-\sigma), \tag{2.8}$$

which indicates that as σ increases, the Larmor frequency decreases. The shielding factor has fallen out of use, but is presented here due to its use in explaining the temperature dependence of the precession frequency (Section 2.3.2). The change in Larmor frequency from that of a reference sample (ω^0_{ref}) is more commonly referenced by the chemical shift, a dimensionless parameter defined by:

$$\delta = 10^6\, \frac{\omega^0 - \omega^0_{\mathrm{ref}}}{\omega^0_{\mathrm{ref}}}, \tag{2.9}$$

where the chemical shift, more intuitively, increases as the Larmor frequency increases. The chemical shift is related to the shielding factor by:

$$\delta = 10^6\, \frac{\sigma_{\mathrm{ref}} - \sigma}{1 - \sigma_{\mathrm{ref}}} \approx 10^6(\sigma_{\mathrm{ref}} - \sigma), \tag{2.10}$$

where the approximation assumes the shielding factor of the reference samples, $\sigma_{\text{ref}} << 1$ [31]. Chemical shifts are occasionally referred to as "upfield" (lower chemical shift) or "downfield" (higher chemical shift) due to the relative field necessary to achieve the same Larmor frequency as a result of differences in shielding. Table 2.1 summarizes these relationships.

Table 2.1: Relationships between chemical shift variables within a plotted spectrum. This table is equivalent for both positive and negative gyromagnetic ratios.

Variable	**Symbol**	**Left in Spectrum**	**Right in Spectrum**
local magnetic field	B^0	higher	lower
frequency	$\lvert\omega^0\rvert$	higher	lower
shielding	σ	less shielded	more shielded
chemical shift	δ	higher (downfield)	low (upfield)

Xenon-129 is unique in that its chemical shift range is extensive compared to other nuclei, ≈ 7500 ppm [23]. Xenon is highly polarizable due to its large electron cloud, which leads to this sensitivity to local environment and strong electron deshielding within xenon compounds. The chemical shift range for free ^{129}Xe is smaller, but still almost 200 ppm separate xenon dissolved in water from the pure gas reference. The chemical shift is also sensitive to density and temperature, which will be discussed in Section 2.3.2.

2.1.2 NMR Detection

In order to detect the precession of the bulk magnetization (M_0), it first must be rotated away from the equilibrium alignment with the main field. This is accomplished by applying a field along the x-axis that is resonant with the Larmor frequency and of sufficient bandwidth to excite spins with various chemical shifts. A radio frequency (RF) coil placed around the sample is used to apply this "pulse," which "excites" the spins, tipping the bulk magnetization away from the z-axis by an angle determined by the pulse duration.

Two flip angles are important for the studies presented here. The first is a $(\pi/2)_\phi$ pulse, which tips the magnetization 90 degrees, exactly into the transverse plane resulting in transverse magnetization, $M_{xy} = M_0$. The second is a $(\pi)_\phi$ pulse in which the magnetization is tipped 180 degrees, inverting it and resulting in $M_z = -M_0$ (also known as an inversion pulse). The phase of the pulses (Section 2.1.4) are indicated by ϕ.

Once tipped away from its equilibrium alignment with the field, the precession of the bulk magnetization can then be detected with the same coil used to excite the spins. The rotating magnetization induces an oscillating current in the coil, which is amplified and recorded. This quadrature signal is referred to as a free induction decay (FID).

2.1.3 Relaxation

After a $(\pi/2)_\phi$ excitation, the transverse component of the magnetization (M_{xy}), and therefore the signal, decays exponentially [46]:

$$M_{xy}(t) = M_0\, e^{-t/T_2}, \tag{2.11}$$

where T_2 is referred to as the spin-spin, or transverse, relaxation time constant. The decay is caused by return of the magnetization to its equilibrium alignment with the main field, as well as fluctuations in the field. The linewidths (full width at half-maximum) of the peaks in the Fourier transformed spectrum are inversely proportional to T_2:

$$\text{linewidth (Hz)} = \frac{1}{\pi\, T_2}. \tag{2.12}$$

For the flowing hyperpolarized (HP) xenon mixture used in this study, the T_2 is approximately 16 ms and the linewidth is about 14 Hz. This broadening is due to the experimental conditions including low spin density and rapid flow.

After a $(\pi/2)_\phi$ excitation, the longitudinal magnetization (M_z) returns to its equilibrium value according to:

$$M_z(t) = M_0\,(1 - e^{-t/T_1}) \tag{2.13}$$

where T_1 is referred to as the spin-lattice, or longitudinal, relaxation time constant, because the relaxation involves the transfer of energy to the surrounding lattice. For HP xenon, T_1 can be on the order of seconds to minutes, which means that the repetition time (TR) must be long enough for the system to return to equilibrium between pulses. However, for the work presented here, the spins travel through the coil in a time $<< T_1$ and are rapidly replace; therefore the TR is set to only 500 ms.

2.1.4 Spin Echoes and Phase Cycling

The measured linewidth is broadened by inhomogeneity of the magnetic field that masks the intrinsic transverse relaxation. The effective decay parameter is denoted T_2^*. The T_2^* is always less than or equal to T_2, and the inhomogeneously broadened linewidth is equal to $1/\pi T_2^*$. The inhomogeneity can be refocused by the use of a Hahn echo [25] (also known as a spin echo), in which the a $(\pi)_{\phi_2}$ pulse is applied following the $(\pi/2)_{\phi_1}$ pulse after a period of time. The $(\pi)_{\phi_2}$ pulse is referred to as a refocusing pulse because it causes any inhomogeneous broadening to be refocused at twice the time, between the pulses, known as the echo time (TE).

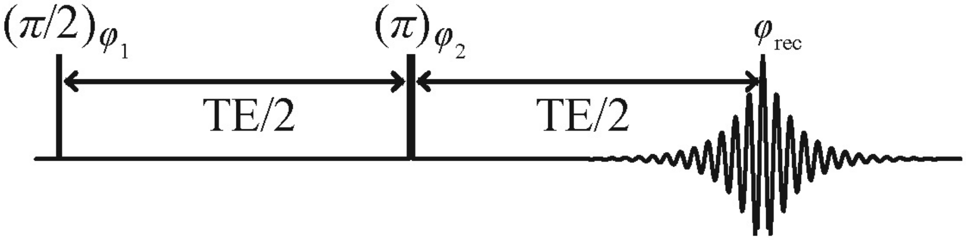

Figure 2.1: Spin echo pulse sequence with phase cycling.

The phase of the pulses and receiver (ϕ_1, ϕ_2, ϕ_{rec}) can be varied in order to suppress signals caused by hardware imperfections. This is known as phase cycling. A phase cycle for the spin echo pulse sequence is shown in Table 2.2.

Table 2.2: Four-step phase cycling for spin echo experiment [39].

Cycle number	ϕ_1	ϕ_2	ϕ_{rec}
0	0	0	0
1	0	$\pi/2$	π
2	0	π	0
3	0	$3\pi/2$	π

2.2 Magnetic Resonance Imaging

Detailed descriptions of MRI, including the spatial frequency k-space, can be found elsewhere [8, 46]. In this section, some of the specific pulse sequences and techniques used in the MRI of combustion are described.

2.2.1 Gradient Echo Multi Slice

The Varian **gems** pulse sequence (Figure 2.2) is typical of many pulse sequences used to image stationary samples without the acquisition of spectral information. The pulse sequence uses a slice-select gradient (G_z) to excite only a slice of the sample along the z-axis, by bringing only those spins into resonance with the RF pulse. The phase-encoding gradient (G_y) encodes position in the phase of the signal by moving to a particular point in k-space for each acquisition. The G_x gradient is known as the readout gradient, and it is a frequency-encoding gradient. The frequency of the precessing spins is varied during readout. This particular type of pulse results in a gradient echo, where the spurious phase shifts resulting from gradient fields is refocused at the center of the readout section of the pulse.

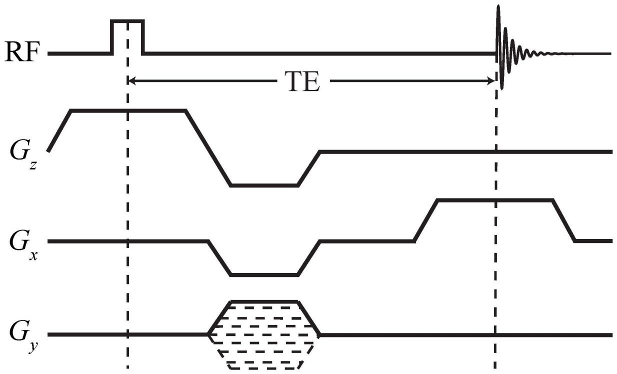

Figure 2.2: Gradient echo pulse sequence **gems**. The G_z gradient is slice-select, G_y is phase-encode, and G_x is frequency-encode and readout with gradient echo [58].

Two of these encoding strategies are not possible in directly-detected, flowing systems, such as the combustion study presented here. The slice-select is not possible because of the rapid movement of the spins, particularly in the z-direction. Frequency-encoding is not possible in spectroscopic imaging (Section 2.2.2), as the frequency dimension is reserved for encoding the chemical shift. Therefore, the pulse sequences were designed with phase-encoding only, in each dimension.

With phase-encoding, the extent of image-space in any one dimension, known as the field of view (FOV) is:

$$\mathrm{FOV} = \frac{N_{\mathrm{pe}} - 1}{2\,\frac{\gamma}{2\pi}\,A}, \qquad (2.14)$$

where N_{pe} is the number of phase-encodes and A is the total area of the gradient pulse. The spatial resolution (δ_i) is calculated from the FOV_i:

$$\delta_i = \frac{\mathrm{FOV}_i}{N_{\mathrm{pe}}}. \tag{2.15}$$

2.2.2 Chemical Shift Imaging

In chemical shift imaging (CSI), also known as spectroscopic imaging, a spectrum is acquired at each spatial position [11, 14, 40]. These spectra are then used to generate images that indicate the variation of chemical shifts across the image space. In medical imaging this technique is used for fat/water imaging [30, 60].

The k-space corresponding to the spatial positions is usually sampled in a Cartesian format in CSI. This permits four-dimensional fast Fourier transform (FFT) of the complex signal,

$$s(t) = \int_x \int_y \int_z \int_f m(x, y, z, f)\, e^{-i\,2\,\pi\,(k_x(t)\,x + k_y(t)\,y + k_z(t)\,z + k_f(t)\,f)}\, dx\, dy\, dz\, df, \tag{2.16}$$

to image and frequency space. The time dimension is treated as a fourth k-space dimension (k_f). The pulse sequence (Figure 2.3) includes a refocusing pulse that generates a spin echo which allows for sampling of the negative k_f-space. The k-space trajectory along three of the four dimensions is detailed in Figure 2.4. The refocusing pulse inverts all three k-space coordinates at $k_f = \mathrm{TE}/2$ [46].

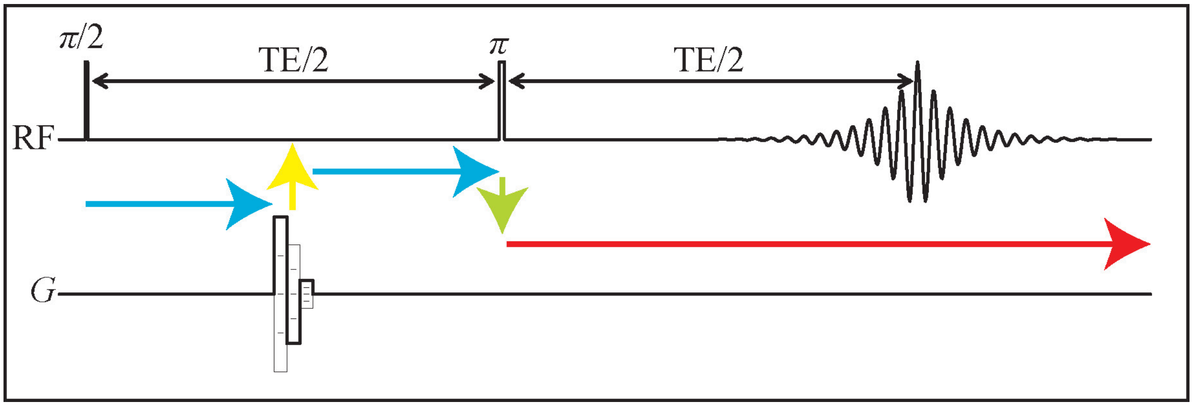

Figure 2.3: Spin echo CSI pulse sequence with a gradient moment nulling postion-encode. Gradient pulses are applied in all three spatial dimensions.

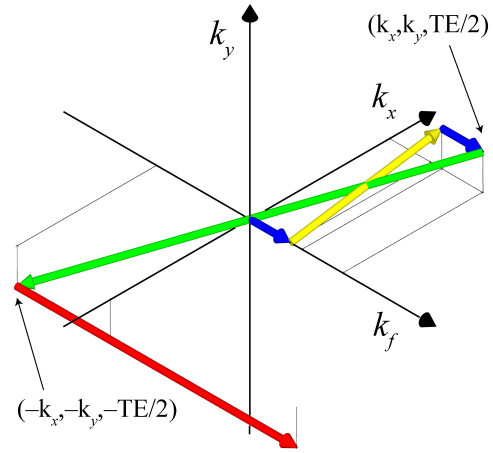

Figure 2.4: k-Space trajectory during the pulses, phase-encoding, and detection for encoding in x- and y-space. The k_f-dimension is the time dimension. The spin echo causes time-inversion and allows sampling of $k_f = 0$.

2.2.3 Gradient Moment Nulling

Motion can cause artifacts in MRI due to the introduction of a phase shift that varies in k-space. This phenomenon is observed with the flow of blood in medical imaging and in the MRI of moving systems in general, and it can manifest itself in images as ghosting, signal loss, and flow displacement artifacts [47]. Gradient moment nulling (GMN) [7] involves modifying the gradient waveforms within the pulse sequence in order to make it more immune to these types of artifacts.

Gradient moments can be calculated from the waveform shape and the equations of motion. The phase accrued during a gradient waveform is

$$\phi(t) = \gamma\, m_0(t)\, x_0 + \gamma\, m_1(t)\, v_0 + \frac{\gamma}{2}\, m_2(t)\, a_0 + \ldots\,, \tag{2.17}$$

where the n^{th} gradient moments are equal to

$$m_n(t) = \int_0^t G(u)\, u^n \, du. \tag{2.18}$$

For m_0, this is simply the signed sum of the areas of the gradient lobes ($G\Delta t$ for rectangular waveforms), whereas the m_1 and m_2 moments have quadratic and cubic dependence on time, respectively. By applying gradient waveforms in which two of the three moments have been nulled, position, velocity, or acceleration can be encoded in the phase without artifacts caused by the other two moments. This requires a minimum of three pulses; the calculated ratios of pulses of various shapes are presented in Appendix B.2 and a rectangular, position-encoding gradient waveform is presented in Figure 2.5.

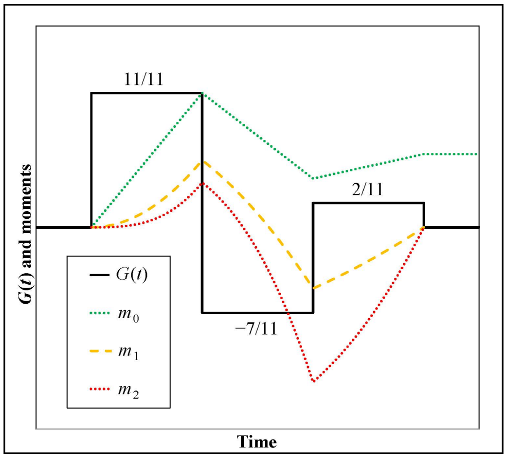

Figure 2.5: Gradient moment nulling for position-encoding with both velocity (m_1) and acceleration (m_2) compensation. The ratios of $\frac{11}{11} : -\frac{7}{11} : \frac{2}{11}$ are necessary for a gradient waveform with three equal-length, rectangular lobes.

2.2.4 Velocimetry

Velocimetry using MRI allows the determination of the individual components at each point of the image by phase-encoding [44, 45]. GMN was used to design three-lobed pulses that encode velocity while compensating for position and acceleration (ratio of $\frac{2}{2} : -\frac{3}{2} : \frac{1}{2}$). Unlike position-encoding, where multiple phase-encodes are used, in velocity-encoding only two encodes are necessary using the same gradient amplitudes, but opposite directions. This leads to a difference in m_1 between the two datasets, which when combined with the phase difference between the signals can be used to determine the velocity [8]:

$$v = \frac{\Delta\phi}{\gamma\left|\Delta m_1\right|}. \tag{2.19}$$

Δm_1 must be carefully chosen so that the phase difference us with the range $-\pi < \Delta\phi < \pi$, and does not wrap. The aliasing velocity parameter (VENC) determines the maximum velocity before the phase will wrap:

$$\text{VENC} = \frac{\pi}{\gamma\left|\Delta m_1\right|}. \tag{2.20}$$

2.3 Hyperpolarized Xenon

Detailed descriptions of the use of HP xenon produced by spin exchange optical pumping [65] in NMR and MRI can be found elsewhere [23, 24, 50].

2.3.1 Xenon Relaxation

Prolonged spin exchange optical pumping within the pumping cell with line-narrowed lasers can can result in ^{129}Xe polarizations approaching 60% [66, 67]. However, in order to perform continuous flow studies of combustion, the HP xenon mixture must travel to the region of the flame continuously. The homebuilt polarizer (Appendix A.1) utilized in the studies presented here is capable of producing polarizations typically in the range of $1-10\%$, which is more than sufficient for single shot acquisition at atmospheric pressure.

Maintaining the xenon hyperpolarization as the HP mixture travels from the cell to the flame is important. The output of the polarizer is placed within the stray field of the magnet to avoid any zero crossings, and the tubing material is carefully chosen to avoid surfaces that promote depolarization such as brass and copper. The HP xenon must also pass through a needle valve prior to the flame, so it is important that the drop to from the cell pressure to atmospheric pressure is not accompanied by a drop in polarization due to the needle valve components.

2.3.2 Temperature Dependence

The ^{129}Xe NMR chemical shift is dependent upon various factors including the temperature (T in K), density of xenon (ρ in amg), interactions with other gases, and interactions with surfaces. The temperature dependence of the second (σ_1 in ppm amg^{-1}) and third (σ_2 in ppm amg^{-2}) virial coefficients of the chemical shift (σ in ppm) [34], where

$$\sigma(\rho, T) = \sigma_0 + \sigma_1(T)\,\rho + \sigma_2(T)\,\rho^2 + \sigma_3(T)\,\rho^3, \tag{2.21}$$

have only been measured in the range $T = 240 - 440$ K for $\rho = 20 - 95$ amg (1 amg $= 2.687 \times 10^{25}$ m^{-3}). In that range, σ_1 was found to increase with increasing temperature:

$$\sigma_1(\tau) = -0.536 + 0.135 \times 10^{-2}\,\tau - 0.132 \times 10^{-4}\,\tau^2 + 0.598 \times 10^{-7}\,\tau^3 - 0.663 \times 10^{-10}\,\tau^4, \tag{2.22}$$

where $\tau = T - 300$ K; σ_2 was also found to increase with increasing temperature. This leads to an increase in σ and a decrease in chemical shift (δ) with increasing T. Within this range an increase in the ρ leads to an increase in δ [32]. The change of the gas composition due to the chemical reaction also effects δ, and the effect of oxygen [33] and methane [35] density have also been studied.

Chapter 3

Combustion Experimental Methods

3.1 Instrumental Approach

3.1.1 Model System

In order to obtain hyperpolarized (HP) xenon magnetic resonance images (MRI) of combustion processes *in situ*, the high-temperature reactions must take place within the bore of a superconducting magnet. Therefore, it is important to keep the temperature of the reaction as low as possible and to thermally insulate it from the instrumentation. This prevents damage to the imaging probe and gradients, and avoids a quench of the cryogen-cooled magnet, a dangerous and costly occurrence. The exhaust gases from the combustion should also be properly vented and not particularly dangerous.

The simplest model system is an open flame, in which xenon is premixed with the component gases. A four-inch long ceramic tube, where the flame burns at one end, was chosen (hereafter referred to as the "combustion tube"). The ceramic tubes are available in various inner (ID) and outer diameters (OD) and with one, two, or four bores, which allows optimization of flame size and type. The flame size can also be adjusted by varying the input pressures and flow rates of the constituent gases (Section 3.3.2).

There are two main types of flames: premixed flames and diffusion flames. In a premixed flame, the oxidizer is mixed with the fuel prior to the flame front. Premixed flames are not an ideal model system as the presence of oxygen prior to the flame front would lead to a significant signal loss, because oxygen causes relaxation of polarized xenon (see Section 2.3.1). Additionally, premixed flames are potentially hazardous, as there is a danger of the flame flashing back to the point of mixture. Therefore, a diffusion flame, where the oxidizer meets the fuel at the flame front is necessary, with the xenon premixed with the fuel. As the name suggests, the fuel must diffuse with the oxidizer in a diffusion flame, and they are therefore slower burning. Diffusion flames also tend to produce more soot than premixed flames, due to incomplete combustion. To achieve a symmetric diffusion flame, a four-bore tube was chosen as the combustion tube.

Initial tests of air-fueled methane diffusion flames, which had been analyzed in each of the previous combustion nuclear magnetic resonance (NMR) studies [1, 22], resulted in high enough temperatures to melt the Teflon (melting point 327 °C) pieces fabricated to hold the ceramic combustion tubes. Air-fueled flames also flickered substantially (Figure 3.1a), making them non-ideal for MRI, with static flames being preferred due to the non-instantaneous (time-averaged) nature of the acquisition. Methane diffusion flames fueled by pure oxygen (Airgas part no. OX K) were found to be hotter, but more stable in a well-defined jet-like flame (Figure 3.1b).

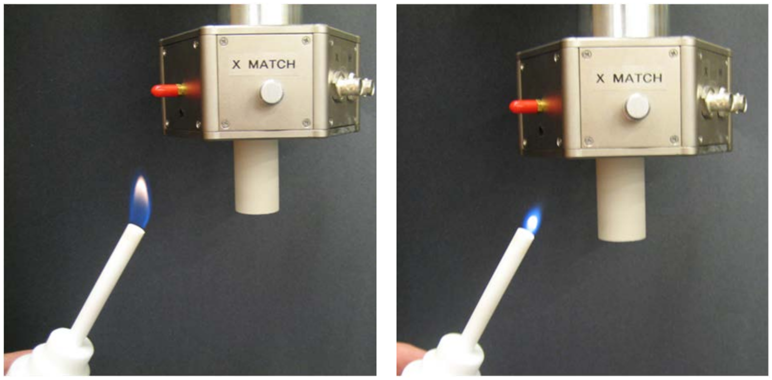

(a) (b)

Figure 3.1: Initial testing of methane flames fueled with air (a) and pure oxygen (b). The oxygen-fueled flame is more jet-like and does not flicker. Flames are shown here with the commercial 40-mm probe and chimney tube.

A survey of other combustible gases was made to determine the optimal model system. Dimethyl ether (DME, also known as methyl ether) was tested to see if cooler flames would be possible with this potential alternative fuel [2]. DME is of particular interest because particle image velocimetry studies [71] have been performed with DME, which is low-sooting [36] due to its lack of carbon-carbon bonds. By adjusting the oxygen enrichment ratio (Section 3.3.2), a relatively low-temperature flame of appropriate size was produced with DME, and many of the initial tests were performed with this system. Unlike diethyl ether, DME does not form explosive peroxide radicals, and therefore long-term storage of DME cylinders does not pose a hazard.

Without a good quantitative measurement technique, the relative flame temperatures of methane and DME were unknown. After further research, it was determined that methane flames (adiabatic flame temperature of $\approx$ 2230 K) are not necessarily hotter than DME flames ($\approx$ 2290 K), at least based on previous modeling studies (see Yoon [70], Fig. 4). The adiabatic flame temperature is the temperature of a complete combustion process that does not result in heat transfer or changes in kinetic or potential energy. However, the flames produced and studied in the present study were not adiabatic. The oxygen enrichment ratios used for each gas were different, while instead the volumetric ratios were kept constant (Section 3.3.2). Diffusion flames are also unlikely to be adiabatic in general. In the end, the experiments were performed using both methane (Airgas part no. ME CP200) and DME

(Sigma Aldrich part no. 295299-1KG), for comparison. High-temperature thermocouples were used later to determine that the maximum flame temperatures in the imaging study were ≈ 1500 K (Section 3.3.7).

3.1.2 Insulation and Cooling

Along with keeping the flame temperature as low as possible, it is also necessary to insulate the flame from the probe, gradients, and magnet bore. The vertical-bore, 400-MHz magnet (Oxford AS400/89) used for the studies has a bore diameter of 89 mm. The temperature in the bore was measured to be below room temperature (RT) at ≈ 16 °C, a result of the dewar of liquid helium that the coils are housed in and which is only separated from the bore by a thin vacuum layer. The gradient (Varian part no. SGRAD 88/55/HS/S) bore ID is only 55 mm, and the gradient stack is water-cooled to 18 °C using a recirculating water chiller located outside of the 5-gauss line. The narrow ID of the gradient bore causes some difficulty in keeping heat properly dissipated (Figure 3.2).

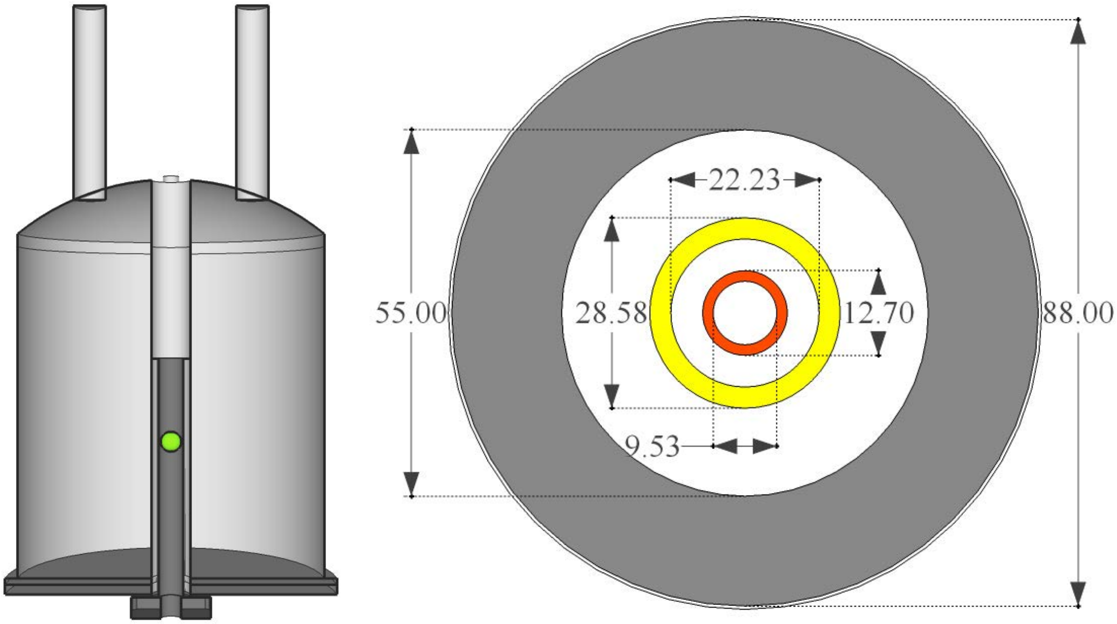

(a) (b)

Figure 3.2: (a) The liquid helium-cooled, liquid nitrogen-jacketed superconducting magnet, with 89-mm bore. Also shown is the imaging gradient stack (inserted from below), with OD/ID of 88/55 mm, and gradient "sweet spot" (47-mm sphere, green). (b) Cross-section of the dimensions (in mm) of the gradient stack (dark-grey) and the chimney (yellow) and containment (orange) ceramic tubes. The flame is bounded by the containment tube.

The previous studies (Section 1.2.1) of combustion inside of superconducting magnets employed two different strategies for cooling. In the ^{1}H MRI study [22], water cooling was not possible because protons were being detected, and the water would interfere with the imaging. Instead a loop gap resonator, which itself was water-cooled, was placed in contact with the glass "chimney" in their setup. The ^{129}Xe spectroscopy study [1] used only air cooling of the probe from an air compressor.

In the present study a combination of ceramic tubing and water tubing was used for insulation and cooling. Four-foot long ceramic tubes, made of mullite (60.0% alumina, 37.9% silica) and later 99.8% alumina (Section 3.3.3), were secured from McDanel Advanced Ceramic Technologies (part nos. MV0161130-43-48 and 98A311030-43-48) and Ortech. This long tube acts as a chimney (herein referred to as "chimney tube"), containing the hot exhaust gases as well as creating an insulating barrier for the flame region (Figure 3.3a).

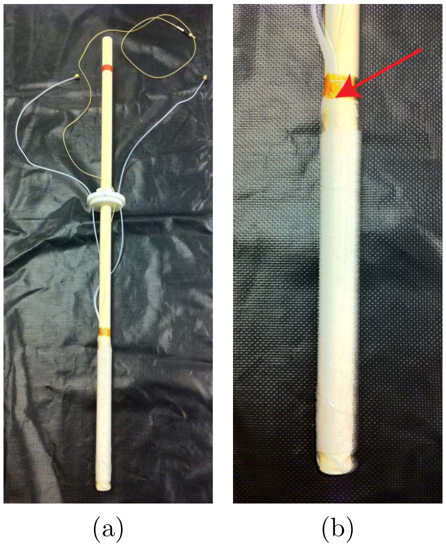
(a) (b)

Figure 3.3: (a) The 4-foot long chimney tube, made of 99.8% alumina, carries off hot exhaust and insulates the flame from the magnet. A custom Teflon piece centers it in the top of the magnet bore. (b) Cooling water flows through 1 foot of tightly-wound, coiled Teflon tubing taped to the lower portion of the chimney tube. The end of the yellow fiber optic thermometer probe is placed just above the tubing (red arrow) with Kapton tape. The temperature in this warmest region of the chimney tube does not exceed 35 °C during the studies.

Active cooling was provided by wrapping the outside of the chimney tube with 1/8″ Teflon tubing through which water was flowed (deionized water from the lab tap at ≈ 120 mL/min). Additionally, house dry nitrogen gas was used to cool the inside of the chimney tube (Section 3.1.3). Using this scheme, the temperature at the surface of the ceramic tube during the combustion experiments was kept to approximately $25 - 35$ °C, only slightly higher than the normal magnet bore temperature. Another cooling strategy that was considered involved installing a Garolite G-10 tube (McMaster-Carr part no. 8527K241) around the chimney tube and sealing off each end with heat-resistant epoxy (Stycast or Permabond 620) to allow cooling water to flow through the outer jacket, in direct contact with the ceramic. This was not implemented due to the limited amount of space this design left for tube fittings.

The temperature was measured using a fiber optic thermometer (Neoptix Reflex), the sensing tip of which is positioned on the outside of the combustion tubing, just above the water tubing, where the highest temperature was found to occur (Figure 3.3b). This device was employed in the encapsulated HP xenon MRI thermometry study [56, 57], and is useful here because it is nonmagnetic and non-metallic and can therefore be used inside the magnet bore during the experiment. The fiber optic thermometer is based on the temperature-dependent absorption of light of the gallium arsenide semiconductor in the sensing tip [38]. Constant temperature monitoring is necessary, both to ensure that the apparatus does not get excessively hot, and to determine if the flame has gone out. The temperature was also recorded before and after each acquisition to rule out temperature drift as a source of error.

3.1.3 Exhaust Handling and Safety Considerations

After consultation with campus Environment Health and Safety, it was determined that the exhaust gases could be collected and removed to the return-air duct of the Stanley Hall heating, ventilation, and air conditioning (HVAC) system. The small amount of carbon monoxide and unburned fuel present in the exhaust was determined not to be a hazard. The gases were collected by attaching a Tygon tube to the top of the chimney tube (Figure 3.4a), which was fed into a larger section of air duct hose. The air duct hose was attached to a blower (Grainger part no. 4C440) that provided suction of the exhaust to the return-air duct (Figure 3.4b). The full 60 standard cubic feet per minute (SCFM) of flow was not attached directly to the chimney tube, but rather it provided negative pressure that allowed the exhaust to clear the tube. The total flow through the chimney tube is approximately 0.2 SCFM (Table 3.3).

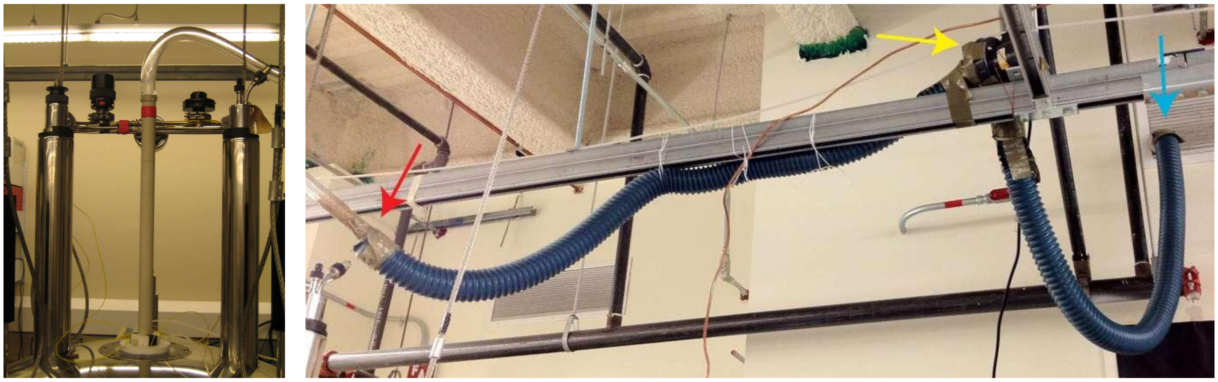
(a) (b)

Figure 3.4: (a) Tight-fitting Tygon tube easily connects to the chimney tube after ignition. (b) Exhaust from Tygon tube is drawn to the HVAC return-air duct (blue arrow) by a blower (yellow arrow). Connection between the air duct hose and the Tygon tube is not sealed (red arrow), so that room air is also drawn into the hose.

Xenon gas is heavier than air, so it was necessary to ensure that it did not accumulate in the bore. House nitrogen was flowed through the outside of the containment tube at

12 standard cubic feet per hour (SCFH) to aid in the clearance of xenon from the bore, and aid in cooling as discussed previously. No nitrogen flow was present inside of the containment tube, as it was found that this was not possible without causing the flame to extinguish or behave erratically. All combustible gas cylinders were stored at least 20 feet away from one another, and the oxygen cylinder, as per safety guidelines. They were electrically grounded by attaching a wire to the valve with a pipe clamp, which was run to the house ground of a power outlet.

A remote detection [43] setup would require compression of the exhaust gases prior to detection with a microsaddle coil. This would need to take place outside of the magnet due to the size and material constraints dictated by the magnet dimensions. The engineering challenge that this presented was significant enough that these measurements could not be included in the scope of this study, but it seems like a reasonable next step in the MRI of combustion.

3.1.4 Initial Approach

The original strategy for combustion imaging was to use a commercial 40-mm double-resonance (^{1}H/^{129}Xe) probe (part no. SW40PFMN07), manufactured by Varian for the 400-MHz magnet. This probe is a hollow-bore vertical imaging probe. A Teflon holder was built to position a four-inch long, four-bore combustion tube inside of the probe. The flame burns at the end of the tube where the HP xenon and combustible gas mixture meets with pure oxygen (Figure 3.5a). The gas connections to the combustion tube were made by inserting one inch of $\frac{1}{16}''$ Teflon tubing into each of the four bores of the combustion tube after applying a liberal amount of Super Glue (82 °C maximum operating temperature), which consists of ethyl-2-cyanoacrylate with poly(methyl methacrylate). This forms a tight seal that does not fail as a result of the heating of the combustion tube during combustion.

There were three tiers to the Teflon holder (Figure 3.5b). The largest diameter (1.62″) of this holder fit snugly inside of the 40-mm probe, to center it within the coil. The next tier up was the same diameter as the OD of chimney tube (1.15″), so that it could be taped onto the end of it. The last tier (0.87″) fit tightly inside of the chimney tube so that the combustion tube could be centered inside of it. The flame was lit outside of the chimney and the holder was carefully placed inside of the chimney and taped in place. The whole apparatus was then carefully raised into the probe.

Prior to attempting ^{129}Xe detection, the magnet was shimmed by using a T_1-relaxed water sample in a 5-mm NMR tube, mounted on top of the combustion tube in a custom fabricated Delrin holder (12.5 Hz linewidth). When xenon was flowed through the combustion tube, no signal was detected using the calibrated pulse length (210 µs at 55 dB transmitter power). This acquisition was performed with significant signal averaging. Unfortunately, the filling factor for this probe was less than ideal for such a small jet (approximately 10 mm diameter, 20 mm high) at atmospheric pressure, where spin density is low.

As a check, the combustion tube was removed and replaced with a $\frac{1}{4}''$ Teflon tube with a needle valve at the end so that pressurized HP xenon could be present in the coil. Using this

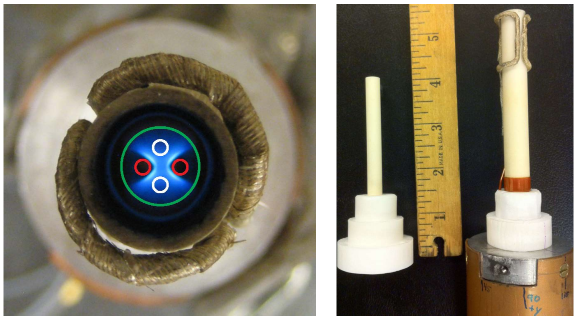

(a) (b)

Figure 3.5: (a) A picture of the flame at the outlet of the combustion tube (McDanel Ceramics part no. AXF1183-04-06), the outline of which has been added in green (7.92 mm OD). A mixture of HP xenon and fuel (DME here) is delivered from the bores (1.57 mm ID) highlighted in red, where they meet with pure oxygen, delivered from bores highlighted in white. Note that the colored portion of the flame corresponds to the location of the oxygen. (b) Left: Original design of combustion tube holder for use with commercial 40-mm probe. Right: Final design with homebuilt coil wrapped around the containment tube.

setup at 70 psig with 0.3 standard liters per minute (SLPM) of flow, signal was detected, as expected, with an signal-to-noise ratio (SNR) of 10. Therefore, it was decided that a new, homebuilt probe would need to be fabricated including a saddle coil with an optimal filling factor. The first probe designed was a single-resonance ^{129}Xe probe, but more sophisticated probes such as double-resonance probes with ^{1}H and/or ^{13}C and remote detection were considered.

3.1.5 Coil Design

A saddle-shaped coil [64] was designed that would match the diameter and height of the flame. A template was fabricated out of Teflon for bending and shaping a coil with a diameter of 15 mm and a height of 25.4 mm (Figure 3.6a). The shaft collars shown in the figure were used along with the template to help bend the 90-degree turns in the coil without scraping off the coating.

The 16-AWG (0.0508″) copper wire used for the coil (Rea Super Hyslik 200) is coated with a tris-(2-hydroxyethyl) isocyanurate (THEIC) modified polyester and then a modified polyamide imide overcoat. This coating fails at temperatures above 280 °C according to the manufacturer. When placed in close proximity to a flame the THEIC blackened, an indication of failure, even when shielded from the flame by a ceramic containment tube (Figure 3.6b). This was unacceptable due to the fact that the coil crosses itself as part of the saddle geometry, and a failure of the coating would lead to a short circuit.

The coil and approximately two inches of the leads were wrapped with high-temperature mica tape (McMaster-Carr part no. 6811A23) to prevent the coating from failing, and as added insulation. The mica tape, which consists of mica paper bonded to glass cloth and

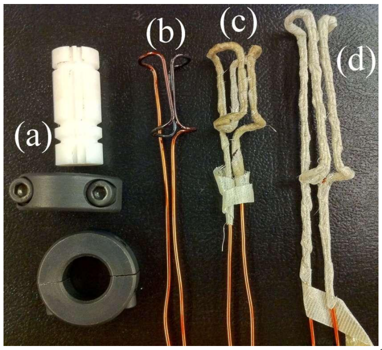

Figure 3.6: (a) Teflon saddle coil template for 15-mm coils (3/4″ or 1″ in height) with black shaft collars for aid in bending. (b) A coil with blackened coating in the regions not covered by mica tape. (c) Used 1″ coil with mica tape wrapping. (d) New 2″ coil designed for use in expanded field of view studies.

infused with a silicone elastomer, is effective up to ≈ 1200 °C and does not interfere with the ^{129}Xe signal. Even after direct exposure to the flame, the mica tape prevents damage to the coil (Figure 3.6c). To avoid the mica tape from unraveling, a small amount of shrink tubing was used to hold it in place at the base of the leads.

A "containment tube" was added to the final design, with an ID of 0.375″ (9.53 mm) and OD of 0.5" (12.70 mm). This containment tube has several purposes. First, it adds another layer of protection for the coil from the flame and provides some support for the coil so that it does not become accidentally deformed during usage. It also provides an outer boundary for the flame, so that it stays only within the coil. With the containment tube in place, the coil is separated from the flame by an opaque barrier. Therefore, the imaging study is of an enclosed flame.

3.1.6 Probe Housing

The probe body is fabricated from a piece of 2.125″ OD copper tube (McMaster-Carr part no. 5175K214), 16.875″ in length, with 0.058″ wall thickness. Three 2″ diameter aluminium discs are used as structural elements within the probe body: two at each end and one placed just below the circuit board to aid in alignment of the tuning rods (Figure 3.7). All pieces were fabricated in the College of Chemistry student machine shop and are nonmagnetic.

The aluminium discs are each 1/2″ thick. The bottom aluminium disc has holes for the tuning rods as well as for the gas lines. A nonmagnetic, through-wall BNC coupler is also housed on this disc, and is grounded to the probe body. A tuning rod holder was added later (Section 3.1.7). The main purpose of the middle disc is to align the tuning rods with the capacitors. However, it provides structural integrity to the probe as well. Two additional holes in the disc allow passage of the gas lines and the coaxial cable. The top disc has a single large hole in it for attaching the Teflon combustion tube holder as well as a slot for mounting the circuit board (Section 3.1.8). The aluminium discs are attached and grounded to the probe body using three #4-40 brass screws each.

Figure 3.7: Side view of the inside of the probe body (bottom-to-top from left-to-right). The bottom disc supports the BNC coupler, the medium disc guides the tuning rods, and the top disc holds both the circuit board and the combustion tube holder. Gas lines and coaxial cables are not shown for clarity. Also not shown: tuning rod holder (Figure 3.9) and shield (Section 3.1.8).

3.1.7 Electronics

Minimizing the length of the coil wire will result in improved sensitivity; for that reason, the resonant circuit as well as the tuning and matching capacitors must be placed in close proximity to the flame. The circuit board is made of copper mounted on Garolite G-10, a glass-cloth laminate with expoxy resin, and cannot withstand the high temperatures of the flame (maximum use temperature 130 °C). Therefore, it is mounted on the bottom of a $\frac{1}{2}''$ aluminium disc which is also used to mount the Teflon combustion tube holder to the probe and grounds the circuit to the probe body.

The single-resonance circuit (Figure 3.8a) is designed to allow tuning and matching to the ^{129}Xe Larmor frequency of 110.6 MHz at 9.4 T. Variable $1-30$ pF nonmagnetic capacitors (Johanson part no. 5641) that can be adjusted with a slotted screwdriver, are used for tuning (C_T) and matching (C_M). They are mounted on the circuit board as shown in Figures 3.8b and 3.8c.

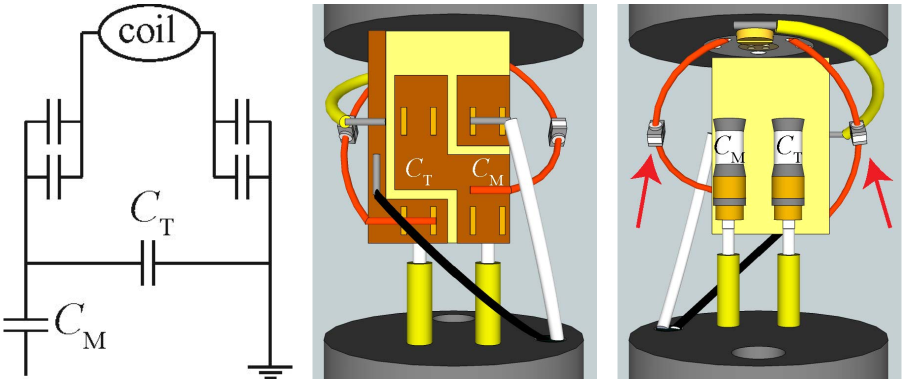

(a) (b) (c)

Figure 3.8: (a) Circuit diagram with $1-30$ pF tuning (C_T) and matching (C_M) capacitors. Also shown are parallel chip capacitors added to bring circuit into resonance (10.0 pF each). (b) Top of circuit board for single-resonance probe. White cable is coaxial transmission core, black is coaxial shield (ground), yellow is probe ground. (c) Bottom of circuit board detailing mounting locations of $1-30$ pF tunable capacitors for tuning and matching and parallel chip capacitors (red arrows) in series with coil (copper). Gas tubing omitted for clarity.

Most homebuilt probes within the Pines Lab are remote detection [43] probes which are inserted into the top of the magnet bore, with the tuning rods held in place by gravity. However, this type of design is not possible with the combustion probe, which must be mounted from below. Application of upward force caused the thin G-10 rods to bend, making them difficult to keep in place and aligned. Additionally, the approach of filing the ends of the rods into slotted screwdriver tips was not robust enough to survive several rounds of tuning and matching.

Thicker G-11 rods that are more rigid and temperature-resistant (maximum use temperature 170 °C) were used instead. In place of filing the tips, 0.102″ ceramic slotted screwdriver tips (McMaster-Carr part no. 5879A24) were installed. The screwdriver tips are mounted by using the lathe to drill out an appropriate-sized hole in the G-11, then inserting the tips after placing a few drops of Super Glue in the holes. Even with the more rigid design, getting the tuning and matching capacitors aligned with the alignment holes built into the probe body was difficult. The screwdriver tips were at first glued onto the capacitors themselves, to prevent the rods from falling out due to gravity. This design necessitated taking the entire probe apart every time the glue failed.

To prevent this, a custom tuning rod holder was designed (Figure 3.9). An aluminium housing was fabricated, which contained non-magnetic springs (Small Parts, Inc. part no. CS-48-01) and o-rings chosen to provide upward force and friction to the tuning rods. This kept them in place and made gluing the tips to the capacitors unnecessary. This has been a very successful strategy and should be implemented in future homebuilt probes.

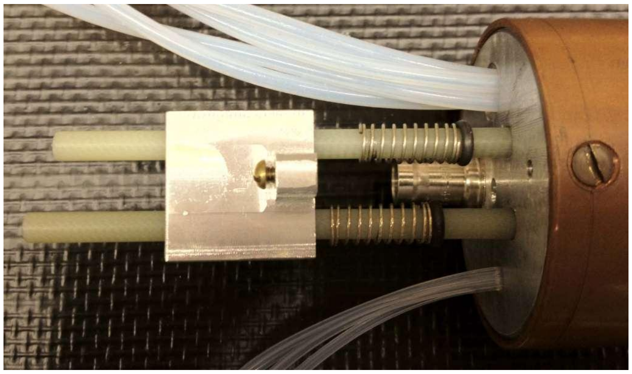

Figure 3.9: Custom-designed tuning rod holder, used to provide upward force on the rods to keep them seated in the capacitor adjustment slots. All pieces are nonmagnetic (aluminium housing, silver-coated beryllium copper springs, brass screw). Holder is shown disassembled for purposes of displaying what is inside.

To increase the resonance frequency, capacitors were added in series to the coil wires (Figure 3.8c). The resonance frequency (ω_{osc}) is proportional to the inverse square root of the capacitance (from Levitt [39] Eq. 4.2):

$$\omega_{\text{osc}} = (L\,C_{\text{T}})^{-1/2}, \tag{3.1}$$

where L is the inductance and C_{T} is the total capacitance in the tuned circuit. Two 10.0 pF chip capacitors (American Technical Ceramics part no. ATC100B100J) were added on each end of the coil in parallel, prior to its connection to the chip. This was done instead of adding them to the already crowded chip. After the addition of these capacitors to lower C_{T}, $\omega_{\mathrm{osc}}/2\pi$ could be adjusted to 110.6 Hz within the tunable range of the variable capacitors.

The target frequency is 110.575 MHz, which is the default calibrated ^{129}Xe frequency on the VnmrJ software. However, the actual resonance frequency of ^{129}Xe in the RT HP mixture was found to be 110.574 MHz and this is what was used as the spectrometer transmitter frequency ($\omega_{\mathrm{ref}}/2\pi$) and chemical shift reference frequency ($\omega^0_{\mathrm{Xe(ref)}}/2\pi$; equivalent to $\omega^0_{\mathrm{TMS}}/2\pi$) and the probe was tuned and matched at this frequency. Even though the probe was retuned and matched at equilibrium flame temperature, the shimming was only performed with the flame unlit (Section 3.3.4), and $\omega_{\mathrm{ref}}/2\pi$ was kept at the RT value.

3.1.8 Further Grounding

A properly tuned circuit must be well-grounded in order to achieve good sensitivity. This can be verified by testing the root-mean-square noise level (σ_{noise}), where σ_{noise} is defined by:

$$\sigma_{\mathrm{noise}} = \langle s^2_{\mathrm{noise}} \rangle^{1/2}. \tag{3.2}$$

A first test of the noise of the coil was made on the probe as originally configured. The σ_{noise} measured was 74.6 (Figure 3.10a), which is quite high compared to commercial probes and well-grounded and shielded homebuilt probes, which usually have σ_{noise} values of ≈ 5 under the same testing conditions. Therefore, attempts were made to further ground the circuit and probe, and to shield the coil from magnet and gradient eddy currents.

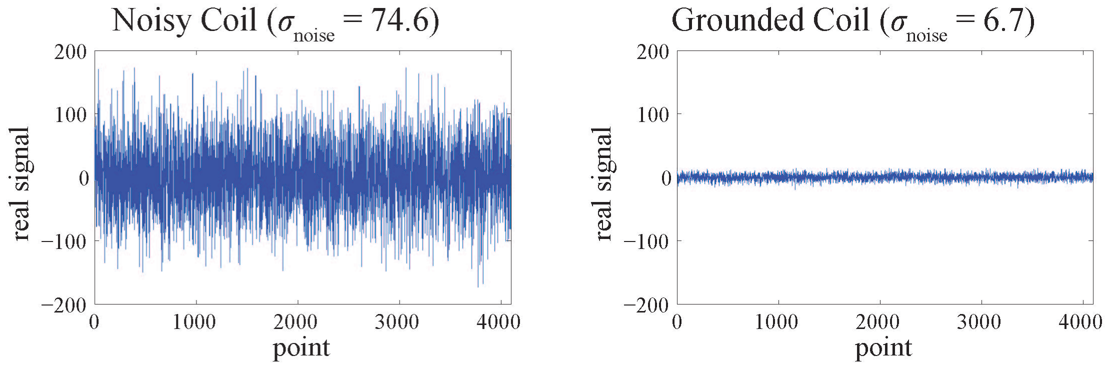

(a) (b)

Figure 3.10: (a) Noise collected for probe as originally configured. The rms noise (σ_{noise}) is well above what is possible with a well-grounded probe. (b) Probe noise after additional grounding and shielding, an order of magnitude improvement in σ_{noise}.

The circuit board had already been grounded to the aluminium disc supporting it by mounting the chip in a deep groove in the disc. The chip was designed so that the strip of copper connected to the tuning capacitor would be inside this groove. Aluminium flux paste (LA-CO part no. 22404) was used to help solder the copper to the aluminium disc prior to rigidly gluing it in place with epoxy. A grounding wire (yellow in Figures 3.8b and 3.8c) was now added that connected the chip to the aluminium disc for additional grounding that did not rely on the potentially loose solder connection in the groove.

A copper shield was added around the coil region to protect it from gradient and magnet eddy currents. A 6″ length of the same 2.125″ OD copper tubing was screwed into the top aluminium disc, by creating notches in the probe body at those locations. Size #4-40 brass screws were used for attachment and grounding to the probe. Repeating the noise test after the modifications resulted in a σ_{noise} of 6.7, more than ten times lower (Figure 3.10b). This means the probe is ten times more sensitive (SNR improvement of > 10) than it was as originally constructed.

3.1.9 Remote Lighter

Preliminary studies with the flame ignited in the magnet were undertaken by lighting the flame outside of the magnet, then inserting the probe assembly into the bore from below. Not only was this a difficult process, especially when done repeatedly, but it made it so that any shimming (Section 3.3.4) done without the flame lit was no longer optimal due to the movement of the probe. Shimming was performed with HP xenon only flowing. This produced the narrowest peak due to the homogeneous environment. Then the flame should be ignited without any other change in the system, other than the addition of the other gases.

A remote lighting apparatus was desired that could ignite the flame while the probe assembly was inside of the magnet. With the help of undergraduate researcher Doug Shin, a remote sparking tool was made (Figure 3.11a). The charging circuit that powers the flash in a disposable camera was used to build up a charge in its capacitor, which is allowed to jump a small gap across two gold-plated tips of a coaxial cable lowered down the four-foot long chimney tube. The center core of the coaxial cable and the shielding mesh were used to complete the circuit from either terminal of the capacitor and a switch capable of handling the high voltage was used to ignite the flame. Several seconds were required to obtain an appropriate charge to create a spark.

In order to optimally position the sparking apparatus in the tube, a copper coil was fashioned to sit on top of the containment tube and allow the leads to hover directly above the gas jet. Early attempts at lighting the flame were quite explosive. It was determined that if the oxygen was turned on first, the excess oxygen led to more violent explosions upon ignition; in some cases the ignition sounded like a gun shot. Thus, in later attempts, the DME combustible gas was first turned on (at 0.1 SCFH for one second), then the oxygen was turned on (0.3 SCFH for one additional second), at which point the switch for ignition was depressed. The rod holding the igniter was then removed from the tube, and a flame check was made visually, using a watch glass to protect one's eyes from the exhaust gases. With repeated use the gold-plated tips acquired a black coating that did not allow the current to

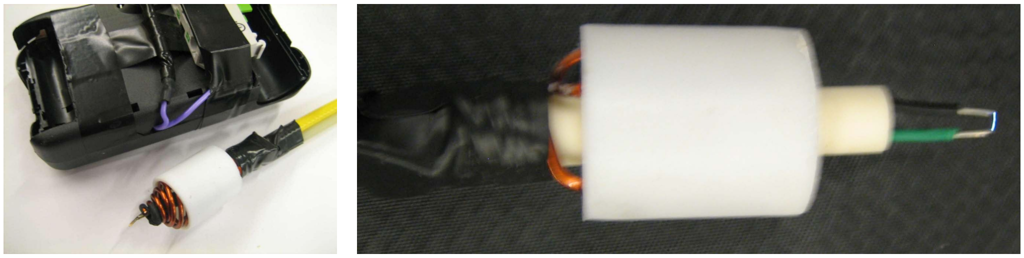
(a) (b)

Figure 3.11: (a) Sparking mechanism using charge stored in a disposable camera flash charging capacitor. A one-time current flows across the spark gap between two gold-plated pins, igniting the flame. (b) Continuous spark produced from the sparking mechanism from a butane lighter.

jump the spark gap, and required scraping with a razor blade to remove.

This process was tedious, unpredictable, and as suggested above, somewhat dangerous. This problem can be solved by continuously sparking the igniter at high enough frequency that it lights as soon as the optimal ignition mixture is achieved. A continuous-flame butane igniter was procured (McMaster-Carr part no. 77115A21) which included a continuous ignition system. A similar approach to that which was used with the camera mechanism was implemented. A wire was attached to each end of the igniter's capacitor. These wires were run down a G-11 rod, through a second alumina combustion tube (as shown in Figure 3.11b). Using the continuous-sparking igniter, the flame could be lit very reproducibly, with full flow on (including the nitrogen flow). This allowed acquisition of the "lit" images directly after the "unlit" images, with equivalent shim values.

3.2 Pulse Sequence

3.2.1 Temporal Challenges

The short residence time of the xenon spins in the coil presents challenges for sensitive and multidimensional detection. The radio frequency (RF) and gradient pulses as well as the acquisition time (**at**) must all take place while the nuclear spins pass through the coil. The time spent in the coil is approximately 100 ms; this value is based on calculations using the flow rate of HP xenon and the dimensions of the combustion and containment tubes (Table 3.1). Assuming that the HP xenon does not decelerate after exiting the bores of the combustion tube, the shortest amount of time spent in the coil is less than 20 ms. If it fills the entire containment tube volume prior to passing through the coil, it could be in the coil $\approx$ 360 ms. All of these calculations assume that the gases are at atmospheric pressure.

Table 3.1: Residence time in coil.

Property	**Value**	**Units**
coil height	25.4	mm
bore ID (4-bore combustion tube)	1.57	mm
cross-sectional area of each bore	1.94	mm^2
cross-sectional area of two bores	3.87	mm^2
containment tube ID	9.53	mm
cross-sectional area of containment tube	71.33	mm
volume of containment tube in coil	1812	mm^3
HP xenon flow rate (total)	5000	$\mathrm{mm}^3\ \mathrm{s}^{-1}$
linear flow in bores	1291	$\mathrm{mm\ s}^{-1}$
residence time (minimum)	19.7	ms
linear flow in containment tube	70	$\mathrm{mm\ s}^{-1}$
residence time (maximum)	362.4	ms

This amount of time is insufficient to perform any pulse sequence requiring long sets of gradient pulses or extensive acquisition times, and because of the rapid flow in the z-direction, precludes slice-select gradients. The short residence time also makes T_1-weighting nearly impossible, as not enough evolution time exists to discriminate between small changes in T_1 relaxation. Fortunately, the pulse widths needed to manipulate the spins, $(\pi/2)_\phi$ and $(\pi)_\phi$ pulses, are only on the order of tens of microseconds. This means that a technique like single-point ramped imaging with T_1 Enhancement (SPRITE) [3], in which pulses of less than $(\pi/2)_\phi$ are used, is not necessary. The maximum gradient amplitude of 100 G cm^{-1} is also sufficient to apply phase-encoding gradient pulses in hundreds of microseconds. The final parameters used were an echo time (TE) of 8 ms, followed by 200 ms of acquisition time. One benefit of the short residence time is that it decreases the necessary sequence repetition time (TR), eventually chosen to be 500 ms, enabling shorter total experiment times.

3.2.2 Early GEMS Images

The single pulse sequence, **spuls**, was used to determine the optimal $(\pi/2)_\phi$ pulse width on the 15-mm combustion coil ($\approx$ 25 µs at 55 dB transmitter power). Some low-SNR images of HP xenon flow were then acquired on the homebuilt probe using the **gems** (gradient echo multi slice) pulse sequence built into VnmrJ (Section 2.2.1). The slice-selecting gradient was set to zero so that the $(\pi/2)_\phi$ pulse excited the entire z-projection of the phase-encoded plane (in x and y).

The one- (1D) and two-dimensional (2D) images were acquired with only HP xenon flowing at 0.3 SLPM through the coil, and were the first acquired at atmospheric pressure (ie. without the pressurized tube described in Section 3.1.4). These are spin density-weighted images, as a different type of pulse sequence is needed to ascertain chemical shift and velocity information. The 1D image in x (Figure 3.12a) is a projection in both y and z.

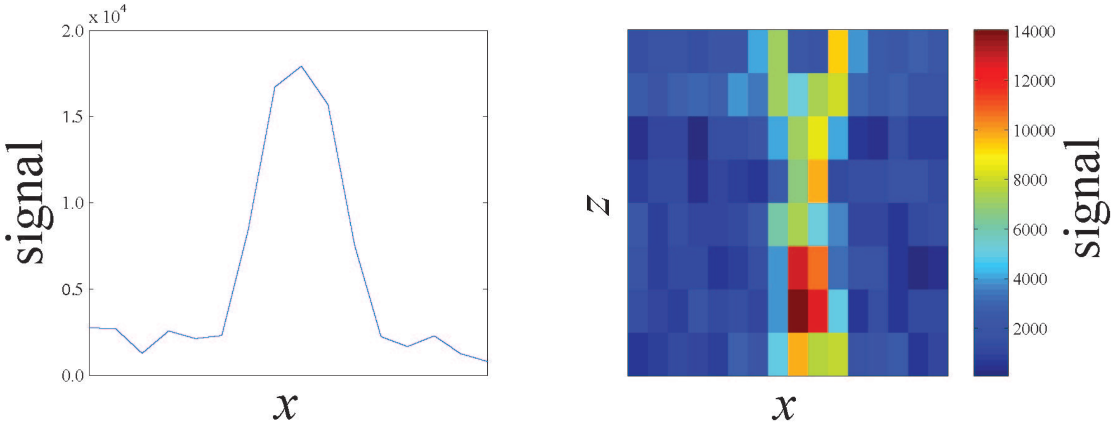

(a) (b)

Figure 3.12: 1D and 2D ^{129}Xe density images acquired using the Varian **gems** pulse sequence with the homebuilt probe. (a) 1D projection image along x ($N_{\mathrm{ro}} = 16$, $\mathfrak{N} = 1024$). (b) 2D coronal (xz plane) projection image ($N_{\mathrm{ro}} = 16$, $N_{\mathrm{pe}} = 8$, $\mathfrak{N} = 512$). The distance units are not shown, as they had not yet been determined.

3.2.3 Chemical Shift Imaging

The first spectroscopic data was acquired using Hahn spin echo experiments (see Section 2.1.4). A $(\pi/2)_\phi$ pulse followed by a $(\pi)_\phi$ pulse, followed by acquisition of the spin echo. A spin echo pulse sequence was needed not only to refocus dephased spins, but also to sample the negative and zero of frequency k-space (Figure 2.4), resulting in frequency data across the full bandwidth. The center frequency selected to be the spectrometer reference for ^{129}Xe, 110.575 MHz.

In the previous ^{1}H MRI SPRITE imaging study [22], a high degree of signal averaging was used, due to the low proton spin density. For the unlit image, 2500 averages were acquired (total experiment time of 3 hours), while in the lit image 6000 averages were acquired (7.5 hours). In the present work, phase cycling was used, so averaging was always in multiples of four in order to have full phase cycles (Section 2.1.4).

For chemical shift imaging (CSI), encoding gradient pulses must be added between the RF pulses. Spatial frequency-encoding is not possible, as the frequency information is what is being imaged. Therefore, all gradient-encoding performed is through phase-encoding, where the phase of the spins encodes their location. The first studies were performed with single-lobed, square gradient pulses spaced in the center of the two RF pulses.

3.2.4 Gradient Moment Nulling

The fast moving gases lead to artifacts in the images, manifesting themselves as apparent vortexes within the containment tube and a broadening of the xenon jets (Figure 3.13a). Therefore, nulling of the velocity and acceleration components of the accrued phase was undertaken using the technique of gradient moment nulling (GMN; Section 2.2.3). First, velocity phase information was nulled using a two-lobed GMN pulse sequence with a ratio of $\frac{3}{3} : -\frac{1}{3}$, resulting in the image shown in Figure 3.13b. The second-order magnetic moment (m_2) still contributes to the swirling observed in this image.

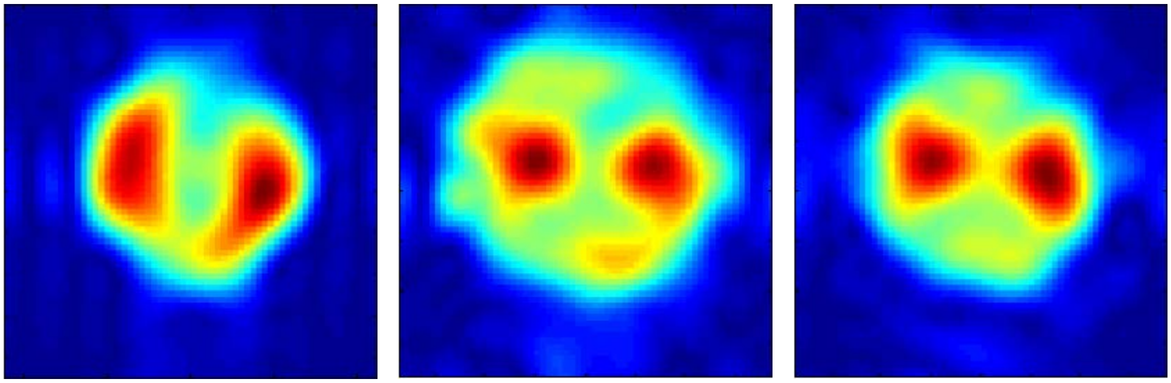
(a) (b) (c)

Figure 3.13: Axial (xy-plane) xenon density images with HP xenon and oxygen flowing from the bores along the x- and y-axes respectivley: (a) with single-lobed phase-encoding, no GMN; (b) with two-lobed velocity compensated phase-encoding; (c) with three-lobed velocity and acceleration compensated phase-encoding. Increasing normalized density from blue to red.

To nullify this moment, caused by acceleration, a three-lobed GMN pulse sequence was created with rectangular pulses in the ratio of $\frac{11}{11} : -\frac{7}{11} : \frac{2}{11}$. These pulses were positioned exactly between the $(\pi/2)_\phi$ and $(\pi)_\phi$ RF pulses and were placed adjacent to each other (i.e. no delay). The resulting density image is closer to what is expected, a more symmetrical image with xenon density focused in the oulets along the x-axis.

In order to minimize the total time of the pulses, it is advantageous to approach the maximum gradient amplitude value of ±100 G cm^{-1}. There is a finite ramp time for the gradients (100 µs), and therefore rectangular gradients are in actuality trapezoidal in shape. With a deviation from rectangular, the calculated ratios of the gradient lobe strengths are no longer valid for effective GMN. The ratios were recalculated for triangular lobes (for low- to mid-resolution studies: 1.6 or 0.8 mm) and trapezoidal lobes (for high-resolution studies: 0.4 mm). See Appendix B.2 for detailed calculations. For reference, the resolution in the SPRITE study was 1.25 mm. A velocity and accelerated pulse sequence with triangular lobes is shown in Figure 3.14.

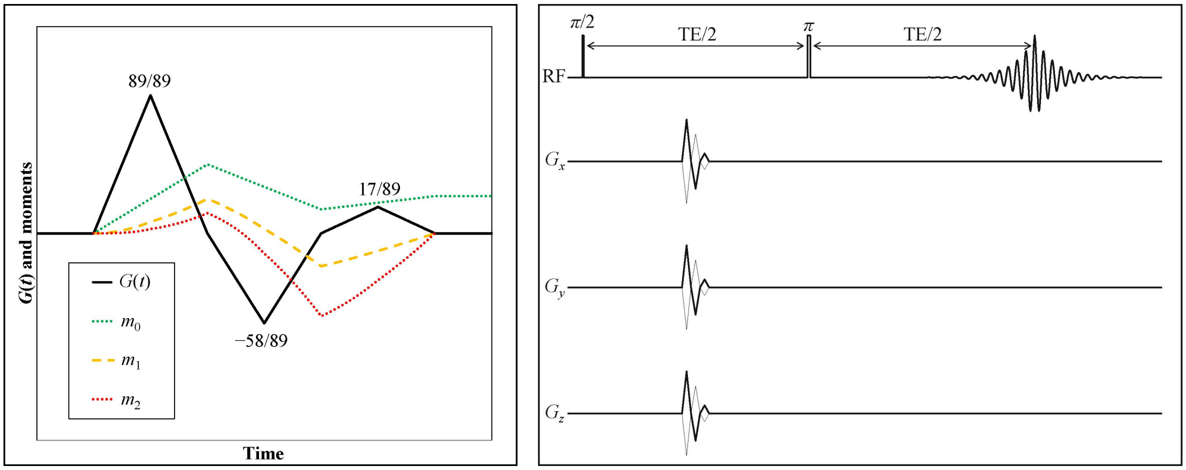

(a) (b)

Figure 3.14: (a) A three-lobed triangular gradient with ratios of $\frac{89}{89} : -\frac{58}{89} : \frac{17}{89}$ effectively nulls the first- and second-order moments (m_1 and m_2), so that the only phase that accrues is due to position. (b) The full CSI pulse sequence, with the gradient pulse positioned between the two RF pulses so that the delays on either side are equal; TE = 8 ms.

3.2.5 Velocity Imaging

The CSI mapping of temperature was qualitative in nature, so it was desirable to perform a more quantitative analysis of the flame. In order to phase-encode velocity information, another set of gradient lobes must be added to the pulse sequence. Normally a simple bipolar gradient (ratio of $1 : -1$) would be sufficient to encode velocity, however, as mentioned in the previous section, acceleration nulling was effective in cleaning up the images. A three-lobed gradient that nulls phase accrued due to position and acceleration has a ratio of $\frac{2}{2} : -\frac{3}{2} : \frac{1}{2}$ (Figure 3.15a). This ratio is valid for equal length rectangular, triangular, or trapezoidal gradient lobes.

The velocity gradient lobes are placed before the position-encoding lobes, with equal spacing between the two RF pulses. The z velocity is expected to be within the range of $7 - 129$ cm s^{-1} (Table 3.1). The gradient values were adjusted so that the phase would not wrap unless the velocity in any dimension exceeded ±500 cm s^{-1}. The full pulse sequence code is presented in Appendix C.1.

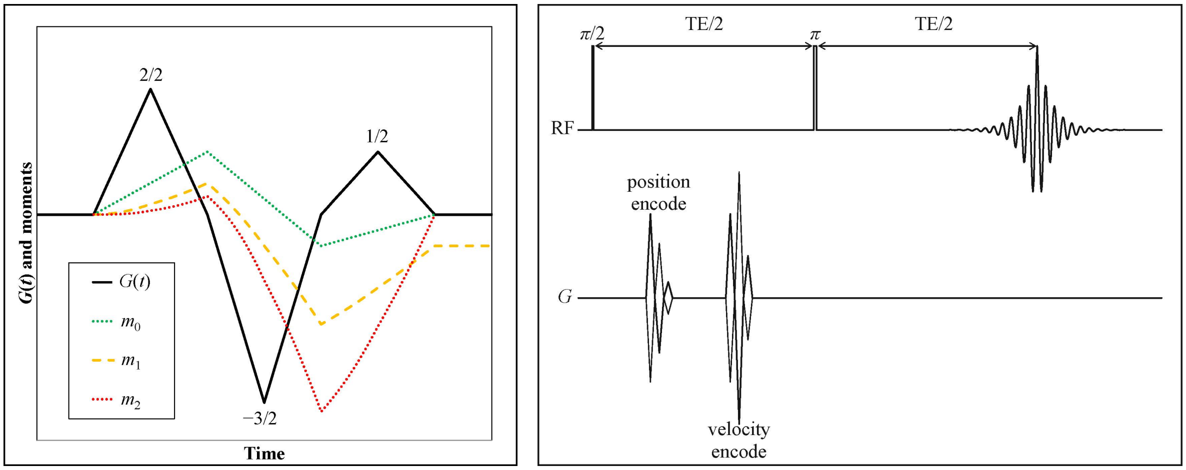

(a) (b)

Figure 3.15: (a) A three-lobed triangular gradient with ratios of $\frac{2}{2} : -\frac{3}{2} : \frac{1}{2}$ effectively nulls the zeroth- and second-order moments (m_0 and m_2), so that the only phase that accrues is due to velocity. (b) The full velocity pulse sequence, with the gradient pulses positioned between the two RF pulses so that the three delays are equal; TE = 8 ms.

3.3 Experimental Parameters

3.3.1 Combustion Reactions

The combustible gases chosen were the simplest alkane, methane, along with the simplest ether, DME.

Table 3.2: Properties of methane and DME.

Gas	**Methane**	**DME**
molecular formula	CH_4	C_2H_6O
density (kg m^{-3})	0.717	1.97
melting point (°C)	-182.5	-141
boiling point (°C)	-161.6	-24.8

The molar ratios of fuel to oxygen for the two stoichiometric reactions are 1 : 2 and 1 : 3.5 respectively. Note that there is an oxygen in DME, which leads to this difference in molar ratios. In order to use air as the oxygen source (≈ 21% oxygen), the flow of air would need to be 9.5 to 16.7 times greater than the fuel flow for a stoichiometric reaction.

$$\mathrm{CH_4 + 2O_2 \rightarrow CO_2 + 2H_2O} \tag{3.3}$$

$$\mathrm{C_2H_6O + \frac{7}{2}O_2 \rightarrow 2CO_2 + 3H_2O} \tag{3.4}$$

Therefore, the oxidizer used was pure oxygen, which resulted in more static, jet-like flames (Section 3.1.1).

3.3.2 Flow Rates

The flow rates of the various gases (HP xenon, combustible gas, oxygen, nitrogen) need to be adjusted to achieve a flame with acceptable xenon signal which was also stable, of appropriate size, and safe. The most important flow rate to optimize is that of the HP xenon (2% natural abundance xenon, 10% nitrogen, balance helium). The mass flow controller (MFC) on the homebuilt xenon polarizer can be set to a range of flow rates between 0.1 and 0.8 SLPM. The homebuilt probe was used to determine the linewidth and SNR at several flow rates (Figure 3.16) and the optimal flow rate of 0.3 SLPM was chosen, because it had the minimum linewidth with sufficient SNR.

All of the previous experiments with gaseous HP xenon were detected under pressure, with a needle valve present at the end of the line. However, in the present study detection must be performed at atmospheric pressure, and thus the needle valve must be placed prior to the detection region. The purpose of the needle valve is to keep the cell at a constant pressure, allowing HP xenon to flow at the rate delivered by the MFC. The needle valves generally used are metal and have interior surfaces made of brass (Figures 3.17a and 3.17b).

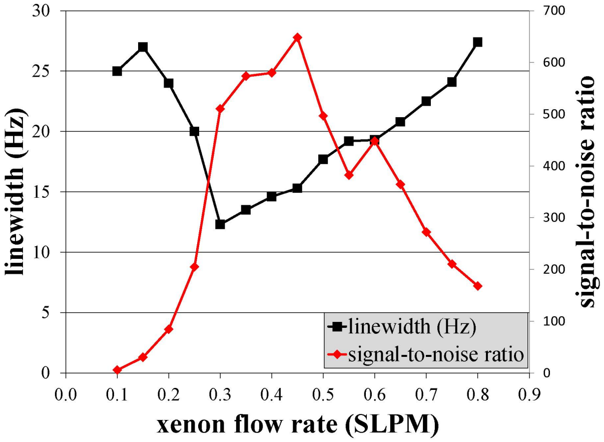

Figure 3.16: The HP xenon flow rate was optimized by measuring the linewidth and SNR at several flow rates. The flow rate chosen, 0.3 SLPM, had the narrowest linewidth and reasonable SNR. Narrow linewidth is more important for CSI studies.

HP xenon can relax on surfaces such as these. It was found that the amount of depolarization at the needle valve varied with positioning. As the valve was reoriented, signal could be maximized or made to disappear completely. To overcome this issue, the metal needle valve was replaced with a perfluoroalkoxy (PFA) needle valve (Partek part no. MV-13-100), which did not display this issue (Figure 3.17c).

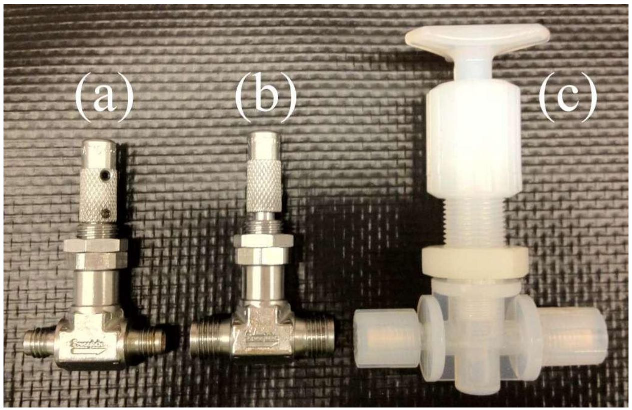

Figure 3.17: (a) Brass-interior needle valve with connections for 1/8″ Swagelok. (b) 1/4″ model. (c) PFA needle valve used to prevent orientation-dependent depolarization.

While the HP xenon was delivered using the mass flow controller, the other gases were delivered using flowmeters calibrated for air (Key Instruments Model MR3000, part nos. MR3A00SVVT and MR3A04SVVT) and mounted on a piece of plywood for easy adjustment. The methane, DME, and oxygen high-pressure cylinders were connected to the flowmeters via Swagelok quick-connect double-end shutoff stems. The individual regulators were all set to 40 psig, as the maximum flowmeter pressure is 100 psig.

Optimization outside of the magnet was performed with a range of flow rates. A glass

Table 3.3: Gas flow rates used in the combustion experiments.

Gas	**Flow Rate (SCFH)**	**Flow Rate (SLPM)**	**Percentage (%)**
HP xenon mix	0.64	0.30	61.4
combustible gas	0.10	0.05	9.7
oxygen	0.30	0.14	29.0
nitrogen	12	5.7	N/A

Table 3.4: Gas percentages in the mixes used in each experiment.

Gas	**Anala et al. [1] (%)**	**Mustonen et al. (%)**
xenon	3	1.7
nitrogen	5	8.6
helium	53	76.0
methane	39	13.6

tube of approximately the same ID as the chimney tube was used for monitoring flame under similar conditions to those of the experiment. The final flow rates (Table 3.3) were 0.3 SLPM HP xenon mixture, 0.1 SCFH combustible gas (methane or DME), 0.3 SCFH oxygen (delivered by two separate flow meters at 0.15 SCFH each), and around 12 SCFH of nitrogen through the outer holes (for cooling at clearance of xenon). These flow rates result in 1 : 3 molar ratios of combustible gas to oxygen. This means that the methane reaction is slightly oxygen-enriched (equivalence ratio $\approx$ 0.67) and the DME reaction is slightly oxygen-deficient (equivalence ratio $\approx$ 1.17).

The ratio of HP xenon to combustible gas used in the present study is approximately 6.4 : 1 (which is about 86.4%/13.6%; see Table 3.4). In the spectroscopy study [1], the percentages were quoted to be 3% xenon, 53% helium, 40% methane (from a 5% xenon, 8% nitrogen, balance helium HP mixture). In other words, HP xenon was mixed with the methane in a 60/40 ratio (by volume). The enrichment ratio is unknown, but air (not pure oxygen) was used as the oxidant.

As the rubidium cell ages, the pressure tends to climb more quickly, a likely effect of rubidium escaping from the cell. When this occurs, the needle valve must be adjusted to lower the pressure in the cell. Experiments are started when the pressure in the cell is at 50 psig and once the cell reaches 70 psig, they must be complete. Adjustment of the needle valve usually extinguishes the flame, which must be relit. Thus, adjustment of the needle valve cannot be performed during the acquisition.

3.3.3 Temperature-Dependent Magnetic Susceptibility

In the ^{129}Xe exchange spectroscopy (EXSY) study [1] it was suggested an observed −3-ppm shift in the zeolite region may be caused by magnetic susceptibility effects, and not temperature. The flow in that region is reduced and therefore susceptibility effects would be more pronounced. The authors did not revisit this, but suggested flow field experiments.

In the present study, a significant temperature dependence on the chemical shift was noticed when using ceramic tubes made out of mullite, a less expensive ceramic material made of both alumina and silica, and containing significant levels of impurities (Table 3.5). One of the impurities, iron oxide, is paramagnetic and thus likely to contribute to the temperature-dependent magnetic susceptibility.

Table 3.5: Components in the mullite and alumina tubes (from McDanel Advanced Ceramics datasheets). By switching to 99.8% alumina tubing, the amount of paramagnetic iron oxide is decreased by a factor of 20.

Compound	**Formula**	**Mullite (%)**	**99.8% Alumina (%)**
alumina	Al_2O_3	60.0	99.820
silica	SiO_2	37.9	0.060
calcia	CaO	0.1	0.040
magnesia	MgO	0.2	0.035
iron oxide	Fe_2O_3	**0.5**	**0.025**
sodium oxide	Na_2O	0.2	0.008
titania	TiO_2	0.5	0.004
chromic oxide	Cr_2O_3	–	0.003
potassium oxide	K_2O	0.6	0.001
boron oxide	B_2O_3	–	0.001

The temperature-dependent magnetic susceptibility was demonstrated by monitoring the chemical shift of ^{129}Xe as the tubes cooled. A simple pulse-acquire sequence with a TR of one second (1 Hz) was started with the flame on, and after five seconds the flame was extinguished by stopping the flow of methane and oxygen. The spectra were monitored over the course of five minutes and are displayed in Figure 3.18a. As shown, the chemical shift drifts more than 0.5 ppm (55 Hz) as the tube cools. After replacement of the mullite tubing with 99.8% alumina tubing, the drift during cooling is reduced significantly as shown in Figure 3.18b.

3.3.4 Tuning and Shimming

Tuning and matching of the NMR circuit must be performed at both RT and at the equilibrated flame temperature due to the temperature dependence of the resonant frequency. At RT, the probe is tuned to the frequency of HP xenon alone, but with water and nitrogen cooling flowing as well. At elevated temperature, the resonance is once again adjusted to this same frequency. In the ^{129}Xe EXSY study [1], 30 minutes was allowed to pass for the system to equilibrate. Here, both the optical thermometer and the resonance line itself were used to monitor the equilibration. Once the resonance line and temperature stopped fluctuating, the probe was tuned.

Shimming of the xenon gas flow is difficult due to the chaotic mixing and the relatively large size of the sample (1.81 mL). While a water sample could be shimmed to several Hz linewidth, the best shimming of the HP xenon jet is $\approx$ 12 Hz. Addition of the oxygen and

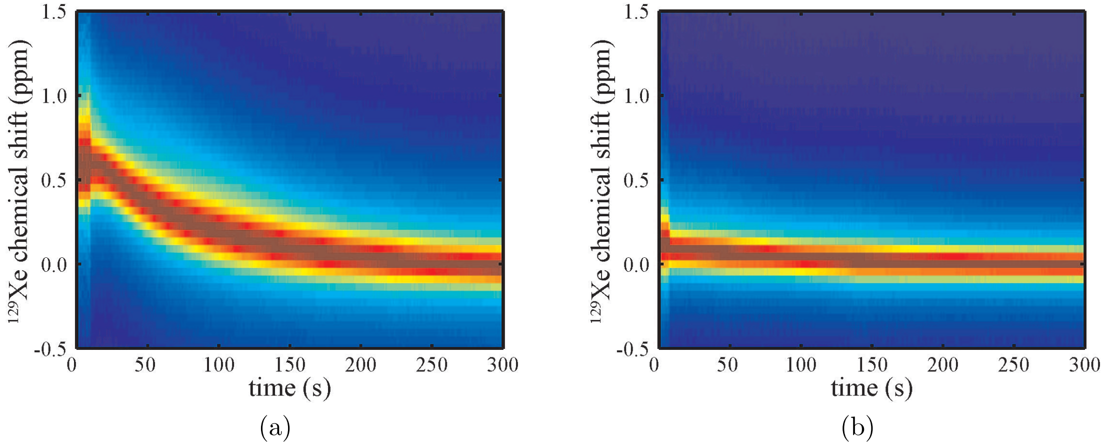

(a) (b)

Figure 3.18: After extinguishing the flame at five seconds by stopping methane and oxygen flow, HP xenon is allowed to flow as the ceramic cools for 5 minutes. (a) For mullite, a large temperature-dependent magnetic susceptibility effect (> 0.5 ppm) is evident in the cooling curve. (b) By switching to 99.8% alumina, the effect is ameliorated. Increasing normalized signal from blue to red.

the combustible gas (methane or DME) broadens the line significantly. The lit flame is even more problematic, as not only the flame itself, but the time it takes for the system to come to constant temperature makes shimming difficult. Shimming at RT with xenon only is optimized and then used to image both the unlit and lit flame. Shimming performed with xenon, nitrogen and water flowing at RT, the same conditions used for the RT tuning and matching.

3.3.5 Orientation and Centering

Significant effort was made to ensure that the centering, orientation, and scaling of the images was correct. The center of the coil was set to sit at the isocenter of the magnet and the sweet spot of the gradient, based on specifications for each (360 and 417 mm from base respectively). To check that the orientation was correct, images were acquired with flow in only three of the bores to see if the images were what was expected. Additionally the probe was rotated between acquisitions, either 45 or 90 degrees to check that the resulting image also turned in that direction (Figure 3.19). A total of fifteen different orientations were tested.

Data in that z-dimension necessitated inversion prior to analysis; therefore, a careful study was made to ensure that the resultant images corresponded with the geometry of the system. Figures 3.19b and 3.19c demonstrate that the xenon signal spreads out from the outlet to the end of the containment tube, as expected.

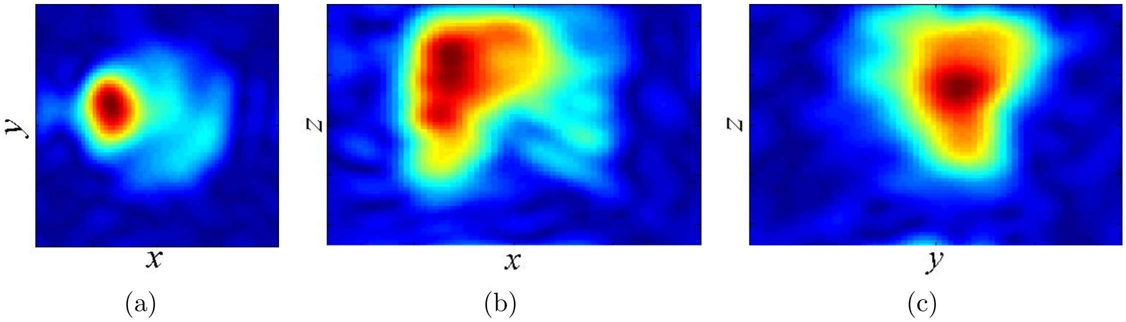

(a) (b) (c)

Figure 3.19: Projection images with xenon flowing in only the bore along the $-x$-axis (at $\theta = 180$ degrees) with oxygen flowing in both y-axis bores: (a) axial (xy), (b) coronal (xz), and (c) sagittal (yz). Note the spreading of the xenon signal as z increases. Fourteen other orientations were tested. Increasing normalized density from blue to red.

3.3.6 Digital Eddy Current Correction

Eddy currents are induced in conducting structures by the rapidly changing magnetic fields during the gradient pulses and work to oppose the field that caused them [9]. Therefore, they will distort the effective gradient from what is intended. The eddy currents also disturb other nearby pulses, including RF pulses. Due to the closely positioned gradient pulses in the velocity sequence, strong eddy currents could cause significant artifacts in the images.

Eddy currents from gradient fields, especially z, were measured to be influencing RF pulses up to 20 ms later using the pulse sequence shown in Figure 3.20. A gradient pulse is applied using one of the gradients, followed by a pulse-acquire after a varying amount of time (T). The effect on peak shape and intensity as T approaches zero (no delay) is then investigated.

Figure 3.20: Pulse sequence employed to test for eddy currents. A gradient pulse (GRAD) is followed by and RF pulse and acquisition (ACQ).

The velocity pulse sequence involves six gradient pulses sandwiched between two RF pulses, the areas of which have been carefully calculated to null appropriate magnetic moments. Substantial eddy currents will result in the accrued phase during the pulses to be different from the desired result. The effect of eddy currents can be ameliorated by using low-power gradient pulses, however, as mentioned previously, high-power pulses are necessary to ensure a short TE.

A full round of digital eddy current correction (DECC) [58] was performed. DECC applies "pre-emphasis" to gradient pulses, based on values input into a parameter file. The first step was to check that the gradient scales were at the appropriate levels. This is accomplished by using a water-filled ping pong ball phantom (40 mm OD, 30.2 mm ID) with water and imaging it with the 40-mm Varian double-resonance probe. The gradient scale/overall values are adjusted until the each of the 2D projection images (axial, coronal, sagittal) are perfectly circular. The optimal scale values were 95, 96, and 100% for the x, y, and z gradients respectively, quite different from the original values of 97, 98, and 100%. This error manifested itself as a distortion in the previously collected images.

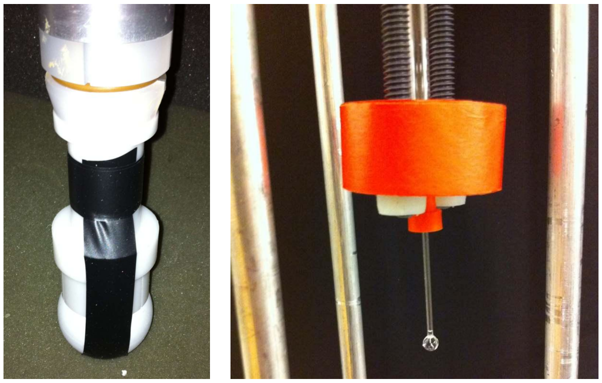
(a) (b)

Figure 3.21: (a) Spherical 40-mm ping pong ball phantom used to determine corrected values for relative gradient scales. (b) Spherical 4-mm point source phantom, which can be positioned at any arbitrary position within the gradient. This phantom was used for determination of the final DECC parameter values.

The second step in DECC involves using a so called "point source" phantom, which is a 4-mm spherical sample which can be placed a specific positions within the gradient volume. In this way, the effect of eddy currents can be compared at the middle of the gradient ($G = 0$) to the extremes of it, up to ±13 mm from the center in each dimension. The optimal values for the DECC correction parameter file were determined after several iterations. These parameters were used for the final CSI and velocity imaging studies.

3.3.7 High-Temperature Thermocouple

In order to calibrate the MRI data, it was necessary to make quantitative measurements of the flame temperature-profile. A high-temperature forward looking infrared (FLIR) camera was investigated (Sierra Pacific Innovations IR996 HT). After discussion with the manufacturer, it was determined that this would not work for the flames in this study. Not only is a specialized camera needed to image temperatures above 800 °C (the IR996 HT had a range up to 2000 °C), but these instruments are unable to visualize gas temperatures. The infrared radiation detected is from the surfaces, which act as black bodies. In order to use a FLIR camera to image flame temperatures, a piece of metal or some other substance would need to be placed within the flame, allowed to equilibrate to the flame temperature, and then imaged.

As FLIR could not aid in getting numerical values for the temperature across the flame easily, it was determined that high-temperature thermocouples were the best approach. Most thermocouples cannot withstand the high temperatures of the flame. Similarly, all of the typical thermocouple coatings will oxidize quickly at elevated temperatures. Therefore, after discussion with a technician at Conax Technologies, it was determined that a "bare wire" thermocouple (one made without insulation) would be best for flames approaching 2000 °C. The thermocouple material able to withstand the highest temperatures without melting is made of tungsten (Conax type W5). However, even this thermocouple does begin to oxidize at the high temperatures, so it eventually fails.

To acquire temperature measurements throughout the flame, the thermocouple wire was coupled to an xyz positioning stage (Figure 3.22a) after passing each of the two leads through opposite bores of an extra alumina combustion tube, which supports the thermocouple tip and allows insulated attachment to the stage. The temperature readings were taken from a calibrated programmable LED indicator (Conax model no. 5714A) and were very noisy, fluctuating by ±100 °C at times. The average temperature at each point was estimated and recorded at each point before moving to the next point. In the first attempt to map temperature in three dimensions (Figure 3.22b), the points were taken in an xyz Cartesian grid ($9 \times 9 \times 5$) designed to match up point for point with the MRI dataset ($9 \times 9 \times 17$). The probe was held stationary, and only the positioning stage was moved.

Thermocouple measurements were made on the open flame, without either the containment or chimney tubes in place. If either of these were in place, sampling would only be possible from above. The data from the first study was asymmetric and highly variable, and it was concluded that air currents from the room HVAC system were causing the flame to flicker and also be hotter on one side of the flame. This was verified by rotating the probe by 180 degrees and resampling.

To circumvent these issues, the second sampling strategy involved radial sampling (Figure 3.22c) with a chimney in place to block some of the room air currents (Figure 3.23a). An indexing head was used to hold the probe in place and rotate it in 15 degree steps. The thermocouple holder was inserted through a slot in the chimney (Figure 3.23b), where it could move along x (now r) and z. In this way data was collected in r, θ, and z (polar coordinates plus height).

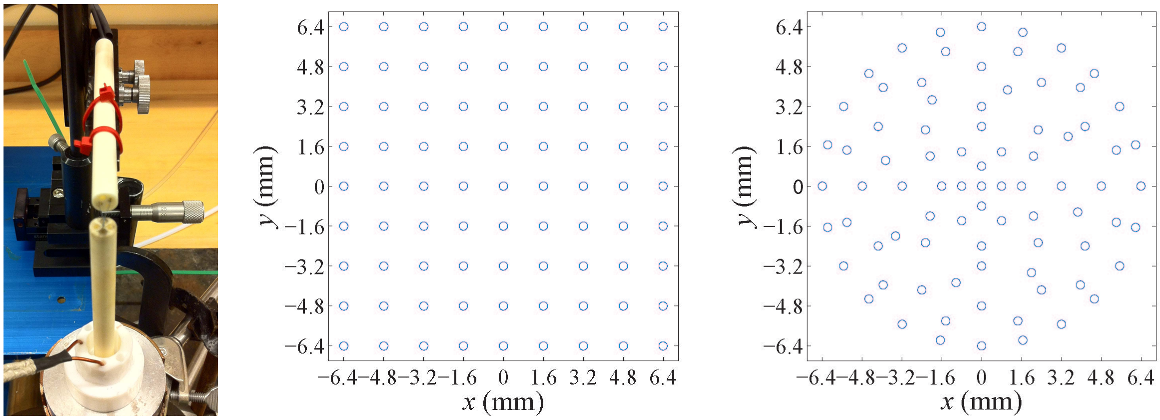

(a) (b) (c)

Figure 3.22: (a) The thermocouple holder (an extra combustion tube) is supported on an xyz stage used for sampling the flame. (b) Initial sampling strategy, Cartesian sampling in x and y at each z slice. (c) Radial sampling at 15 degree increments in θ using indexing head. In both cases 81 points are sampled for each z value.

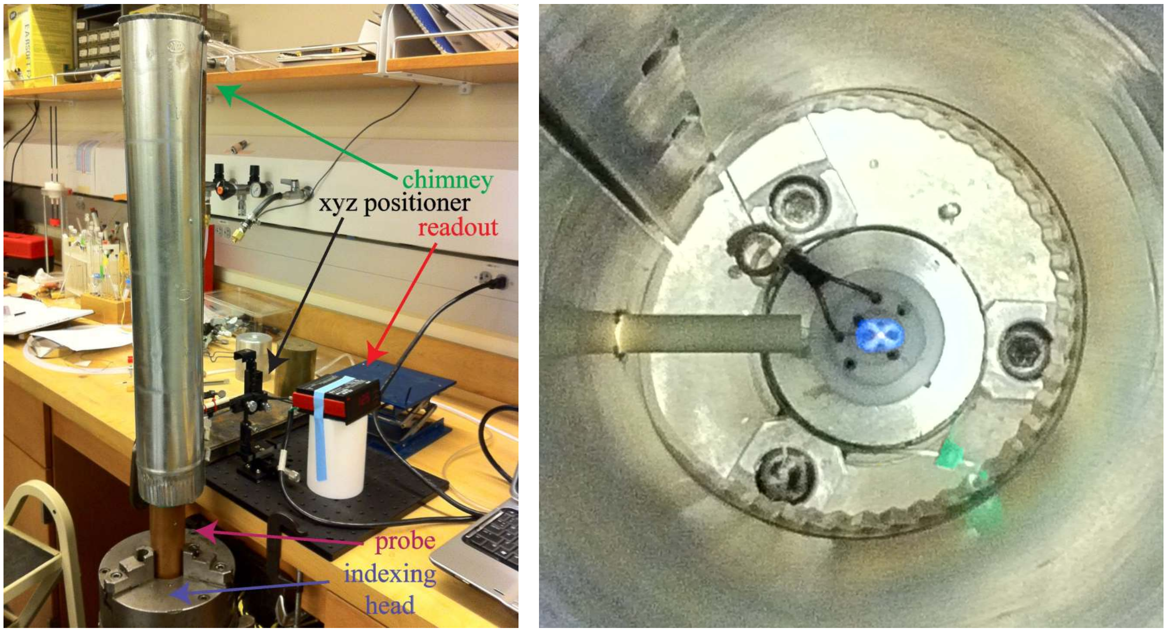

(a) (b)

Figure 3.23: (a) High-temperature thermocouple measurement setup for radial sampling with chimney to block room air currents. (b) View from above inside of chimney, detailing thermocouple at center of flame, supported by an extra combustion tube. The thermocouple holder enters the chimney through a vertical slot in the chimney. The RF coil has been bent out of the way for sampling.

Chapter 4

Combustion Results

4.1 Data Collection and Analysis

4.1.1 Data Collection

Chemical shift imaging (CSI) and velocimetry of ^{129}Xe in enclosed methane and dimethyl ether (DME) flames were performed using the apparatus described in Chapter 3. The optimized final data presented here is from four-dimensional (4D) data sets, with three spatial dimensions and one velocity dimension associated with each free induction decay (FID). The number of phase-encodes were $9 \times 9 \times 17 \times 3$ for the $x \times y \times z \times v_i$ dimensions, resulting in 4131 points in k-space. Each point consists of a four 500 ms phase cycles, 2 s per full cycle, with the full experiment in one velocity dimension v_i (where i is x, y, or z) taking $\approx$ 2.3 hours. This was repeated for the unlit jet and lit flame and the two datasets were compared.

A MATLAB processing script was written to convert the large, multidimensional data sets into density, chemical shift, and velocity arrays for analysis. The m-file **process_csi_vel_ac** (Appendix C.4) is flexible enough to accept and process data from any array size, determining the dimensionality from the parameter file. Front-end control over the level of zero-filling is provided, and the zero-filled density (**img**), CSI (**csimg**), and velocity (**velocity**) arrays are automatically saved.

As described below, the binary data are first read and reshaped, then apodized in the temporal and spatial dimensions. Fast Fourier transform (FFT) of the time dimension, with zero-filling, is followed by spectral range determination from the generated spectra. After FFT from k-space to image space, with empirically optimized levels of zero-filling, xenon density, chemical shift and velocity is determined for each voxel. Finally a spatial position, based on the computed fields of view (FOV$_x$, FOV$_y$, FOV$_z$) and spatial resolutions (δ_x, δ_y, δ_z), is assigned to each voxel.

4.1.2 Read and Reshape Data

The raw VnmrJ data files, which contain FID data for arrays in up to four dimensions (three each in position and one in velocity) must first be read and reshaped into workable MATLAB arrays. The FID are stored by VnmrJ as a binary data file with a single "file header" and "block headers" for each individual FID. The **fid** file is read by the MATLAB function **readfid** (Appendix C.2), which extracts the data into a MATLAB vector. The headers are extracted into MATLAB structure arrays. The quadrature data are also combined into complex data in this step.

In order to determine the size of the spatial and velocity arrays, the parameter file **procpar** is read using the MATLAB function **readpar** (Appendix C.3). These parameter data are extracted and used to determine how the data arrays should be reshaped, such that each dimension is accounted for in the new array. Knowledge of the array order is important, as only the parameter array sizes and individual values (gradient lobe amplitudes and times) are stored in the parameter file, but not the array order.

For this reason the array order is always set to: **gacx**, **gacy**, **gacz**, then the velocity gradient (**gvx**, **gvy**, or **gvz**). Here, **gacx** is the pulse sequence variable for the data acquisition (DAQ) value of the first $\underline{\text{g}}$radient lobe that is velocity and $\underline{\text{a}}$cceleration $\underline{\text{c}}$ompensated and position-encoding in $\underline{x}$, and **gvz** is the DAQ value of the first $\underline{\text{g}}$radient lobe that is position and acceleration compensated and $\underline{\text{v}}$elocity-encoding in $\underline{z}$ (and so on). The full range of the gradient strengths are represented in the DAQ input by a signed 16-bit integer with values between −32,767 and +32,767 and can be converted to gradient strength:

$$G = \frac{\text{DAQ}}{32{,}767}\,(100\ \text{G cm}^{-1}). \tag{4.1}$$

The velocity-encoding lobes are placed in the lowest array order so that they are arrayed in sequential acquisitions; otherwise the three phase-encodes could be separated by hours. The velocity dimension has three encodes, negative, zero, and positive. The velocity-encode with zero gradient applied is used for the generation of the density images and CSI, while the other two are used for velocity determination. All gradients are arrayed from negative to positive DAQ values.

4.1.3 Apodization

If z-gradients were employed during the acquisition, the k-space data in that dimension is flipped, as discussed in Section 3.3.5. The data points prior to the spin echo are then trimmed. The parameters **enct** (encoding time; equal to $\frac{1}{2}$ the echo time, TE) and **sw** (spectral width) are used to determine the number of points to trim; this ends up being the first three points because the echo is at 4 ms and the points are every 1 ms (1 kHz spectral width). After these preliminary data modifications, each dimension (excluding the velocity dimension) is apodized.

The time dimension is apodized by fitting an exponential to the FID at the center of k-space:

$$|s(t)| = a\, e^{-t/T_2^*}, \tag{4.2}$$

and then applying this exponential filter to the full data set (Figure 4.1). The absolute value of the FID is trimmed after it has decayed to 13.5% (e^{-2}) of its original amplitude (a), prior to fitting, to avoid applying the natural logarithm to zero. Then a first degree polynomial is fit to the natural logarithm versus time, to determine λ ($1/T_2$):

$$\ln|s(t)| = (-\lambda)\, t + \ln(a). \tag{4.3}$$

The T_2 of the unlit jet is ≈ 16 ms and ≈ 15 ms for the lit flame (≈ 20 Hz linewidth).

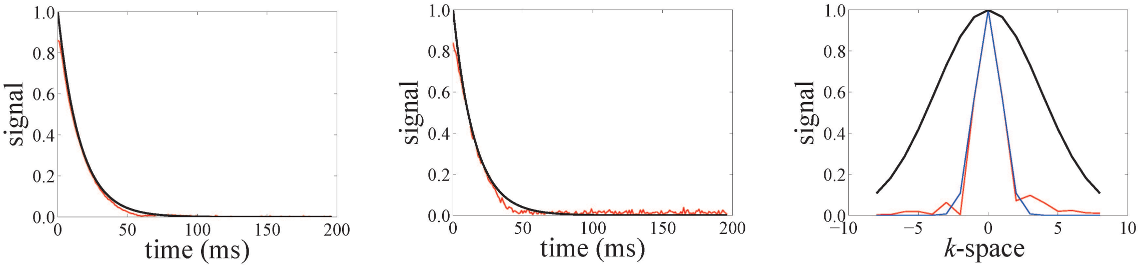

(a) (b) (c)

Figure 4.1: Apodization of the time dimension of the (a) unlit and (b) lit flame fits an exponential decay (black) to the absolute value of the FID at the center of k-space (red). The filter is then applied to each FID in the data set. (c) Apodization of the k-space dimensions fits a gaussian distribution (blue) to the center of the echo at each point in a particular k-space dimension, with the data from the k_z-dimension shown here (red). The resulting σ is multiplied by four to create the gaussian filter (black).

The k-space dimensions are apodized by fitting a gaussian to the first data points, the peak of the echo, $a(k)$, of the array of gradient values for the FIDs when the other gradient values are zero:

$$|a(k)| = \frac{1}{\sqrt{2\,\pi\,\sigma^2}}\, e^{-\frac{(k-\mu)^2}{2\,\sigma^2}}. \tag{4.4}$$

The apodization was attenuated by modifying the standard deviation (σ) of the applied fit,

$$\ln|a(k)| = (-\frac{1}{2\,\sigma^2})k^2 + \dots\,, \tag{4.5}$$

typically by multiplying this value by four prior to applying the filter (Figure 4.1c). The value of 4σ was chosen empirically, after examination of images using various filter widths (Figure 4.2). The velocity dimension is not apodized, and as mentioned in Section 4.1.2, the dimension with no velocity gradients applied is used for CSI.

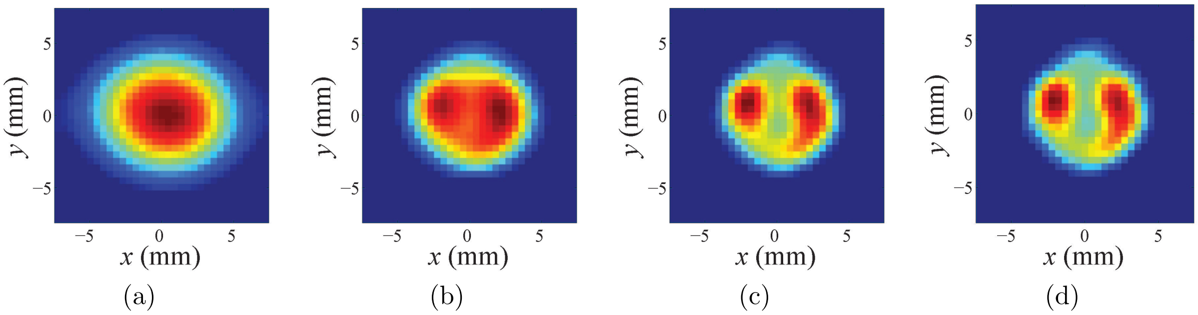

(a) (b) (c) (d)

Figure 4.2: Examples of different levels of gaussian apodization, varying the width of the filter as compared to the fit: (a) 1σ, (b) 2σ, (c) 4σ, and (d) 6σ. The 4σ filter was chosen as the optimal level. All images are axial slices at $z = 0$, zero-filled from 9×9 to 33×33.

4.1.4 Fast Fourier Transform and Zero-Filling

The next step is to perform FFT in each dimension to transform the time/k-space data to frequency/image-space. This is done with some level of zero-filling, in order to increase the digital resolution. The MATLAB function **fft** pads the data with zeros based on the dimensions input as one of the arguments. The time dimension is equal in length to the acquisition time, which is 200 ms, with one data point per ms (minus the 3 points trimmed previously). These data are zero-filled by a factor of 2, by adding zeros to the end of each FID to 400 points prior to FFT, which improves the digital resolution from 5 Hz (0.045 ppm) to 2.5 Hz (0.023 ppm).

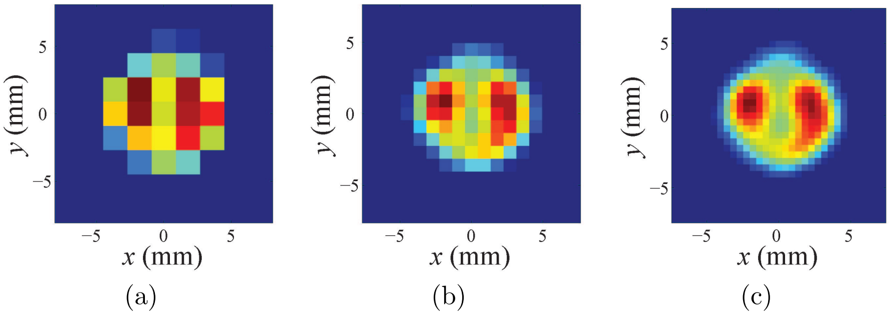

(a) (b) (c)

Figure 4.3: (a) Original array size: 9×9. (b) Zero-filling once to 17×17 gives some definition to the two xenon bores along the x-axis. (c) Zero-filling twice to 33×33 increases digital resolution to 0.4 mm.

The spectral range is determined by summing the frequency data across the entire data set to determine the frequency with the maximum intensity within the full experimental spectral width of 1000 Hz. Data within ±100 Hz (an approximately ±1.8 ppm range) of this frequency are considered part of the spectral range. All other data are trimmed from the data set. Each of the k-space dimensions (except velocity) are then transformed into image space, with desired levels of zero-filling. The density image array, **img**, is generated by summing the frequency data in each voxel. The data in low density voxels, which are below a certain threshold (typically 10% of maximum), is replaced by not a number (**NaN**).

4.1.5 Chemical Shift Determination

The chemical shift at each point within the spectral range is determined by dividing the relative Larmor frequency ($\Omega^0/2\pi$) by the transmitter frequency ($\mathbf{sfrq} = \omega^0_{\mathrm{Xe(ref)}}/2\pi$):

$$\delta = \frac{\Omega^0/2\pi - \mathbf{tof}}{\omega^0_{\mathrm{Xe(ref)}}/2\pi}. \tag{4.6}$$

The offset frequency (**tof**) would normally need to be taken into account as shown in Equation 4.6, but in all combustion studies this value was set to zero.

The chemical shift is determined for each voxel by examining the associated spectra. The index of the frequency with the maximum signal is used to assign a chemical shift value from the spectral range. A single chemical shift for each voxel results from this analysis and the CSI array is saved as **csimg**. If more than one chemical shift is present, then only the peak with the maximum intensity is reported, due to the manner in which the chemical shifts are determined. However, examination of individual spectra suggests that two peaks are rarely present in the same voxel, the second peak a small shoulder of the main peak.

4.1.6 Field of View and Resolution

The desired FOV is used to determine the gradient DAQ values and pulse lengths prior to the start of the experiment. The image size (14.40 × 14.40 × 27.20 mm, $x \times y \times z$) was chosen to be slightly larger than the flame size (9.53 × 25.4 mm, diameter × height). For the three-lobed, equal length, triangular gradient waveforms used to encode position,

$$\mathrm{FOV} = \frac{89}{48}\frac{N_{\mathrm{pe}} - 1}{\frac{\gamma}{2\pi} G_1 T}, \tag{4.7}$$

where N_{pe} is the number of phase-encodes, G_1 is the peak strength of the first gradient lobe (see Equation 4.1), and T is the length of each gradient lobe. This equation results from substituting the summed area of the gradient waveform,

$$A = \frac{24}{89} G_1 T, \tag{4.8}$$

into Equation 2.14. See Appendix B.2 for the calculation of this area. The peak gradient strengths employed for the studies presented here were ±54.665 G cm^{-1} (17,912 DAQ units) for G_x and G_y and ±57.888 G cm^{-1} (18,968 DAQ units) for G_z.

The original spatial resolution can be calculated using Equation 2.15; however, in order to calculate the digital resolution between the zero-filled points, N_{pe} should be replaced with the total number of points in the zero-filled space (N_{ZF}):

$$\delta_{\text{ZF}} = \frac{\text{FOV}}{N_{\text{ZF}}}. \tag{4.9}$$

The values used in the imaging studies are presented in Table 4.1. An odd number of spatial phase-encodes are used, and the zero-filled array size is also odd, so that the middle data points in the transformed data sets correspond to the zero points in image space.

Table 4.1: Study FOV and resolution.

Parameter	**Original**	**Zero-Filled**
N_{pe} ($x \times y \times z$)	$9 \times 9 \times 17$	$33 \times 33 \times 65$
array size (points)	1377	70785
FOV_x (mm)	14.40	14.40
FOV_y (mm)	14.40	14.40
FOV_z (mm)	27.20	27.20
$x_{\max}$ (mm)	7.20	7.20
$y_{\max}$ (mm)	7.20	7.20
$z_{\max}$ (mm)	13.60	13.60
δ_x (mm)	1.6	0.4
δ_y (mm)	1.6	0.4
δ_z (mm)	1.6	0.4

4.1.7 Velocity Determination

The phase difference between the signals encoded by the two bipolar gradient waveforms is used to determine the velocity at each voxel. The summed data in the two xenon density **img** arrays have complex amplitudes, which can be represented by:

$$a_{\text{neg}} = |a_{\text{neg}}|\, e^{i\,\phi_{\text{neg}}} \qquad \text{and} \qquad a_{\text{pos}} = |a_{\text{pos}}|\, e^{i\,\phi_{\text{pos}}}. \tag{4.10}$$

To calculate the phase difference in MATLAB, the negative array is multiplied point-by-point with the complex conjugate of the positive array:

$$|a_{\text{neg}}|\, e^{i\,\phi_{\text{neg}}} \times |a_{\text{pos}}|\, e^{-i\,\phi_{\text{pos}}} = |a_{\text{neg}}\, a_{\text{pos}}|\, e^{i\,(\phi_{\text{neg}}-\phi_{\text{pos}})}. \tag{4.11}$$

Then, the angle of each point is determined to produce an array of $\Delta\phi$ values.

The gradient DAQ values chosen determine the aliasing velocity (VENC) as defined by Equation 2.20. For the equal length, three-lobed, position and acceleration compensated gradient waveforms used to phase-encode velocity (ratio of $\frac{2}{2}:-\frac{3}{2}:\frac{1}{2}$), the change in the first gradient moment is

$$|\Delta m_1| = \frac{1}{2}\,|G_1|\,T^2, \tag{4.12}$$

where G_1 is the peak strength of the first gradient lobe and T is the length of each lobe. In the data presented here, VENC was selected to be 500 cm s^{-1}, which can be encoded with 200 µs lobes, first gradient lobe peak strength (G_1) of 42.45 G cm^{-1} (13,911 DAQ units). Note that the second gradient lobe actually has a higher peak strength (G_2 = 63.68 G cm^{-1}), due to the ratios necessary for position and acceleration compensation. The same VENC was used in all three dimensions. By combining Equations 2.19 and refeqn:velocity, the velocity can be calculated at each point:

$$v = (500\ \text{cm s}^{-1})\,\frac{\Delta\phi}{\pi}. \tag{4.13}$$

The velocity array is saved as **velocity** and a separate parameter **velplane** indicates the direction. This was repeated for each dimension (v_x, v_y, and v_z) so that a three-dimensional (3D) velocity vector at each point could be formed. The magnitude of these vectors was calculated to determine the scalar velocity (speed) at each point.

4.2 Results

4.2.1 Density Data

To generate ^{129}Xe density images, the absolute value of the complex data points in the **img** array is taken. This is a 4D data set, including a velocity dimension. The velocity data set without velocity-encoding is used to generate density images and CSI. Data are presented here for both the unlit jet and lit methane flames. Only the methane data are presented, although the DME data led to similar conclusion. The unlit jet images are with all gases flowing: hyperpolarized (HP) xenon mixture, methane, and oxygen. During these acquisitions the cooling/clearance nitrogen gas and water flow were also on (Section 3.1.2).

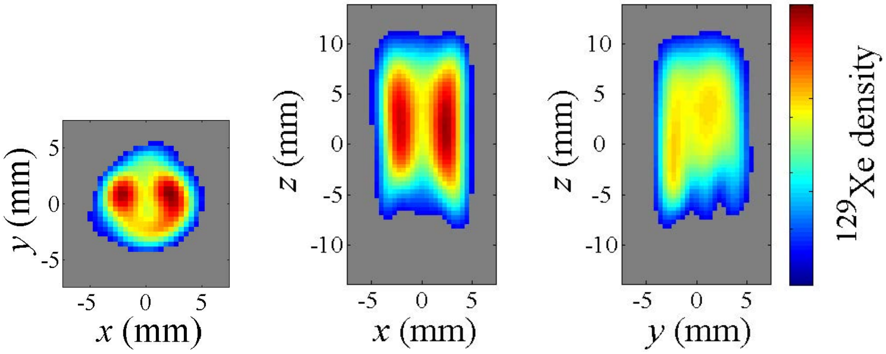

(a) (b) (c)

Figure 4.4: Normalized ^{129}Xe density images of the unlit methane jet, with all gases flowing: (a) axial slice at $z = 0$, (b) coronal slice at $y = 0$, (c) sagittal slice at $x = 0$. Highest density occurs along paths of xenon/methane bore outlets, throughout length of containment tube.

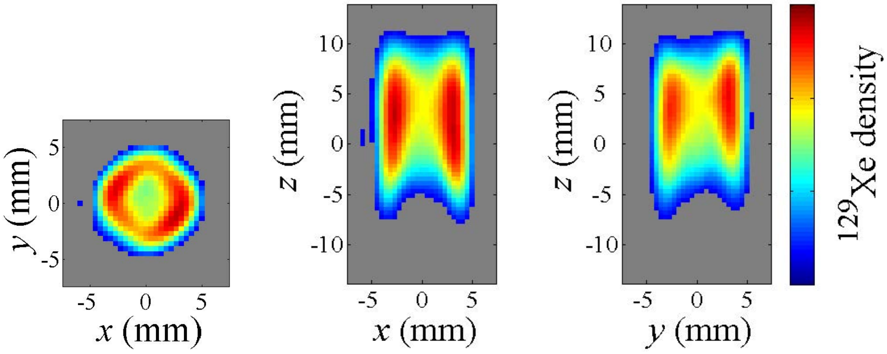

(a) (b) (c)

Figure 4.5: Normalized ^{129}Xe density images of the lit methane flame: (a) axial slice at $z = 0$, (b) coronal slice at $y = 0$, (c) sagittal slice at $x = 0$. Significant xenon density present along y-axis, suggesting mixing not observed in the unlit jet.

The two-dimensional (2D) density images shown in Figures 4.4 and 4.5 are actually slices taken from the 3D data set. The particular slices taken are along each of the planes at the center of image space. The density in the images is indicated with a color map in which normalized density increases from blue to red. The unlit jet and lit flame images are normalized independently; the signal is predictably lower in the flame data. The low intensity voxels that were set to **NaN** during processing are displayed as gray (2D images) or transparent (3D images).

In the unlit images the xenon flow from the two bores along the x-axis is clearly seen in an axial slice (Figure 4.4a). This separation persists from the base to the top of the jet, as can be observed in Figures 4.4b and 4.4c, and is a consequence of the strong oxygen flow from the bores along the y-axis, which prevents xenon from diffusing into that space. When separate images were acquired with no oxygen flow, the xenon density is spread throughout the containment tube and image.

The density images of the lit flame indicate that the xenon is diffusing away from the x-axis and into the regions where oxygen flow had prevented it from traveling in the unlit jet. This mixing is clearly evident in the axial slice (Figure 4.4a) and also from the higher density present in the sagittal slice (Figure 4.4c). The differences between the unlit and lit images clearly indicate a change in the system, even without investigating the changes in chemical shift or velocity.

4.2.2 CSI Data

The array of chemical shifts, **csimg**, is generated as described in Section 4.1.5 and requires no further manipulation. As with the density data, only the data with zero velocity-encode is used. The chemical shift reference is room temperature (RT) HP xenon, as described previously. The entire 3D CSI with xenon only flowing displays a homogenous chemical shift around zero (not shown).

The zero slices of the unlit jet are shown in Figure 4.6 and indicate an ≈ 0.5 ppm increase in chemical shift as a result of the combined effect of the change in xenon density and interactions with both oxygen and methane. Please note that in all of the CSI figures, the colorbar has been inverted so that lower chemical shifts are red. There is nearly 1 ppm of chemical shift contrast across the flame, with δ decreasing with increasing height (z). It is unclear whether the high chemical shifts at the base of the jet (Figures 4.6b and 4.6c) are real or due to a lower xenon spin density (low SNR).

In the lit flame (Figure 4.7), the chemical shift decreases, almost back to the reference value ($\delta = 0$ ppm). Unlike the unlit jet, where the chemical shift decreased with increasing height, the lit flame displays the reverse trend. This is likely due to the higher temperatures at the base of the flame, which cause an upfield shift.

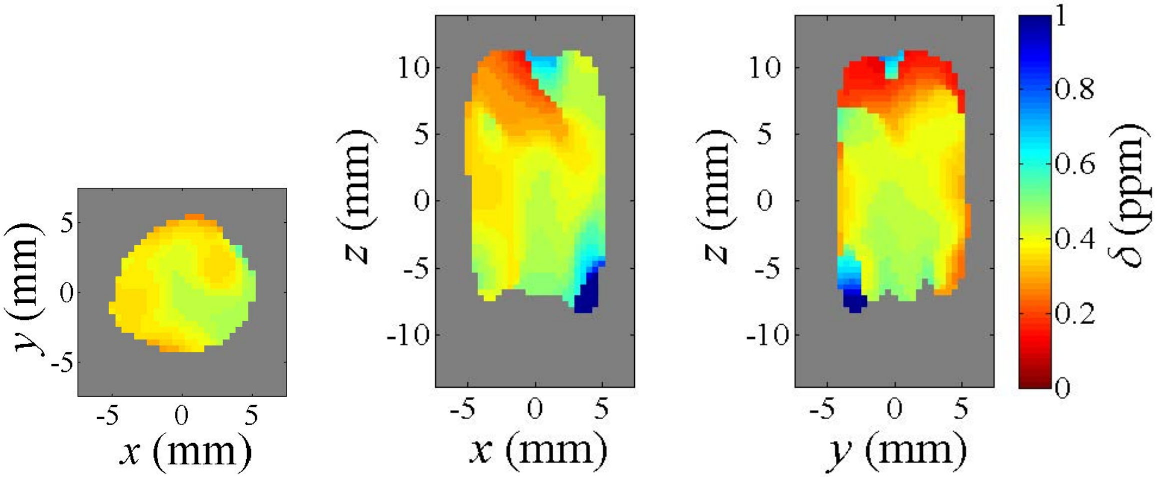

(a) (b) (c)

Figure 4.6: ^{129}Xe CSI of the unlit methane jet, with all gases flowing: (a) axial slice at $z = 0$, (b) coronal slice at $y = 0$, (c) sagittal slice at $x = 0$. Chemical shift decreases from base to top of jet, with highest chemical shift observed near oxygen outlet. Note inverted colorbar.

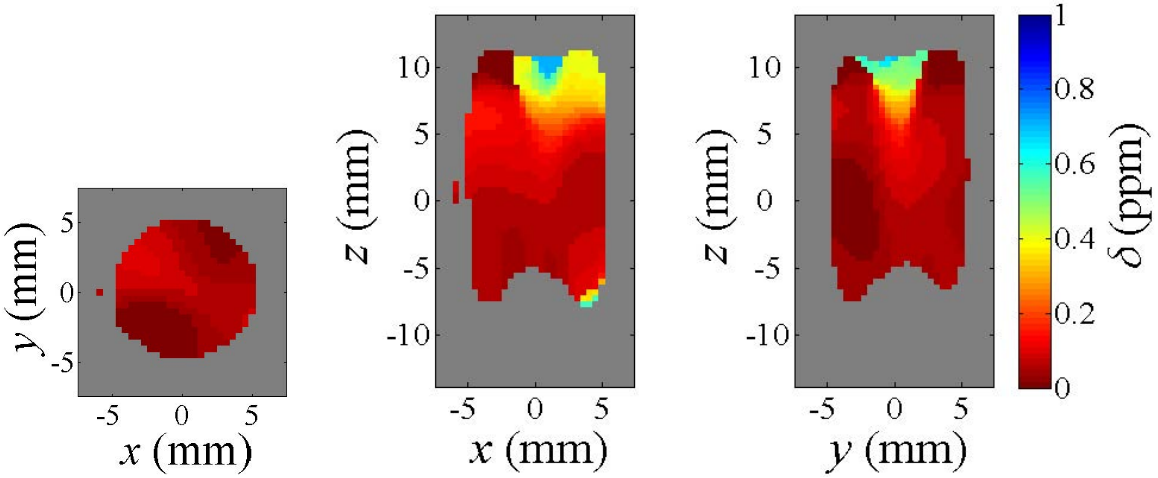

(a) (b) (c)

Figure 4.7: ^{129}Xe CSI of the lit methane flame: (a) axial slice at $z = 0$, (b) coronal slice at $y = 0$, (c) sagittal slice at $x = 0$. Overall decrease in chemical shift to near zero (RT reference in the absence of oxygen). In contrast to unlit jet, chemical shift increases from base to top of flame. Note inverted colorbar.

To more easily visualize the 3D chemical shift distribution across the full extent of the containment tube, slices of data along axial, coronal, and sagittal planes are presented for the unlit jet (Figure 4.8) and lit flame (Figure 4.9).

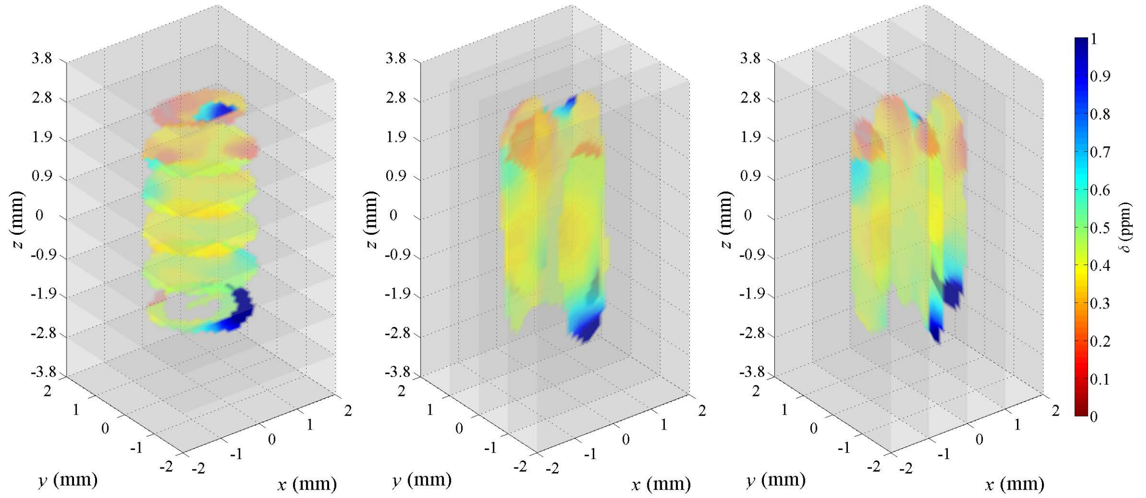

Figure 4.8: Axial, coronal, and sagittal slices of the 3D ^{129}Xe CSI of the unlit methane jet, acquired with all gases flowing. Nine axial slices and five each of coronal and sagittal are shown, with the low density voxels transparent. Note inverted colorbar.

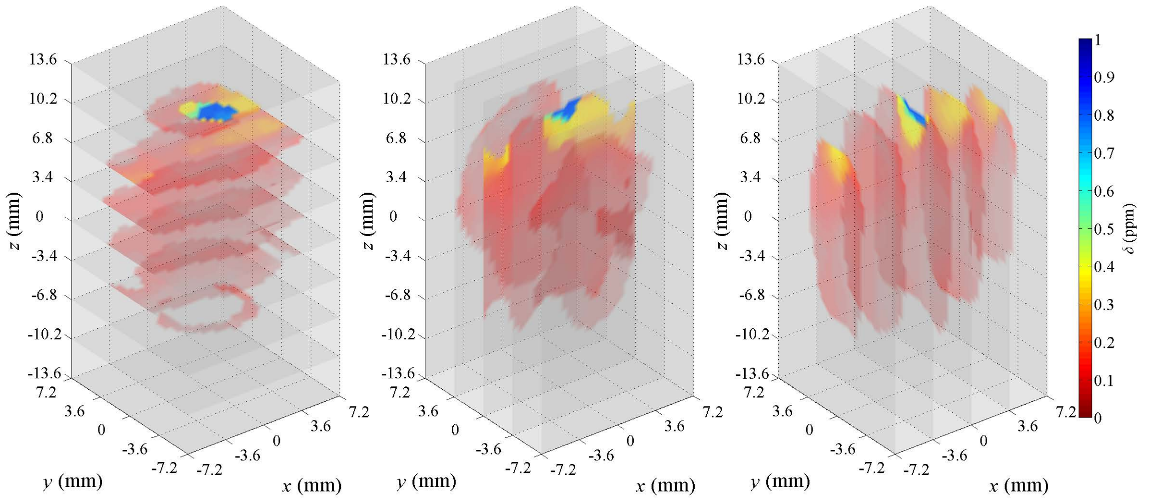

Figure 4.9: Axial, coronal, and sagittal slices of the 3D ^{129}Xe CSI of the lit methane diffusion flame. Nine axial slices and five each of coronal and sagittal are shown, with the low density voxels transparent. Note inverted colorbar.

4.2.3 Velocity Data

The individual velocity components of each voxel are calculated as described in Section 4.1.7, for the lit and unlit flame. The maximum magnitudes of the velocities were close to what was expected based on the flow rates calculated in Section 3.2.1. However, the velocity images for each component of the velocity each displayed an unexplained spatial dependence, where the velocity was greatest (positive values) at the negative part of the respective image space, approximately zero at the center of images space, and lowest (negative) at the positive part of the respective image space (Figure 4.10). For instance, v_z is approximately $+300$ cm s^{-1} (up) at the base of the flame (and coil), passes through 0 cm s^{-1} at the center, and then is -300 cm s^{-1} (down) at the top. The other components of velocity, v_x and v_z, display similar trends, with lower overall magnitudes (< 100 cm s^{-1}). It was confirmed that phase wrapping is not to blame for this phenomenon, as the maximum phase difference observed was far less than π. The VENC of 500 cm s^{-1} would need to exceeded for the phase to wrap.

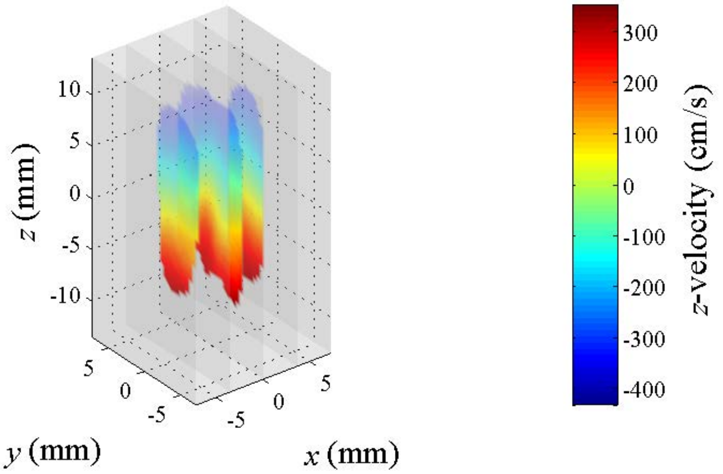

Figure 4.10: Sagittal slices of the v_z data. The imaged velocity changes direction across the center of the flame for unexplained reasons. This phenomenon is also observed for v_x and v_y.

A significant effort was undertaken to correct for eddy currents using digital eddy current correction (DECC). The DECC process is described in Section 3.3.6. Following DECC, the velocity images did not change. Ideally, velocity imaging of water at a known flow rate would be undertaken; however, the combustion probe is only capable of imaging ^{129}Xe, and would need to be significantly altered to allow water imaging. Therefore, the velocity imaging study will be attempted with a modified pulse sequence.

The velocity images themselves did not present the quantitative data that were desired. However, by subtracting the velocities of the unlit data from that of the lit, qualitative maps of velocity changes can be generated. These "velocity difference" images are presented in Figure 4.11 (v_z difference) and Figure 4.12 (speed difference). In both of these images, the most notable change is an increase in velocity near the base of the flame. The speed difference image demonstrates that this change is not dominated by changes in v_z but has significant contributions from v_x and v_y.

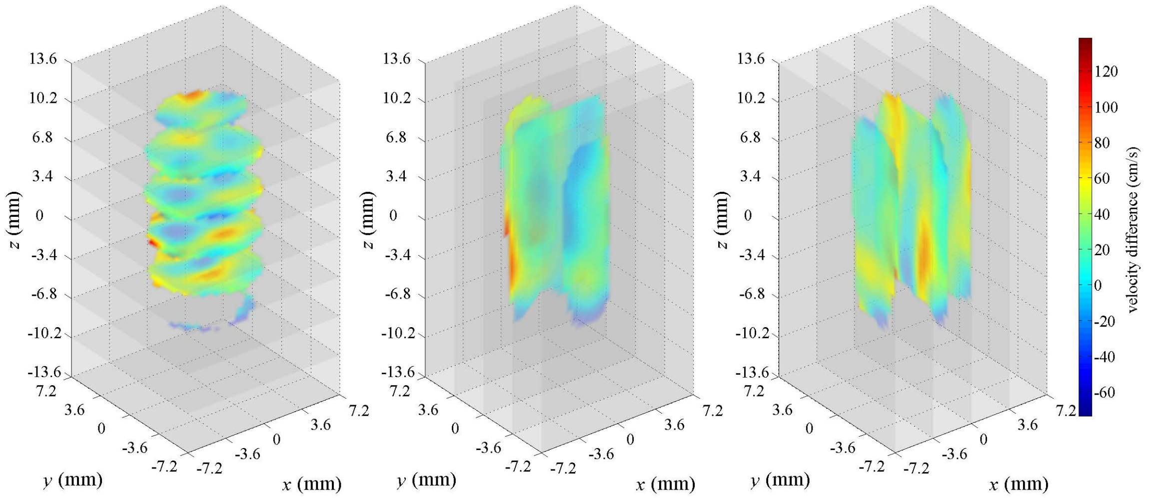

Figure 4.11: Slices of the velocity difference (lit minus unlit methane flame) along the z-axis (v_z). Calculated velocity was subtracted at each point of the zero-filled data set. Red indicates an increased velocity when the flame is lit; blue a decrease.

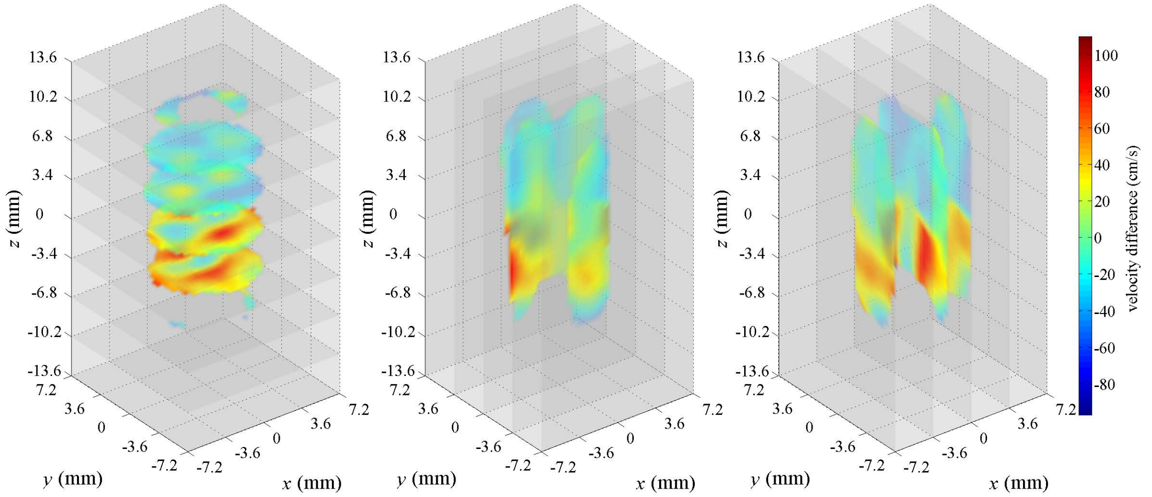

Figure 4.12: Slices of the speed difference (lit minus unlit methane flame). The magnitude of the full velocity vector (v_x, v_y, v_z) was subtracted at each point of the zero-filled data set. Red indicates an increased velocity when the flame is lit; blue a decrease.

4.2.4 Thermocouple Data

The data collected from the high-temperature thermocouple studies was interpolated in three dimensions, depending on the manner in which it was collected. An explanation of the interpolation procedure can be found in Appendix B.3. As described in Section 3.3.7, the data collected along a Cartesian coordinate system is asymmetric, a consequence of the effect of the room air currents on the flame (Figure 4.13). The thermocouple data collected using radial sampling, and with a chimney in place, was more symmetric (Figure 4.14). The recorded temperatures were also lower.

In both cases the temperatures at the base of the flame were much greater than those at the top of the flame, as expected. The collection of these data was very tedious and while the probe can be positioned precisely, the location and size of the sensitive region of the thermocouple wire could not be accurately defined. The readings also fluctuated significantly (up to hundreds of degrees). The use of thermocouples to measure flame temperatures, while it can be done rather cheaply, is neither easy nor accurate. It also is not possible for a confined flame, as these studies needed to be done with the containment tube not in place.

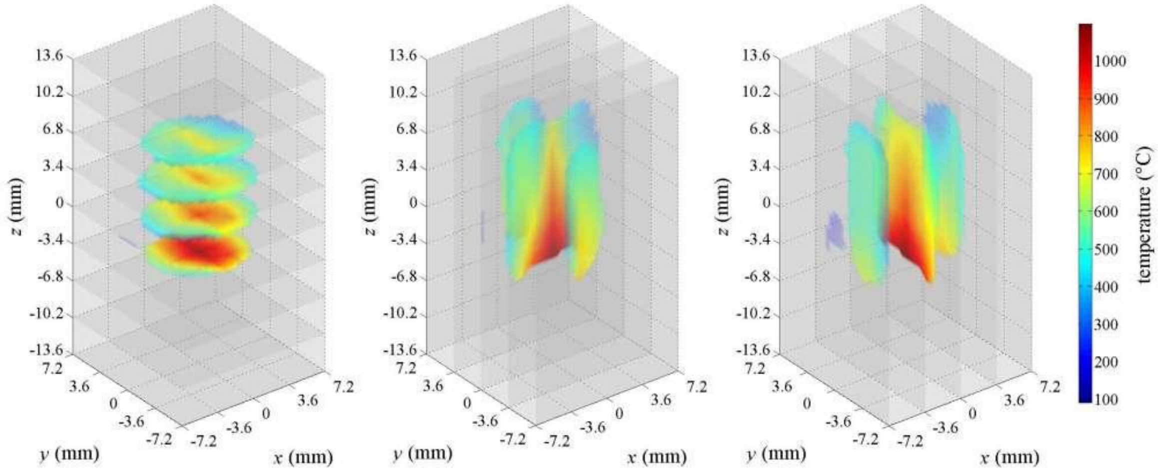

Figure 4.13: Thermocouple data collected from the methane flame along a Cartesian grid pattern. Room air currents caused asymmetry of the flame and higher temperatures overall.

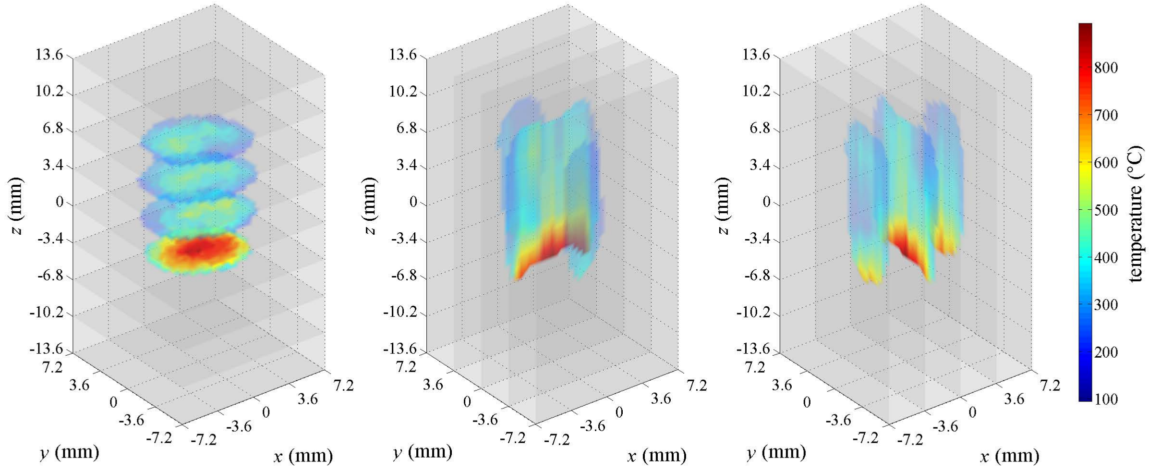

Figure 4.14: Thermocouple data collected from the methane flame with a radial sampling strategy in a chimney to prevent room air currents from disrupting the flame. The data are more symmetric that the Cartesian data, but lower in temperature overall.

4.3 Conclusions and Outlook

4.3.1 Qualitative Images of Flames

HP ^{129}Xe MRI is a powerful technique for visualizing the properties and dynamics of combustion processes. The local changes within an unlit jet of combustible gas and the lit flame can be observed with high spatial resolution, even within opaque devices. Unlike proton images, which suffer from low polarization, the enhanced sensitivity afforded by the use of HP xenon enables faster acquisitions, with less signal averaging.

Information about the diffusion and mixing of gases can be extracted from the spin density images through comparison of images acquired under various conditions. Ignition of the combustible gas jet changes the path of the xenon nuclei through the flame region, which can be seen by comparison of the lit flame and unlit jet. ^{129}Xe can also be used a sensor of local environment due to the dependence of the chemical shift on temperature, density, and interactions with other gases and surfaces. When comparing the CSI of the unlit jet and lit flame, a significant upfield chemical shift is observed in the flame region.

The acquisition of velocity information from the fast moving nuclei enables the visualization of the mixing of gases within a diffusion flame. The images acquired in the present study are insufficient for a true quantitative analysis; however, the velocity difference between the lit flame and unlit jet allow qualitative analysis of the regions where change is significant, namely the lower flame region.

4.3.2 Extracting Temperature Information

Extracting quantitative temperature information from the CSI data set would require decoupling the effect of temperature [34] on the chemical shift from other factors such as xenon density [32] and interactions with other gases (oxygen, methane, DME) [33, 35] and surfaces [15] (Table 4.2). This theoretical analysis is beyond the scope of this this work.

Table 4.2: Chemical shift contributions.

Cause	**Proportionality with δ**
xenon density	direct
oxygen density	direct
fuel density	direct
temperature	inverse
surfaces	unknown

Attempts were made to measure high-temperature HP xenon in the absence of oxygen, in order to determine the effect of temperature alone on the chemical shift. A smaller ceramic tube was glued into one the bores of the combustion tube, so that xenon could travel through a lit flame without interacting with the other gases. The room temperature spectrum of gas flowing through the single bore contained two peaks. The upfield peak was small and broad from the fast flow of xenon through the small tube. The large and narrow downfield peak was most likely HP xenon that had leaked around the imperfect glue seal. The width of the peak of interest would make visualizing small chemical shifts challenging. This fact, combined with the likely failure of the glue at high temperatures led to the termination of this study. Ideally, a comprehensive study of the chemical shift, while heating a sealed vessel of pure xenon, should be performed.

4.3.3 Outlook

Analyses of enclosed high-temperature combustion processes are technically challenging. The use of HP xenon MRI can enable investigations of reactions that are difficult or impossible to visualize by any other technique. The multidimensional images generated in HP xenon studies contain a wealth of information about diffusion and mixing, the temperature and local environment, and flow velocity.

The imaging of smoldering combustion is one area where HP xenon MRI could make an impact, and is currently studied using thermocouples and optical techniques, neither of which enable 3D imaging inside of opaque systems. Specifically the transition from smoldering combustion to flame is of interest in this field [4]. HP xenon could be flowed through non-metallic analogs of the devices used to study these systems. Fast acquisitions could generate qualitative density images and CSI sufficient to study the dynamics of this event

The analysis of flames in microchannels [52] could also be enhanced by the use of HP xenon MRI. The micro-turbine engines being developed for micro electro mechanical systems (MEMS) devices [18] are a potential model system of interest due to the lack of optimal characterization techniques for these opaque devices. HP xenon MRI could also make an impact in the temperature and air flow profiling of macroscopic composite turbine blades and airfoils, currently performed using water MRI and particle velocimetry.

Each of these measurements could benefit from the use of remote detection [43]. This would involve encoding at the region of interest and then compressing the combustion products for more sensitive detection at a remote, filling factor-matched coil. Time-of-flight images can be acquired using this technique. The well-defined channels in MEMS devices would allow patterning of coils directly onto these devices, without the need for a separate compression mechanism. Improvement of the velocity imaging protocol will also enable quantitative analyses of the flame region itself.

Bibliography

[1] Anala, S., Pavlovskaya, G. E., Pichumani, P., Dieken, T. J., Olsen, M. D., and Meersmann, T. In Situ NMR Spectroscopy of Combustion. *Journal of the American Chemical Society 125*, 43 (Oct. 2003), 13298–13302.

[2] Andersen, A., and Carter, E. A. Insight into Selected Reactions in Low-Temperature Dimethyl Ether Combustion from Born-Oppenheimer Molecular Dynamics. *The Journal of Physical Chemistry A 110*, 4 (Mar. 2006), 1393–1407.

[3] Balcom, B. J., MacGregor, R. P., Beyea, S. D., Green, D. P., Armstrong, R. L., and Bremner, T. W. Single-Point Ramped Imaging with T_1 Enhancement (SPRITE). *Journal of Magnetic Resonance, Series A 123*, 1 (Nov. 1996), 131–134.

[4] Bar-Ilan, A., Putzeys, O. M., Rein, G., Fernandez-Pello, A. C., and Urban, D. L. Transition From Forward Smoldering to Flaming in Small Polyurethane Foam Samples. *Proceedings of the Combustion Institute 30*, 2 (Jan. 2005), 2295–2302.

[5] Bartik, K., Choquet, P., Constantinesco, A., Duhamel, G., Fraissard, J., Hyacinthe, J.-N., Jokisaari, J., Locci, E., Lowery, T. J., Luhmer, M., Meersmann, T., Moudrakovski, I. L., Pavlovskaya, G. E., Pierce, K. L., Pines, A., Ripmeester, J. A., Telkki, V.-V., and Veeman, W. S. Xenon NMR as a Probe for Microporous and Mesoporous Solids, Polymers, Liquid Crystals, Solutions, Flames, Proteins, Imaging. *L' Actualité Chimique 287* (2005), 16–34.

[6] Beaucage, G., Kammler, H. K., Mueller, R., Strobel, R., Agashe, N., Pratsinis, S. E., and Narayanan, T. Probing the Dynamics of Nanoparticle Growth in a Flame Using Synchrotron Radiation. *Nature Materials 3*, 6 (June 2004), 370–374.

[7] Bernstein, M. A., King, K. F., and Zhou, X. J. Correction Gradients: Gradient Moment Nulling. In *Handbook of MRI Pulse Sequences*. Academic Press, New York, 2004, ch. 10.4, pp. 331–349.

[8] Bernstein, M. A., King, K. F., and Zhou, X. J. *Handbook of MRI Pulse Sequences*. Academic Press, New York, 2004.

[9] Boesch, C., Gruetter, R., and Martin, E. Temporal and Spatial Analysis of Fields Generated by Eddy Currents in Superconducting Magnets: Optimization of Corrections and Quantitative Characterization of Magnet/Gradient Systems. *Magnetic Resonance in Medicine 20*, 2 (Aug. 1991), 268–284.

[10] Bouchard, L.-S., Burt, S. R., Anwar, M. S., Kovtunov, K. V., Koptyug, I. V., and Pines, A. NMR Imaging of Catalytic Hydrogenation in Microreactors with the Use of Para-Hydrogen. *Science 319*, 5862 (Jan. 2008), 442–445.

[11] Brateman, L. Chemical Shift Imaging: A Review. *American Journal of Roentgenology 146*, 5 (May 1986), 971–980.

[12] Brinkmann, D. Die Magnetischen Momente von Xe^{129} und Xe^{131}. *Helvetica Physica Acta 36*, 4 (1963), 413–414.

[13] Brinkmann, D. Verschiebung des Lokalen Magnetischen Feldes in der Kernresonanz von Edelgasen. *Helvetica Physica Acta 41*, 3 (1968), 367–384.

[14] Brown, T. R., Kincaid, B. M., and Ugurbil, K. NMR Chemical Shift Imaging in Three Dimensions. *Proceedings of the National Academy of Sciences of the United States of America 79*, 11 (June 1982), 3523–3526.

[15] Brunner, E., Haake, M., Kaiser, L., Pines, A., and Reimer, J. A. Gas Flow MRI Using Circulating Laser-Polarized ^{129}Xe. *Journal of Magnetic Resonance 138*, 1 (May 1999), 155–159.

[16] El-Banhawy, Y., Hassan, M. A., Lockwood, F. C., and Moneib, H. A. Velocity and Unburned Hydrocarbon Measurements in a Vertical Turbulent-Free Jet Diffusion Flame. *Combustion and Flame 53*, 1-3 (Nov. 1983), 145–148.

[17] Elkins, C., Markl, M., Pelc, N., and Eaton, J. 4D Magnetic Resonance Velocimetry for Mean Velocity Measurements in Complex Turbulent Flows. *Experiments in Fluids 34*, 4 (Apr. 2003), 494–503.

[18] Epstein, A. H. Millimeter-Scale, Micro-Electro-Mechanical Systems Gas Turbine Engines. *Journal of Engineering for Gas Turbines and Power 126*, 2 (2004), 205–226.

[19] Epstein, A. H., and Senturia, S. D. Microengineering: Macro Power from Micro Machinery. *Science 276*, 5316 (May 1997), 1211.

[20] Fernandez-Pello, A. C. Micropower Generation Using Combustion: Issues and Approaches. *Proceedings of the Combustion Institute 29*, 1 (2002), 883–899.

[21] Fristrom, R. M. *Flame Structure and Processes.* Oxford University Press, New York, 1995.

[22] Glover, P. M., Newling, B., Poirier, C., and Balcom, B. J. A Novel High Temperature ^{1}H NMR Imaging Probe for Combustion Studies: The Behaviour of Both a Lit and Unlit Methane Gas Jet. *Journal of Magnetic Resonance 176*, 1 (Sept. 2005), 79–86.

[23] Goodson, B. M. Nuclear Magnetic Resonance of Laser-Polarized Noble Gases in Molecules, Materials, and Organisms. *Journal of Magnetic Resonance 155*, 2 (Apr. 2002), 157–216.

[24] Graziani, D. *Portable MRI and* ^{131}*Xe Signal Amplification by Gas Extraction.* Doctor of philosophy, University of California, Berkeley, 2011.

[25] Hahn, E. Spin Echoes. *Physical Review 80*, 4 (Nov. 1950), 580–594.

[26] Halpern-Manners, N. W., Paulsen, J. L., Bajaj, V. S., and Pines, A. Remotely Detected MRI Velocimetry in Microporous Bead Packs. *The Journal of Physical Chemistry A 115*, 16 (Mar. 2011), 4023–4030.

[27] Han, S., Granwehr, J., Garcia, S., McDonnell, E. E., and Pines, A. Auxiliary Probe Design Adaptable to Existing Probes for Remote Detection NMR, MRI, and Time-of-Flight Tracing. *Journal of Magnetic Resonance 182*, 2 (Oct. 2006), 260–272.

[28] Han, S.-I., Pierce, K. L., and Pines, A. NMR Velocity Mapping of Gas Flow Around Solid Objects. *Physical Review E 74*, 1 (July 2006), 016302.

[29] Harel, E., and Pines, A. Spectrally Resolved Flow Imaging of Fluids Inside a Microfluidic Chip with Ultrahigh Time Resolution. *Journal of Magnetic Resonance 193*, 2 (Aug. 2008), 199–206.

[30] Hood, M. N., Ho, V. B., Smirniotopoulos, J. G., and Szumowski, J. Chemical Shift: The Artifact and Clinical Tool Revisited. *RadioGraphics 19*, 2 (1999), 357–371.

[31] Hore, P. J. *Nuclear Magnetic Resonance.* Oxford University Press, Oxford, 1995.

[32] Jameson, A. K., Jameson, C. J., and Gutowsky, H. S. Density Dependence of ^{129}Xe Chemical Shifts in Mixtures of Xenon and Other Gases. *The Journal of Chemical Physics 53*, 6 (1970), 2310–2321.

[33] Jameson, C. J., and Jameson, A. K. Density Dependence of ^{129}Xe N.M.R. Chemical Shifts in O_2 and NO. *Molecular Physics 20*, 5 (1971), 957–959.

[34] Jameson, C. J., Jameson, A. K., and Cohen, S. M. Temperature and Density Dependence of ^{129}Xe Chemical Shift in Xenon Gas. *The Journal of Chemical Physics 59*, 8 (1973), 4540–4546.

[35] Jameson, C. J., Jameson, A. K., Kostikin, P., and Baello, B. I. Adsorption of Xenon and CH4 Mixtures in Zeolite NaA. ^{129}Xe NMR and Grand Canonical Monte Carlo Simulations. *The Journal of Chemical Physics 112*, 1 (2000), 323–334.

[36] Kaiser, E. W., Wallington, T. J., Hurley, M. D., Platz, J., Curran, H. J., Pitz, W. J., and Westbrook, C. K. Experimental and Modeling Study of Premixed Atmospheric-Pressure Dimethyl Ether–Air Flames. *The Journal of Physical Chemistry A 104*, 35 (Sept. 2000), 8194–8206.

[37] Keeler, J. *Understanding NMR Spectroscopy*, second ed. John Wiley & Sons, 2010.

[38] Kyuma, K., Sawada, T., and Nunoshita, M. Fiber-Optic Instrument for Temperature Measurement. *IEEE Journal of Quantum Electronics 18*, 4 (Apr. 1982), 676–679.

[39] Levitt, M. H. *Spin Dynamics: Basics of Nuclear Magnetic Resonance*, second ed. John Wiley & Sons, Chichester, England, 2008.

[40] Maudsley, A. A., Hilal, S. K., Perman, W. H., and Simon, H. E. Spatially Resolved High Resolution Spectroscopy by "Four-Dimensional" NMR. *Journal of Magnetic Resonance (1969) 51*, 1 (Jan. 1983), 147–152.

[41] Meersmann, T., Anala, S., Pavlovskaya, G. E., Dieken, T. J., and Olson, M. D. Development of a New Analytical Tool: In Situ NMR and In Situ MRI of High-Temperature Reaction. *Preprints - American Chemical Society, Division of Petroleum Chemistry 49*, 3 (2004), 374–376.

[42] Mohr, P. J., Taylor, B. N., and Newell, D. B. CODATA Recommended Values of the Fundamental Physical Constants: 2006. *Journal of Physical and Chemical Reference Data 37*, 3 (2008), 1187–1284.

[43] Moulé, A. J., Spence, M. M., Han, S.-I., Seeley, J. A., Pierce, K. L., Saxena, S., and Pines, A. Amplification of Xenon NMR and MRI by Remote Detection. *Proceedings of the National Academy of Sciences of the United States of America 100*, 16 (Aug. 2003), 9122–9127.

[44] Newling, B. Gas Flow Measurements by NMR. *Progress in Nuclear Magnetic Resonance Spectroscopy 52*, 1 (Jan. 2008), 31–48.

[45] Newling, B., Gibbs, S. J., Derbyshire, J. A., Xing, D., Hall, L. D., Haycock, D. E., Frith, W. J., and Ablett, S. Comparisons of Magnetic Resonance Imaging Velocimetry With Computational Fluid Dynamics. *Journal of Fluids Engineering 119*, 1 (1997), 103–109.

[46] Nishimura, D. G. *Principles of Magnetic Resonance Imaging*. Lulu, 2010.

[47] Nishimura, D. G., Jackson, J. I., and Pauly, J. M. On the Nature and Reduction of the Displacement Artifact in Flow Images. *Magnetic Resonance in Medicine 22*, 2 (Dec. 1991), 481–492.

[48] Papadopoulos, G., Bryant, R. A., and Pitts, W. M. Flow Characterization of Flickering Methane/Air Diffusion Flames Using Particle Image Velocimetry. *Experiments in Fluids 33*, 3 (2002), 472–481.

[49] Paulsen, J., Bajaj, V. S., and Pines, A. Compressed Sensing of Remotely Detected MRI Velocimetry in Microfluidics. *Journal of Magnetic Resonance 205*, 2 (Aug. 2010), 196–201.

[50] Pavlovskaya, G. E., and Meersmann, T. Hyperpolarized ^{129}Xe NMR Spectroscopy, MRI and Dynamic NMR Microscopy for the In Situ Monitoring of Gas Dynamics in Opaque Media Including Combustion Processes. In *NMR Imaging in Chemical Engineering*, S. Stapf and S.-I. Han, Eds. Wiley-VCH Verlag GmbH & Co. KGaA, Weinheim, FRG, 2005, ch. 5.3, pp. 551–570.

[51] Pierce, K. L. *Enhancing NMR Sensitivity in Large and Small Scale Flow Systems.* Doctor of philosophy, University of California, Berkeley, 2005.

[52] Pizza, G., Frouzakis, C. E., Mantzaras, J., Tomboulides, A. G., and Boulouchosb, K. Dynamics of Premixed Hydrogen/Air Flames in Microchannels. *Combustion and Flame 152*, 3 (Feb. 2008), 433–450.

[53] Raghaven, P. Table of Nuclear Moments. *Atomic Data and Nuclear Data Tables 42*, 2 (July 1989), 189–291.

[54] Reimer, J. Chemistry: Internal Combustion. *Nature 426*, 6966 (Dec. 2003), 508–509.

[55] Rosman, K. J. R., and Taylor, P. D. P. Isotopic Compositions of the Elements 1997 (Technical Report). *Pure and Applied Chemistry 70*, 1 (1998), 217–235.

[56] Schilling, F. *MRI Thermometry Based on Hyperpolarized Xenon Biosensors.* Master thesis, Julius-Maximilians University Würzburg, 2009.

[57] Schilling, F., Schröder, L., Palaniappan, K. K., Zapf, S., Wemmer, D. E., and Pines, A. MRI Thermometry Based on Encapsulated Hyperpolarized Xenon. *ChemPhysChem 11*, 16 (Nov. 2010), 3529–3533.

[58] Schreiber, E., Ed. *VnmrJ Imaging, User's Guide: Varian MR Systems With VnmrJ 2.2C Software.* Varian, Inc., Palo Alto, CA, 2007.

[59] Schröder, L., Chavez, L., Meldrum, T., Smith, M., Lowery, T. J., Wemmer, D. E., and Pines, A. Temperature-Controlled Molecular Depolarization Gates in Nuclear Magnetic Resonance. *Angewandte Chemie (International ed. in English) 47*, 23 (Jan. 2008), 4316–4320.

[60] Simon, J. H., and Szumowski, J. Proton (Fat/Water) Chemical Shift Imaging in Medical Magnetic Resonance Imaging: Current Status. *Investigative Radiology 27*, 10 (Oct. 1992), 865–874.

[61] Stone, N. J. Table of Nuclear Magnetic Dipole and Electric Quadrupole Moments. *Atomic Data and Nuclear Data Tables 90*, 1 (May 2005), 75–176.

[62] Trease, D. R. *Advances in NMR Methodology.* Doctor of philosophy, University of California, Berkeley, 2010.

[63] Tse, S. D., Anthenien, R. A., Fernandez-Pello, A. C., and Miyasaka, K. An Application of Ultrasonic Tomographic Imaging to Study Smoldering Combustion. *Combustion and Flame 116*, 1-2 (Jan. 1999), 120–135.

[64] Turner, R. Gradient Coil Design: A Review of Methods. *Magnetic Resonance Imaging 11*, 7 (1993), 903–920.

[65] Walker, T. G., and Happer, W. Spin-Exchange Optical Pumping of Noble-Gas Nuclei. *Reviews of Modern Physics 69*, 2 (Apr. 1997), 629–642.

[66] Whiting, N., Nikolaou, P., Eschmann, N. A., Barlow, M. J., Lammert, R., Ungar, J., Hu, W., Vaissie, L., and Goodson, B. M. Using Frequency-Narrowed, Tunable Laser Diode Arrays with Integrated Volume Holographic Gratings for Spin-Exchange Optical Pumping at High Resonant Fluxes and Xenon Densities. *Applied Physics B 106*, 4 (Mar. 2012), 775–788.

[67] Whiting, N., Nikolaou, P., Eschmann, N. A., Goodson, B. M., and Barlow, M. J. Interdependence of In-Cell Xenon Density and Temperature During Rb/^{129}Xe Spin-Exchange Optical Pumping using VHG-Narrowed Laser Diode Arrays. *Journal of Magnetic Resonance 208*, 2 (Feb. 2011), 298–304.

[68] Xu, S., Crawford, C. W., Rochester, S., Yashchuk, V., Budker, D., and Pines, A. Submillimeter-Resolution Magnetic Resonance Imaging at the Earth's Magnetic Field with an Atomic Magnetometer. *Physical Review A 78*, 1 (July 2008), 013404.

[69] Xu, S., Yashchuk, V. V., Donaldson, M. H., Rochester, S. M., Budker, D., and Pines, A. Magnetic Resonance Imaging with an Optical Atomic Magnetometer. *Proceedings of the National Academy of Sciences of the United States of America 103*, 34 (Aug. 2006), 12668–12671.

[70] Yoon, S. S., Anh, D. H., and Chung, S. H. Synergistic Effect of Mixing Dimethyl Ether with Methane, Ethane, Propane, and Ethylene Fuels on Polycyclic Aromatic Hydrocarbon and Soot Formation. *Combustion and Flame 154*, 3 (Aug. 2008), 368–377.

[71] Zhao, Z., Kazakov, A., and Dryer, F. Measurements of Dimethyl Ether/Air Mixture Burning Velocities by Using Particle Image Velocimetry. *Combustion and Flame 139*, 1-2 (Oct. 2004), 52–60.

[72] Zhou, X., Luo, J., Sun, X., Zeng, X., Zhan, M., Ding, S., and Liu, M. Experiment and Dynamic Simulations of Radiation Damping of Laser-Polarized Liquid ^{129}Xe at Low Magnetic Field in a Flow System. *Applied Magnetic Resonance 26*, 3 (Sept. 2004), 327–337.

[73] Zhou, X., Sun, X.-P., Luo, J., Zeng, X.-Z., Liu, M.-L., and Zhan, M.-S. Production of Hyperpolarized ^{129}Xe Gas Without Nitrogen by Optical Pumping at ^{133}Cs D_2 Line in Flow System. *Chinese Physics Letters 21*, 8 (Aug. 2004), 1501–1503.

Appendix A

Instrumentation

A.1 Xenon Polarizer

There are two xenon hyperpolarizers in use in our lab: a commercial system manufactured by Magnetic Imaging Technologies, Inc. (now part of General Electric Healthcare) and a system fabricated in house in between 2007 and 2008. Postdoctoral researcher Xin Zhou was instrumental in the fabrication effort, and had previous experience with xenon hyperpolarizers [72, 73].

The homebuilt xenon polarizer was used to generate the hyperpolarized xenon mixture used for the combustion imaging studies. A mass flow controller (MFC; Aalborg Part No. DFC26S-VADN5-C5A,3XX-07-XS) delivers 0.3 standard liters per minute of the xenon mixture (2% natural abundance xenon, 10% nitrogen, balance helium) to the polarization cell. The pumping cell is heated to 130 °C, to increase the vapor pressure of rubidium. The previous xenon combustion study [1] used a different xenon mixture (5% xenon, 5% nitrogen, balance helium), and operated at 700 kPa (101.5 psi) and 393 K (120 °C).

The polarizer flow diagram is detailed in Figure A.1. The drop to atmospheric pressure, from ≈ 70 psig in the pumping cell, occurs across a needle valve prior to the gas reaching the magnet (after the "OUT" shown in the diagram. This is in contrast to all previous and current work in the Pines Lab, where spectroscopy and imaging of the hyperpolarized xenon is performed at higher pressures ($50 - 70$ psig) [24, 57]. Thus, the importance of the needle valve cannot be overlooked, as described in Section 3.3.2.

A.1.1 Testing Level of Polarization

The output of the xenon polarizer should be tested regularly to determine the current level of polarization, by comparison to a thermal (non-hyperpolarized) standard. Measurement of polarization levels is necessary for reporting of experimental sensitivity enhancements. Regular polarization checks can also help to determine whether the cell needs to be changed due to rubidium oxidation or if other problems may be present leading to a drop in signal.

At thermal equilibrium, the difference in population in a thermal standard is given by $\frac{1}{2}\mathbb{B}$,

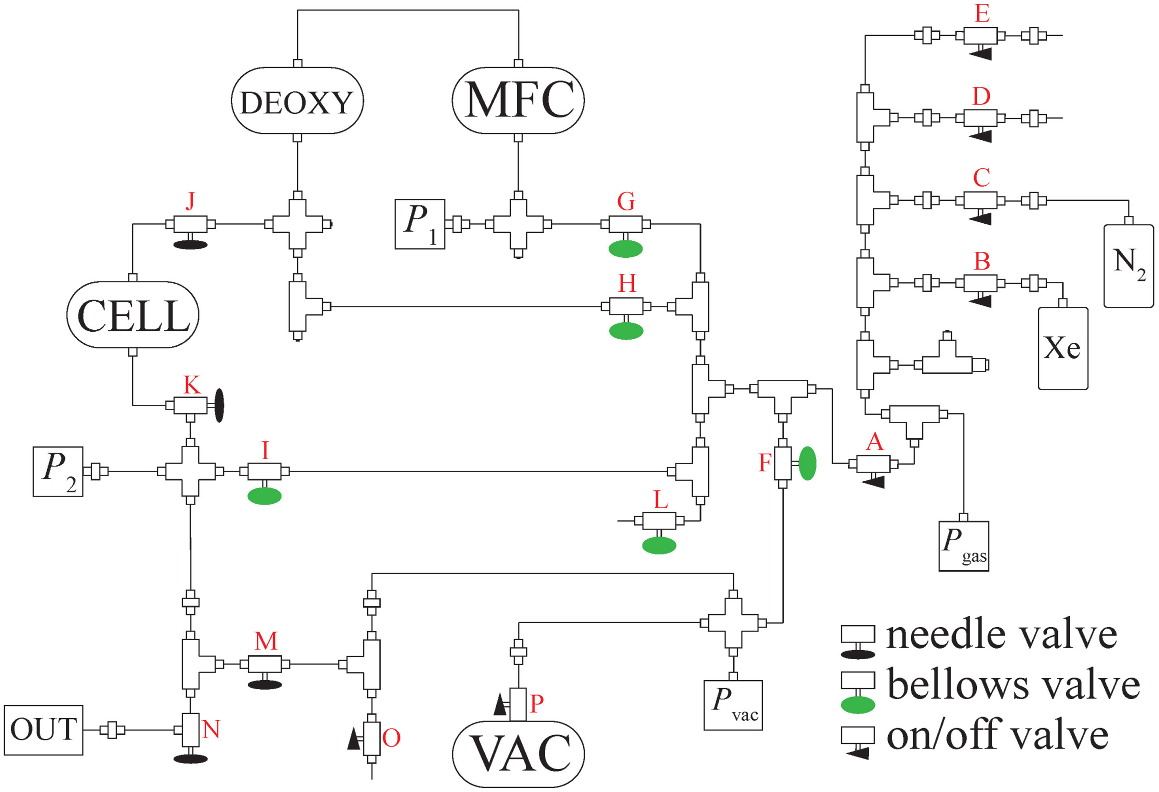

Figure A.1: A flow diagram of the homebuilt polarizer. The valves are lettered from A to M, and the other parts are as follows: CELL (Rb pumping cell), DEOXY (oxygen trap), MFC (mass flow controller), P_1 (input digital pressure gauge), P_2 (output digital pressure gauge), P_{gas} (gas backing pressure gauge), P_{vac} (vacuum pressure gauge), VAC (vaccuum pump).

where the Boltzmann factor $\mathbb{B}$ is defined by Equation A.1 (from Levitt [39] Equation 11.16).

$$\text{polarization}_{\text{thermal}} = \frac{1}{2}\,\mathbb{B} = \frac{\hbar\,|\gamma|\,B^0}{2\,k_{\text{B}}\,T} \tag{A.1}$$

This equation can be simplified for any combination of magnetic field (B^0, in tesla) and temperature (T, in kelvin) for protons (Equation A.2) and ^{129}Xe (Equation A.3).

$$\text{polarization}_{\text{thermal}(^{1}\text{H})} = (1.0217 \times 10^{-3}\ \text{K T}^{-1})\,\frac{B^0}{T} \tag{A.2}$$

$$\text{polarization}_{\text{thermal}(^{129}\text{Xe})} = (0.2826 \times 10^{-3}\ \text{K T}^{-1})\,\frac{B^0}{T} \tag{A.3}$$

At 9.395 T (400 MHz ^{1}H, 110.6 MHz ^{129}Xe), the polarization for a thermal standard of ^{129}Xe is 9 ppm or 0.0009% at room and magnet bore temperatures. The thermal standard typically used is a mixture of 50 psig (64.696 psia) natural abundance xenon with 10 psig oxygen added to reduce T_1 so that signal averaging is possible in a reasonable time. By contrast, a typical level of output polarization for the homebuilt xenon polarizer approaches 10%, a greater than 10,000 times increase.

The hyperpolarization improvement can be calculated using Equation A.4,

$$\frac{\text{polarization}_{\text{hyper}}}{\text{polarization}_{\text{thermal}}} = \frac{N_{\text{thermal}}}{N_{\text{hyper}}} \frac{\sqrt{\mathfrak{N}_{\text{thermal}}}}{\sqrt{\mathfrak{N}_{\text{hyper}}}} \frac{\text{SNR}_{\text{hyper}}}{\text{SNR}_{\text{thermal}}} \tag{A.4}$$

where $\mathfrak{N}$ is the number of transients acquired, SNR is the signal-to-noise ratio, and the number of ^{129}Xe atoms (N) in each sample can be determined using Equation A.5.

$$N_{^{129}\text{Xe}} = (\text{NA}_{^{129}\text{Xe}})\,(\text{mole }\%)\,\frac{P\,V}{k_{\text{B}}\,T} \tag{A.5}$$

Equation A.4 can be simplified, as both the thermal and hyperpolarized samples are at natural isotopic abundance, and the volume and temperature are assumed to be equal. The resulting Equation A.6 allows calculation of the polarization enhancement.

$$\frac{\text{polarization}_{\text{hyper}}}{\text{polarization}_{\text{thermal}}} = \frac{P_{\text{thermal}}}{P_{\text{hyper}}} \frac{(\text{mole }\%)_{\text{thermal}}}{(\text{mole }\%)_{\text{hyper}}} \frac{\sqrt{\mathfrak{N}_{\text{thermal}}}}{\sqrt{\mathfrak{N}_{\text{hyper}}}} \frac{\text{SNR}_{\text{hyper}}}{\text{SNR}_{\text{thermal}}} \tag{A.6}$$

Using a 2 % xenon hyperpolarization mixture and the thermal standard described above (72.37 mole %) at 9.395 T (bore temperature 16 °C):

$$\text{polarization}_{\text{hyper}} = \frac{0.0297\text{ psia}}{P_{\text{hyper}}} \frac{\sqrt{\mathfrak{N}_{\text{thermal}}}}{\sqrt{\mathfrak{N}_{\text{hyper}}}} \frac{\text{SNR}_{\text{hyper}}}{\text{SNR}_{\text{thermal}}} \tag{A.7}$$

To measure $\text{SNR}_{\text{hyper}}$, the output of the xenon polarizer is flowed into the tube from the "bubbling" setup. The output of the bubbling tube runs through a needle valve, so the tube is at the same pressure as the polarizer, which can be read from the readout on the computer. The **spuls** pulse sequence is used after pulse width calibration and the **getsn** command is used to measure the SNR. The number of transients, $\mathfrak{N}$, is set using **nt**.

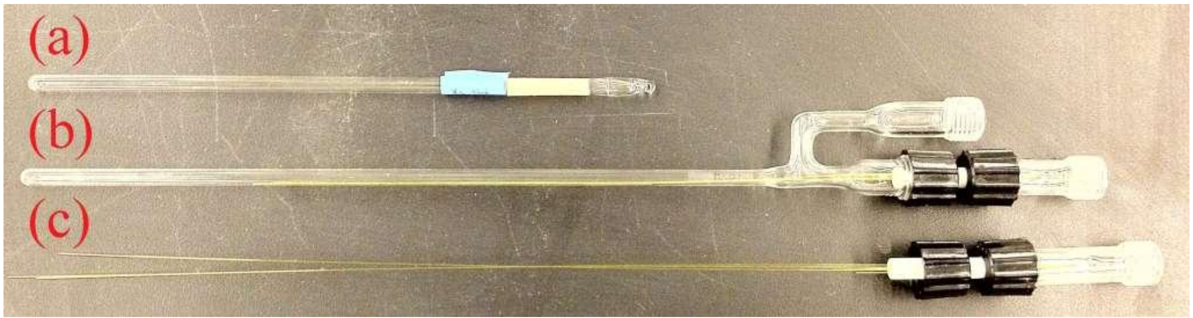

Figure A.2: (a) Thermal ^{129}Xe standard. (b) Bubbling tube used to keep HP xenon at polarizer output pressure. (c) A picture of the connector, detailing the fused silica tubes used to deliver the HP xenon into the base of the tube.

A.1.2 Rubidium Oxidation

The surface layer of the liquid rubidium in the pumping cell oxidizes over time, which leads to a loss in polarization enhancement. This is caused by a decrease in pumping efficiency due to the lower vapor pressure, as well as the depolarization of xenon at this surface. Cleaning out the cell and replacing the oxidized rubidium with 1 g of fresh rubidium will improve polarization enhancement (Figure A.3). The use, and proper care, of an oxygen trap is effective at prolonging the life of the cell. This removes trace oxygen from the xenon mixture prior to it entering the cell.

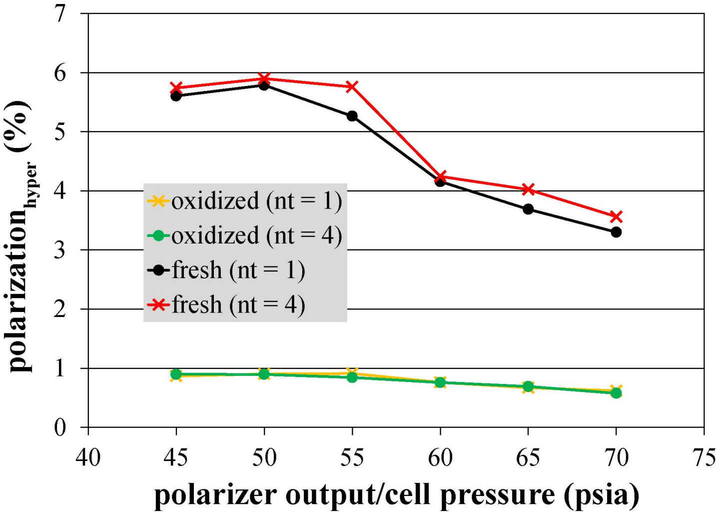

Figure A.3: Comparison of polarization levels at various pressures for an old, oxidized rubidium cell and a fresh cell. Polarization is improved by more than five times. Polarization is generally higher at lower pressures.

Appendix B

Calculations

B.1 Calculation of Xenon-129 Gyromagnetic Ratio

Most published values of the magnetic moment [61] cite a 1968 paper by Brinkmann [13], which refers back to the author's previous 1963 paper where it was first reported [12]. Brinkmann measured the xenon-129 to deuteron frequency ratio, extrapolated to zero density to be 1.80192(2). This value is not corrected for diamagnetism. By applying the diamagnetic correction for xenon-129 ($Z = 54$) and deuterons ($Z = 1$) [53],

$$\frac{\nu_{^{129}\mathrm{Xe}}}{\nu_\mathrm{d}} = \frac{1-\sigma'_\mathrm{d}}{1-\sigma'_{^{129}\mathrm{Xe}}} \cdot \frac{\nu'_{^{129}\mathrm{Xe}}}{\nu'_\mathrm{d}} = 1.81465(2), \tag{B.1}$$

the corrected frequency ratio results.

The xenon-129 magnetic moment is obtained using the most recent recommended value of the deuteron magnetic moment [42]:

$$\frac{\mu_{^{129}\mathrm{Xe}}}{\mu_\mathrm{N}} = \frac{I_{^{129}\mathrm{Xe}}}{I_\mathrm{d}} \cdot \frac{\mu_\mathrm{d}}{\mu_\mathrm{N}} \cdot \frac{\nu_{^{129}\mathrm{Xe}}}{\nu_\mathrm{d}} = -0.777976(9). \tag{B.2}$$

This is the value given by Stone [61]. To obtain the corrected gyromagnetic ratio (over 2π), the most recent recommended value of the nuclear magneton is used:

$$\frac{\gamma_{^{129}\mathrm{Xe}}}{2\pi} = \frac{1}{I_{^{129}\mathrm{Xe}}} \cdot \frac{\mu_\mathrm{N}}{h} \cdot \frac{\mu_{^{129}\mathrm{Xe}}}{\mu_\mathrm{N}} = -11.8604(1)\ \mathrm{MHz\ T^{-1}}. \tag{B.3}$$

This means that the corrected gyromagnetic ratio is equal to $-74.5211(8)$ rad MHz T^{-1}.

The more useful values, which are not corrected for diamagnetism are:

$$\frac{\mu'_{^{129}\mathrm{Xe}}}{\mu_\mathrm{N}} = -0.772498(9), \qquad \gamma'_{^{129}\mathrm{Xe}} = -73.9963(8)\ \mathrm{rad\ MHz\ T^{-1}}, \tag{B.4}$$

$$\frac{\gamma'_{^{129}\mathrm{Xe}}}{2\pi} = -11.7769(1)\ \mathrm{MHz\ T^{-1}}. \tag{B.5}$$

B.2 Gradient Moment Nulling

Calculations of gradient nulling waveforms with three equal-length lobes were made for each of three lobes shapes: rectangular, triangular, and trapezoidal. Both the triangles and trapezoids are isosceles. The ratios necessary for encoding position, velocity, or acceleration, while nulling the other two moments, are presented here. The accrued magnetic moments, which can be used to determine the phase, as well as the fields of view (FOV) and aliasing velocity parameters (VENC), are also presented.

The peak strengths of the gradient lobes are designated G_1, G_2, and G_3 and the time of each individual lobe is T. The length of the total waveform is $3T$. N_{pe} is the number of phase-encodes. Please note that in the velocity- and acceleration-encoding waveforms, the second gradient lobe has a higher magnitude than the first lobe, which must be taken into account when determining whether triangular or trapezoidal waveforms are appropriate.

B.2.1 Rectangular Waveforms

For encoding position with velocity and acceleration compensation:

$$G_1 : G_2 : G_3 = \frac{11}{11} : -\frac{7}{11} : \frac{2}{11}, \tag{B.6}$$

$$m_0 = \frac{6}{11}\, G_1\, T, \tag{B.7}$$

$$\mathrm{FOV} = \frac{11}{12}\, \frac{N_{\mathrm{pe}} - 1}{\frac{\gamma}{2\pi}\, G_1\, T}. \tag{B.8}$$

For encoding velocity with position and acceleration compensation:

$$G_1 : G_2 : G_3 = \frac{2}{2} : -\frac{3}{2} : \frac{1}{2}, \tag{B.9}$$

$$m_1 = -\frac{1}{2}\, G_1\, T^2, \tag{B.10}$$

$$\mathrm{VENC} = \frac{1}{2\, \frac{\gamma}{2\pi}\, |G_1|\, T^2}. \tag{B.11}$$

For encoding acceleration with position and velocity compensation:

$$G_1 : G_2 : G_3 = 1 : -2 : 1, \tag{B.12}$$

$$m_2 = 2\, G_1\, T^3. \tag{B.13}$$

B.2.2 Triangular Waveforms

For encoding position with velocity and acceleration compensation:

$$G_1 : G_2 : G_3 = \frac{89}{89} : -\frac{58}{89} : \frac{17}{89}, \tag{B.14}$$

$$m_0 = \frac{24}{89}\, G_1\, T, \tag{B.15}$$

$$\text{FOV} = \frac{89}{48}\, \frac{N_{\text{pe}} - 1}{\frac{\gamma}{2\pi}\, G_1\, T}. \tag{B.16}$$

For encoding velocity with position and acceleration compensation:

$$G_1 : G_2 : G_3 = \frac{2}{2} : -\frac{3}{2} : \frac{1}{2}, \tag{B.17}$$

$$m_1 = -\frac{1}{4}\, G_1\, T^2, \tag{B.18}$$

$$\text{VENC} = \frac{1}{\frac{\gamma}{2\pi}\, |G_1|\, T^2}. \tag{B.19}$$

For encoding acceleration with position and velocity compensation:

$$G_1 : G_2 : G_3 = 1 : -2 : 1, \tag{B.20}$$

$$m_2 = G_1\, T^3. \tag{B.21}$$

B.2.3 Trapezoidal Waveforms

For trapezoidal waveforms, the ramp time (T_{ramp}) and total lobe time (T) are necessary for the calculations. The two are related by:

$$T = 2\, T_{\text{ramp}} + T_{\text{plateau}}, \tag{B.22}$$

where T_{plateau} is the length of the trapezoid plateau. The rectangular equations result as T_{ramp} approaches zero, while the triangular equations result as T_{ramp} approaches $\frac{1}{2}T$.

For encoding position with velocity and acceleration compensation (see Figure B.1):

$$G_1 : G_2 : G_3 = 1 : -2 \left[\frac{7 + (\frac{T_{\text{ramp}}}{T}) - (\frac{T_{\text{ramp}}}{T})^2}{22 + (\frac{T_{\text{ramp}}}{T}) - (\frac{T_{\text{ramp}}}{T})^2} \right] : \left[\frac{4 + (\frac{T_{\text{ramp}}}{T}) - (\frac{T_{\text{ramp}}}{T})^2}{22 + (\frac{T_{\text{ramp}}}{T}) - (\frac{T_{\text{ramp}}}{T})^2} \right], \tag{B.23}$$

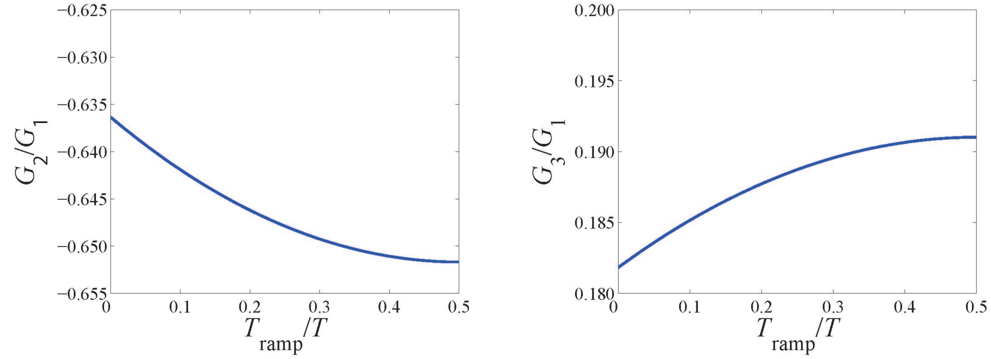

(a) (b)

Figure B.1: Ratios of the (a) second and (b) third isosceles trapezoidal gradient lobes for position-encoding, with velocity and acceleration compensation. The ratios at $\frac{T_{\text{ramp}}}{T} = 0$ are equal to the rectangular ratios, while the ratios at $\frac{T_{\text{ramp}}}{T} = \frac{1}{2}$ are equal to the triangular ratios.

$$m_0 = \left[\frac{12\,(1 - \frac{T_{\text{ramp}}}{T})}{22 + (\frac{T_{\text{ramp}}}{T}) - (\frac{T_{\text{ramp}}}{T})^2} \right] G_1\, T, \tag{B.24}$$

$$\text{FOV} = \left[\frac{22 + (\frac{T_{\text{ramp}}}{T}) - (\frac{T_{\text{ramp}}}{T})^2}{24} \right] \frac{N_{\text{pe}} - 1}{\frac{\gamma}{2\pi}\, G_1\, (T - T_{\text{ramp}})}. \tag{B.25}$$

For encoding velocity with position and acceleration compensation:

$$G_1 : G_2 : G_3 = \frac{2}{2} : -\frac{3}{2} : \frac{1}{2}, \tag{B.26}$$

$$m_1 = -\left[\frac{1 - (\frac{T_{\text{ramp}}}{T})}{2} \right] G_1\, T^2, \tag{B.27}$$

$$\text{VENC} = \frac{1}{2\,[1 - (\frac{T_{\text{ramp}}}{T})]\, \frac{\gamma}{2\pi}\, |G_1|\, T^2}. \tag{B.28}$$

For encoding acceleration with position and velocity compensation:

$$G_1 : G_2 : G_3 = 1 : -2 : 1, \tag{B.29}$$

$$m_2 = 2 \left[1 - \left(\frac{T_{\text{ramp}}}{T} \right) \right] G_1\, T^3. \tag{B.30}$$

B.3 Thermocouple Data Manipulation

B.3.1 Cartesian-Collected Data

The thermocouple data collected in a Cartesian coordinate sampling pattern (see Section 3.3.7) was manipulated in MATLAB to produce Figure 4.13. The $9 \times 9 \times 5$ $(x \times y \times z)$ data was first two-dimensionally interpolated within each of the z-slices to $33 \times 33 \times 5$. Three-dimensional interpolation was not employed because the points there were much closer together within the slices (1.6 mm separation) than they were between them (6.4 mm separation). One-dimensional interpolation along z was then performed between the equivalent points in each of the interpolated slices to arrive at a $33 \times 33 \times 65$ array, the same size as the zero-filled magnetic resonance imaging data set (0.4 mm resolution).

B.3.2 Radial-Collected Data

The thermocouple data collected in a radial sampling pattern (see Section 3.3.7) was manipulated in MATLAB to produce Figure 4.14. Simple two- or three-dimensional interpolation would not work for this data set due to the non-uniform positioning of the points within x- and y-space. The r/θ positions were first converted into x/y positions. In order to get to a final array size of $33 \times 33 \times 65$ $(x \times y \times z)$ with 0.4 mm resolution, the final temperatures are determined by averaging the nearest five data points, weighted by the normalized inverse of their Euclidean distance from the final point. The points outside of the radial field of view are set to **NaN**.

Appendix C

Reference Code

C.1 VnmrJ Pulse Sequence

The C-code for the VnmrJ pulse sequence **csi_vel_ac** is presented here. Only the full steps for the first gradient lobe are shown. In the other lobes the corresponding middle portion is replaced by "...".

```
/* Chemical Shift Imaging (CSI) and Velocity Imaging pulse sequences with
   velocity and acceleration compensated phase-encoding using
   gradient moment nulling and triangular or trapezoidal gradient pulses.
   - J. Peter Mustonen 06/14/2010
*/

/* csi_vel_ac */

#include <standard.h>

static int phasecycle[4] = {0, 1, 2, 3};
static int reccycle[4] = {0, 2, 0, 2};

pulsesequence()
{  double d1, enct, dtotal, dv, dvac, dac, decho1, decho2, pw;
   double gvt, gvx, gvy, gvz;
   double gact, gacx, gacy, gacz;
   double gvrt, gacrt, p, gvel2, gvel3, gac2, gac3;
   d1 = getval("d1"); // recycle delay
   enct = getval("enct"); // total time between 90 and 180 (encoding)
   decho1 = getval("decho1"); // post-180, pre-acquire delay
   decho2 = getval("decho2"); // post-acquire delay
   pw = getval("pw"); // 90-degree pulse-width
   gvt = getval("gvt"); // velocity gradient time (total)
   gvx = getval("gvx"); // velocity gradient amplitude x (< 21844)
   gvy = getval("gvy"); // velocity gradient amplitude y (< 21844)
   gvz = getval("gvz"); // velocity gradient amplitude z (< 21844)
```

```
   gact = getval("gact"); // ac gradient time (total)
   gacx = getval("gacx"); // ac gradient amplitude x (< 32767)
   gacy = getval("gacy"); // ac gradient amplitude y (< 32767)
   gacz = getval("gacz"); // ac gradient amplitude z (< 32767)

   settable(t1, 4, phasecycle);
   settable(t2, 4, reccycle);

/* set delay times for total encoding of genct (sec) */

   if (gvt == 0 && gact == 0) {
     dv = enct / 3;
     dvac = enct / 3;
     dac = enct / 3; }
   if (gvt == 0 && gact > 0) {
     dv = (enct - 3 * gact) / 4;
     dvac = dv;
     dac = 2 * dv; }
   if (gvt > 0 && gact == 0) {
     dv = (enct - 2 * gvt) / 2; // should be 3 * gvt
     dvac = dv / 2;
     dac = dv / 2; }

/* if vel gradient on, determine spacing */

   if (gvt > 0 && gact > 0) {
     dtotal = enct - 2 * gvt - 3 * gact; // should be 3 * gvt
     dv = 1 * dtotal / 3;
     dvac = 1 * dtotal / 3;
     dac = 1 * dtotal / 3; }

/* set velocity ramp step time (4e-6 <= gvrt < 8e-6) */

   if (gvt <= 200e-6) {
     gvrt = gvt / floor(gvt / 40e-6) / 10; }
   if (gvt > 200e-6) {
     gvrt = 4e-6; }

/* set ac ramp step time (4e-6 <= gacrt < 8e-6) and determine plateau ratio */

   if (gact <= 200e-6) {
     gacrt = gact / floor(gact / 40e-6) / 10;
     p = 0; } // should be p = 0.5;
   if (gact > 200e-6) {
     gacrt = 4e-6;
     p = 100e-6 / gact; }

/* check for errors */

   if (dv < 0) {
     abort_message("encoding time exceeeds 4 ms"); }
```

```
    if (1.5 * abs(gvx) / gvt > 32767 / 200e-6 && gvt > 0) {
      abort_message("gvx ramp too steep"); }
    if (1.5 * abs(gvy) / gvt > 32767 / 200e-6 && gvt > 0) {
      abort_message("gvy ramp too steep"); }
    if (1.5 * abs(gvz) / gvt > 32767 / 200e-6 && gvt > 0) {
      abort_message("gvz ramp too steep"); }
    if (abs(gacx) / gact > 32767 / 200e-6 && gact > 0) {
      abort_message("gacx ramp too steep"); }
    if (abs(gacy) / gact > 32767 / 200e-6 && gact >0) {
      abort_message("gacy ramp too steep"); }
    if (abs(gacz) / gact > 32767 / 200e-6 && gact >0) {
      abort_message("gacz ramp too steep"); }
    if (abs(gvx) > 0 && abs(gvy) > 0) {
      abort_message("two velocity gradients on: x & y"); }
    if (abs(gvx) > 0 && abs(gvz) > 0) {
      abort_message("two velocity gradients on: x & z"); }
    if (abs(gvy) > 0 && abs(gvz) > 0) {
      abort_message("two velocity gradients on: y & z"); }

/* set vel gradient ratios */

    gvel2 = -1.5;
    gvel3 = 0.5;

/* set ac gradient ratios */

    gac2 = -2 * (7 + p - p * p) / (22 + p - p * p);
    gac3 = (4 + p - p * p) / (22 + p - p * p);

/* adjust gradient amplitudes for lobes shorter than 200e-6 */

    if (gvt < 80e-6) {
      gvx = gvx / 0.20;
      gvy = gvy / 0.20;
      gvz = gvz / 0.20; }
    if (gvt >= 80e-6 && gvt < 120e-6) {
      gvx = gvx / 0.40;
      gvy = gvy / 0.40;
      gvz = gvz / 0.40; }
    if (gvt >= 120e-6 && gvt < 160e-6) {
      gvx = gvx / 0.60;
      gvy = gvy / 0.60;
      gvz = gvz / 0.60; }
    if (gvt >= 160e-6 && gvt < 200e-6) {
      gvx = gvx / 0.80;
      gvy = gvy / 0.80;
      gvz = gvz / 0.80; }
    if (gact < 80e-6) {
      gacx = gacx / 0.20;
      gacy = gacy / 0.20;
      gacz = gacz / 0.20; }
```

```
   if (gact >= 80e-6 && gact < 120e-6) {
     gacx = gacx / 0.40;
     gacy = gacy / 0.40;
     gacz = gacz / 0.40; }
   if (gact >= 120e-6 && gact < 160e-6) {
     gacx = gacx / 0.60;
     gacy = gacy / 0.60;
     gacz = gacz / 0.60; }
   if (gact >= 160e-6 && gact < 200e-6) {
     gacx = gacx / 0.80;
     gacy = gacy / 0.80;
     gacz = gacz / 0.80; }

/* equilibrium period */

   status(A);
   delay(d1);

/* encoding */

   status(B);
   obspower(tpwr);
   obsoffset(tof);
   rgpulse(pw, zero, rof1, rof2);

   delay(dv);

/* velocity-encoding lobe 1 of 3 */

   if (gvt >= 40e-6) {
     rgradient('x', 0.04 * gvx);
     rgradient('y', 0.04 * gvy);
     rgradient('z', 0.04 * gvz);
     delay(gvrt);
     rgradient('x', 0.08 * gvx);
     rgradient('y', 0.08 * gvy);
     rgradient('z', 0.08 * gvz);
     delay(gvrt);
     rgradient('x', 0.12 * gvx);
     rgradient('y', 0.12 * gvy);
     rgradient('z', 0.12 * gvz);
     delay(gvrt);
     rgradient('x', 0.16 * gvx);
     rgradient('y', 0.16 * gvy);
     rgradient('z', 0.16 * gvz);
     delay(gvrt);
     rgradient('x', 0.20 * gvx);
     rgradient('y', 0.20 * gvy);
     rgradient('z', 0.20 * gvz);
     delay(gvrt);
     if (gvt >= 80e-6) {
```

```
      rgradient('x', 0.24 * gvx);
      rgradient('y', 0.24 * gvy);
      rgradient('z', 0.24 * gvz);
      delay(gvrt);
      rgradient('x', 0.28 * gvx);
      rgradient('y', 0.28 * gvy);
      rgradient('z', 0.28 * gvz);
      delay(gvrt);
      rgradient('x', 0.32 * gvx);
      rgradient('y', 0.32 * gvy);
      rgradient('z', 0.32 * gvz);
      delay(gvrt);
      rgradient('x', 0.36 * gvx);
      rgradient('y', 0.36 * gvy);
      rgradient('z', 0.36 * gvz);
      delay(gvrt);
      rgradient('x', 0.40 * gvx);
      rgradient('y', 0.40 * gvy);
      rgradient('z', 0.40 * gvz);
      delay(gvrt);
      if (gvt >= 120e-6) {
        rgradient('x', 0.44 * gvx);
        rgradient('y', 0.44 * gvy);
        rgradient('z', 0.44 * gvz);
        delay(gvrt);
        rgradient('x', 0.48 * gvx);
        rgradient('y', 0.48 * gvy);
        rgradient('z', 0.48 * gvz);
        delay(gvrt);
        rgradient('x', 0.52 * gvx);
        rgradient('y', 0.52 * gvy);
        rgradient('z', 0.52 * gvz);
        delay(gvrt);
        rgradient('x', 0.56 * gvx);
        rgradient('y', 0.56 * gvy);
        rgradient('z', 0.56 * gvz);
        delay(gvrt);
        rgradient('x', 0.60 * gvx);
        rgradient('y', 0.60 * gvy);
        rgradient('z', 0.60 * gvz);
        delay(gvrt);
        if (gvt >= 160e-6) {
          rgradient('x', 0.64 * gvx);
          rgradient('y', 0.64 * gvy);
          rgradient('z', 0.64 * gvz);
          delay(gvrt);
          rgradient('x', 0.68 * gvx);
          rgradient('y', 0.68 * gvy);
          rgradient('z', 0.68 * gvz);
          delay(gvrt);
          rgradient('x', 0.72 * gvx);
```

```
      rgradient('y', 0.72 * gvy);
      rgradient('z', 0.72 * gvz);
      delay(gvrt);
      rgradient('x', 0.76 * gvx);
      rgradient('y', 0.76 * gvy);
      rgradient('z', 0.76 * gvz);
      delay(gvrt);
      rgradient('x', 0.80  *  gvx);
      rgradient('y', 0.80 * gvy);
      rgradient('z', 0.80 * gvz);
      delay(gvrt);
      if (gvt >= 200e-6) {
        rgradient('x', 0.84 * gvx);
        rgradient('y', 0.84 * gvy);
        rgradient('z', 0.84 * gvz);
        delay(gvrt);
        rgradient('x', 0.88 * gvx);
        rgradient('y', 0.88 * gvy);
        rgradient('z', 0.88 * gvz);
        delay(gvrt);
        rgradient('x', 0.92 * gvx);
        rgradient('y', 0.92 * gvy);
        rgradient('z', 0.92 * gvz);
        delay(gvrt);
        rgradient('x', 0.96 * gvx);
        rgradient('y', 0.96 * gvy);
        rgradient('z', 0.96 * gvz);
        delay(gvrt);
        rgradient('x', 1.00 * gvx);
        rgradient('y', 1.00 * gvy);
        rgradient('z', 1.00 * gvz);
        delay(gvrt);
    if (gvt > 200e-6) {
          rgradient('x', 1.00 * gvx);
          rgradient('y', 1.00 * gvy);
          rgradient('z', 1.00 * gvz);
          delay(gvt - 200e-6); }
        rgradient('x', 0.96 * gvx);
        rgradient('y', 0.96 * gvy);
        rgradient('z', 0.96 * gvz);
        delay(gvrt);
        rgradient('x', 0.92 * gvx);
        rgradient('y', 0.92 * gvy);
        rgradient('z', 0.92 * gvz);
        delay(gvrt);
        rgradient('x', 0.88 * gvx);
        rgradient('y', 0.88 * gvy);
        rgradient('z', 0.88 * gvz);
        delay(gvrt);
        rgradient('x', 0.84 * gvx);
        rgradient('y', 0.84 * gvy);
```

```
      rgradient('z', 0.84 * gvz);
      delay(gvrt);
      rgradient('x', 0.80 * gvx);
      rgradient('y', 0.80 * gvy);
      rgradient('z', 0.80 * gvz);
      delay(gvrt); }
     rgradient('x', 0.76 * gvx);
     rgradient('y', 0.76 * gvy);
     rgradient('z', 0.76 * gvz);
     delay(gvrt);
     rgradient('x', 0.72 * gvx);
     rgradient('y', 0.72 * gvy);
     rgradient('z', 0.72 * gvz);
     delay(gvrt);
     rgradient('x', 0.68 * gvx);
     rgradient('y', 0.68 * gvy);
     rgradient('z', 0.68 * gvz);
     delay(gvrt);
     rgradient('x', 0.64 * gvx);
     rgradient('y', 0.64 * gvy);
     rgradient('z', 0.64 * gvz);
     delay(gvrt);
     rgradient('x', 0.60 * gvx);
     rgradient('y', 0.60 * gvy);
     rgradient('z', 0.60 * gvz);
     delay(gvrt); }
    rgradient('x', 0.56 * gvx);
    rgradient('y', 0.56 * gvy);
    rgradient('z', 0.56 * gvz);
    delay(gvrt);
    rgradient('x', 0.52 * gvx);
    rgradient('y', 0.52 * gvy);
    rgradient('z', 0.52 * gvz);
    delay(gvrt);
    rgradient('x', 0.48 * gvx);
    rgradient('y', 0.48 * gvy);
    rgradient('z', 0.48 * gvz);
    delay(gvrt);
    rgradient('x', 0.44 * gvx);
    rgradient('y', 0.44 * gvy);
    rgradient('z', 0.44 * gvz);
    delay(gvrt);
    rgradient('x', 0.40 * gvx);
    rgradient('y', 0.40 * gvy);
    rgradient('z', 0.40 * gvz);
    delay(gvrt); }
   rgradient('x', 0.36 * gvx);
   rgradient('y', 0.36 * gvy);
   rgradient('z', 0.36 * gvz);
   delay(gvrt);
   rgradient('x', 0.32 * gvx);
```

```
       rgradient('y', 0.32 * gvy);
       rgradient('z', 0.32 * gvz);
       delay(gvrt);
       rgradient('x', 0.28 * gvx);
       rgradient('y', 0.28 * gvy);
       rgradient('z', 0.28 * gvz);
       delay(gvrt);
       rgradient('x', 0.24 * gvx);
       rgradient('y', 0.24 * gvy);
       rgradient('z', 0.24 * gvz);
       delay(gvrt);
       rgradient('x', 0.20 * gvx);
       rgradient('y', 0.20 * gvy);
       rgradient('z', 0.20 * gvz);
       delay(gvrt); }
     rgradient('x', 0.16 * gvx);
     rgradient('y', 0.16 * gvy);
     rgradient('z', 0.16 * gvz);
     delay(gvrt);
     rgradient('x', 0.12 * gvx);
     rgradient('y', 0.12 * gvy);
     rgradient('z', 0.12 * gvz);
     delay(gvrt);
     rgradient('x', 0.08 * gvx);
     rgradient('y', 0.08 * gvy);
     rgradient('z', 0.08 * gvz);
     delay(gvrt);
     rgradient('x', 0.04 * gvx);
     rgradient('y', 0.04 * gvy);
     rgradient('z', 0.04 * gvz);
     delay(gvrt);
     rgradient('x', 0.00 * gvx);
     rgradient('y', 0.00 * gvy);
     rgradient('z', 0.00 * gvz);
     delay(gvrt); }

/* velocity-encoding lobe 2 of 3 */

   if (gvt >= 40e-6) {
     rgradient('x', 0.04 * gvx * gvel2);
     rgradient('y', 0.04 * gvy * gvel2);
     rgradient('z', 0.04 * gvz * gvel2);
     delay(gvrt);
    ...
     delay(gvrt);
     rgradient('x', 0.00 * gvx * gvel2);
     rgradient('y', 0.00 * gvy * gvel2);
     rgradient('z', 0.00 * gvz * gvel2);
     delay(gvrt); }

/* velocity-encoding lobe 3 of 3 */
```

```

   if (gvt >= 40e-6) {
     rgradient('x', 0.04 * gvx * gvel3);
     rgradient('y', 0.04 * gvy * gvel3);
     rgradient('z', 0.04 * gvz * gvel3);
     delay(gvrt);
    ...
     delay(gvrt);
     rgradient('x', 0.00 * gvx * gvel3);
     rgradient('y', 0.00 * gvy * gvel3);
     rgradient('z', 0.00 * gvz * gvel3);
     delay(gvrt); }

   zero_all_gradients();
   delay(dvac);

/* velocity and acceleration compensation lobe 1 of 3 */

   if (gact >= 40e-6) {
     rgradient('x', 0.04 * gacx);
     rgradient('y', 0.04 * gacy);
     rgradient('z', 0.04 * gacz);
     delay(gacrt);
    ...
     delay(gacrt);
     rgradient('x', 0.00 * gacx);
     rgradient('y', 0.00 * gacy);
     rgradient('z', 0.00 * gacz);
     delay(gacrt); }

/* velocity and acceleration compensation lobe 2 of 3 */

   if (gact >= 40e-6) {
     rgradient('x', 0.04 * gacx * gac2);
     rgradient('y', 0.04 * gacy * gac2);
     rgradient('z', 0.04 * gacz * gac2);
     delay(gacrt);
    ...
     rgradient('x', 0.00 * gacx * gac2);
     rgradient('y', 0.00 * gacy * gac2);
     rgradient('z', 0.00 * gacz * gac2);
     delay(gacrt); }

/* velocity and acceleration compensation lobe 3 of 3 */

   if (gact >= 40e-6) {
     rgradient('x', 0.04 * gacx * gac3);
     rgradient('y', 0.04 * gacy * gac3);
     rgradient('z', 0.04 * gacz * gac3);
     delay(gacrt);

```

```
    ...
     delay(gacrt);
     rgradient('x', 0.00 * gacx * gac3);
     rgradient('y', 0.00 * gacy * gac3);
     rgradient('z', 0.00 * gacz * gac3);
     delay(gacrt); }

   zero_all_gradients();
   delay(dac);

/* 180 pulse for spin echo */

   rgpulse(2 * pw, t1, rof1, rof2);

   delay(decho1);

/* readout */
   status(C);

   setreceiver(t2);
   startacq(alfa);
   acquire(np, 1.0 / sw);
   endacq();

   delay(decho2);

   endacq();
}
```

C.1.1 VnmrJ Parameters

The VnmrJ pulse sequence parameters used in the combustion studies are detailed in Table C.1.

Table C.1: Parameters used in data presented.

Variable	Value	Units
at	200	ms
d1	300	ms
enct	4	ms
gacrt	4	µs
gact	160	µs
gacx	17912	DAQ units
gacy	18968	DAQ units
gacz	18968	DAQ units
gain	30	dB
gvrt	4	µs
gvt	200	µs
gvx	13911	DAQ units
gvy	13911	DAQ units
gvz	13911	DAQ units
np	400	
nt	4	
pw	28.5	µs
sfrq	110.5743289	MHz
sw	1000	Hz
tof	0	Hz
tpwr	55	dB
tr	0	s

C.2 MATLAB: Read FID

The MATLAB code for reading the free induction decay (**fid**) binary data file is presented here.

```
function [dta, fheader, bheader] = readfid(filename, n)

% READFID: function to read binary VnmrJ fid data file
%
% call syntax:
%  function [dta, fheader, bheader] = readfid(filename, n)
%
% input:
%  filename: VnmrJ fid file to read (format: 'filename.fid/fid')
%  n: number of points at the end of fid to use for baseline correction ...
%   (-1 = no correction)
%
% output:
%  dta: returned fid(s) (a np*ntraces/2 by nblocks array)
%  fheader: returned fid file header information (9 total fields)
%  bheader: returned fid block header information for the last block ...
%   that was read (9 fields)
%
% MODIFIED BY J. PETER MUSTONEN 2010-NOV-22
% Reference: VnmrJ User Programming
% -------------------------------------------------------------------------

% create empty structure arrays for fheader and bheader:
fheader = struct('nblocks', {0}, 'ntraces', {0}, 'np', {0}, 'ebytes', ...
 {0}, 'tbytes', {0}, 'bbytes', {0}, 'vers_id', {0}, 'status', {0}, ...
 'nbheaders',{0});
bheader = struct('scale',{0},'status',{0},'index',{0},'mode',{0}, ...
 'ctcount',{0},'lpval',{0},'rpval',{0},'lvl',{0},'tlt',{0});

% open binary VnmrJ data file:
f = fopen(filename, 'r', 'b');

% read fid file header information from binary data file (9 fields):
fheader.nblocks = fread(f, 1, 'long');   % number of blocks in file
fheader.ntraces = fread(f, 1, 'long');   % number of traces per block
fheader.np = fread(f, 1, 'long');        % number of elements per trace
fheader.ebytes = fread(f, 1, 'long');    % number of bytes per element
fheader.tbytes = fread(f, 1, 'long');    % number of bytes per trace
fheader.bbytes = fread(f, 1, 'long');    % number of bytes per block
fheader.vers_id = fread(f, 1, 'short');  % software version, file_id ...
                                         %  status bits
fheader.status = fread(f, 1, 'short');   % status of whole file
fheader.nbheaders = fread(f, 1, 'long'); % number of block headers per ...
                                         %  block
```

```

% preallocate empty data array:
dta = zeros(fheader.np * fheader.ntraces / 2, fheader.nblocks);

% read each of nblocks of data from binary data file:
%  generates a np*ntraces/2 by nblocks array
for fv = 1:fheader.nblocks

    % read fid block header information from binary data file (9 fields)
    bheader.scale = fread(f, 1, 'short');  % scaling factor
    bheader.status = fread(f, 1, 'short'); % status of data in block
    bheader.index = fread(f, 1, 'short');  % block index
    bheader.mode = fread(f, 1, 'short');   % mode of data in block
    bheader.ctcount = fread(f, 1, 'long'); % ct value for FID
    bheader.lpval = fread(f, 1, 'float');  % f2 (2D-f1) left phase in ...
                                           %  phasefile
    bheader.rpval = fread(f, 1, 'float');  % f2 (2D-f1) right phase in ...
                                           %  phasefile
    bheader.lvl = fread(f, 1, 'float');    % level drift correction
    bheader.tlt = fread(f, 1, 'float');    % tilt drift correction

    % read fid data from binary data file:
    %  generates a column vector of length np*ntraces
    d = fread(f, fheader.np * fheader.ntraces, 'float32');

    % reshape fid data into a 2 by np*ntraces/2 array:
    %  splits data into real and imaginary row vectors
    d = reshape(d, 2, size(d,1) / 2);

    % transpose fid data into a np*ntraces/2 by 2 array:
    %  converts to real and imaginary column vectors
    d = transpose(d);

    % combine the real and imaginary column vectors into a complex vector:
    %  C = COMPLEX(A,B) returns the complex result A + Bi
    d = complex(d(:,1), d(:,2));

    % perform baseline correction as specified by n in call syntax
     if n >= 0
        d = d - mean(d(end - n:end)); % subtract mean of last n points
        dta(:, fv) = d;               % append vector to data array
     else
        dta(:, fv) = d;               % append vector to data array
     end
end

% close binary VnmrJ data file:
fclose(f);

end
```

C.3 MATLAB: Parameters

The MATLAB code for extracting parameters from the parameter (**procpar**) binary file is presented here.

```matlab
function p = readpar(filename, parname)

% READPAR: function to read parameter value or parameter array from ...
%  VnmrJ binary parameter file
%
% call syntax:
%  function p = readpar(filename, parname)
%
% input:
%  filename: path to vnmr procpar file (format: 'filename.fid/procpar')
%  parname: name of parameter to read (format: 'parname')
%
% output:
%  p: returned parameter value or parameter array
%
% CREATED BY XIN ZHOU 2007-OCT-07
% MODIFIED BY J. PETER MUSTONEN 2010-NOV-22
% Reference: VnmrJ User Programming
% -------------------------------------------------------------------------

% insert space after parameter name string
parnm = [parname ' '];

% open binary VnmrJ data file:
f = fopen(filename, 'r', 'b');

% get first line of binary data file:
line = fgetl(f);

% compare line to parameter name, continue until line is found:
    while (~strncmp(line, parnm, size(parnm, 2))) && (~feof(f))
        line = fgetl(f); % get the next line
    end

% get next line, which contains parameter value
line = fgetl(f);

% close binary VnmrJ data file:
fclose(f);

% retrieve parameter value(s) from line:
nparray = sscanf(line, '%f', inf);

% remove array size
```

```
parray = nparray(2:end);

% assign retrieved parameter value to output p
p = parray;

end
```

C.4 MATLAB: Data Processing

The code presented here, **process_csi_vel_ac.m**, is used to process data collected using the “csi_vel_ac.c” pulse sequence in anywhere from one to four dimensions.

```
function process_csi_vel_ac(filename, zf_time, zf_space, piecedata)

% PROCESS_CSI_VEL_AC: function to process VnmrJ data acquired using ...
%  csi_vel_ac, which is a chemical shift imaging pulse sequence with ...
%  a three-lobed velocity-encoding gradient pulse followed by a ...
%  three-lobed position-encoding gradient pulse, both sandwiched ...
%  between spin-echo 90 and 180 RF pulses, with immediate data ...
%  acquisition after the 180
%
% call syntax:
%  process_csi_vel_ac(filename, zf_time, zf_space, piecedata)
%
% input:
%  filename: VnmrJ fid file folder to read (format: 'filename.fid')
%  zf_time: amount of zero-filling in direct (time) dimension (none [0] ...
%   by default; linear scaling [1 doubles, 2 triples, etc.]; ...
%   non-negative integers)
%  zf_space: amount of zero-filling in space dimension (none [0] by ...
%   default; quadratic scaling to powers of two; non-negative integers)
%  piecedata: if the dataset was collected piecewise, reconstruct the ...
%   full dataset first and use as an input (optional)
%
% output (saved as arrays):
%  sfrq: transmitter frequency
%  nt: number of transients
%  plane: dimensionality of the data (0 1-D, 1 axial, 2 coronal, ...
%   3 sagittal, 4 3-D)
%  xpos, ypos, zpos: position information for indices of arrays (in mm)
%  img: xenon density image array [ZYX(V)] (zero-filled if specified)
%  csimg: chemical shift image array [ZYX(V)] (zero-filled if specified)
%  velplane: velocity dimension (1 for x, 2 for y, 3 for z; optional)
%  phase_angle: phase difference array
%  velocity: velocity arrray (optional)
%  min_angle: minimum phase difference (optional)
%  max_angle: maximum phase difference (optional)
% CREATED BY DOMINIC GRAZIANI & J. PETER MUSTONEN 2009-DEC-04
```

```
% EDITED BY J. PETER MUSTONEN 2010-DEC-27
% ---------------------------------------------------------------------------

% set pre-fit trimming, apodization, and thresholding parameters:
%  exp_thresh: threshold for data to be used in determining exponential fit
%  gauss_thresh: threshold to be used for gaussian fit
%  sigmas: amount of times to multiply the gaussian sigma value by ...
%   for apodization
%  signal_thresh: all values in the final img array less than this ...
%   threshold will be set as NaN; this mask is also mapped to csimg
exp_thresh = exp(-2);
gauss_thresh = .1;
sigmas = 4;
signal_thresh = .1;

% constants:
gammabar_xe = 0.0011777; % us-1 G-1

% set default zero-filling levels to none:
if nargin == 1
    zf_time = 0;
    zf_space = 0;
end

% check for input errors:
if ceil(zf_time) ~= zf_time || ceil(zf_space) ~= zf_space
    error('zero-filling values must be integers!')
end
if zf_time < 0 || zf_space < 0
    error('zero-filling values must be non-negative integers!')
end

% use readpar to get acquisition parameters:
%  function p = readpar(filename, parname)
%  enct: total encoding time between 90 and 180 (sec); also echo time
%  gvt: vel gradient lobe duration (sec)
%  gvx, gvy, gvz: gradient in first lobe of each vel gradient (DAQ units)
%  gact: ac gradient lobe duration (sec)
%  gacx, gacy, gacz: gradient in first lobe of each ac gradient (DAQ units)
%  sfrq: transmitter frequency to observe nucleus (MHz)
%  sw: spectral width in directly detected dimension (Hz)
%  tof: frequency offset for observe transmitter (Hz)
enct = readpar(strcat(filename, '/procpar'), 'enct');
gact = readpar(strcat(filename, '/procpar'), 'gact');
gacx = readpar(strcat(filename, '/procpar'), 'gacx');
gacy = readpar(strcat(filename, '/procpar'), 'gacy');
gacz = readpar(strcat(filename, '/procpar'), 'gacz');
gvt = readpar(strcat(filename, '/procpar'), 'gvt');
gvx = readpar(strcat(filename, '/procpar'), 'gvx');
gvy = readpar(strcat(filename, '/procpar'), 'gvy');
gvz = readpar(strcat(filename, '/procpar'), 'gvz');
```

```
sfrq = readpar(strcat(filename, '/procpar'), 'sfrq');
sw = readpar(strcat(filename, '/procpar'), 'sw');
tof = readpar(strcat(filename, '/procpar'), 'tof');
nt = readpar(strcat(filename, '/procpar'), 'nt');

% replace gacx if data is piecewise:
%  note that this relies on complete gacx and gacy vectors being equivalent
if nargin == 4
    gacx = readpar(strcat(filename, '/procpar'), 'gacy');
end

% check for order and symmetry of gradients:
if gacx(1) > gacx(end) || gacy(1) > gacy(end) || gacz(1) > gacz(end) || ...
 gvx(1) > gvx(end) || gvy(1) > gvy(end) || gvz(1) > gvz(end)
    error('one of gradients is backwards!')
end
if gacx(1) ˜= −gacx(end) || gacy(1) ˜= −gacy(end) || gacz(1) ˜= ...
 −gacz(end) || gvx(1) ˜= −gvx(end) || gvy(1) ˜= −gvy(end) || gvz(1) ˜= ...
 −gvz(end)
    error('one of gradients is not symmetric!')
end

% create vector of image dimensions:
spacedims = [size(gacx, 1), size(gacy, 1), size(gacz, 1)];
veldims = [size(gvx, 1), size(gvy, 1), size(gvz, 1)];

% determine orientation from image dimensions:
%  plane: orientation (1 for axial, 2 for coronal, 3 for sagittal)
%  onedimindex: 1−D axis (1 for x, 2 for y, 3 for z)
%  genc1, genc2: encoding gradient values in each dimension (DAQ units)
if max(spacedims) == sum(spacedims) − 2
    plane = 0;
    [imagedims, onedimindex] = max(spacedims);
    if onedimindex == 1
        genc1 = gacx;
    else
        if onedimindex == 2;
            genc1 = gacy;
        else
            genc1 = gacz;
        end
    end
else
    onedimindex = 0;
    if spacedims(1) > 1 && spacedims(2) > 1 && spacedims(3) == 1
        plane = 1;
        imagedims = spacedims(1:2);
        genc1 = gacx;
        genc2 = gacy;
    else
        if spacedims(1) > 1 && spacedims(2) == 1 && spacedims(3) > 1
```

```
            plane = 2;
            imagedims = [spacedims(1), spacedims(3)];
            genc1 = gacx;
            genc2 = gacz;
        else
            if spacedims(1) == 1 && spacedims(2) > 1 && spacedims(3) > 1
                plane = 3;
                imagedims = spacedims(2:3);
                genc1 = gacy;
                genc2 = gacz;
            else
                plane = 4;
                imagedims = spacedims;
                genc1 = gacx;
                genc2 = gacy;
                genc3 = gacz;
            end
        end
    end
end
datadims = fliplr(imagedims);
midpoints = (datadims + 1) / 2;

% determine velocity information:
%  velplane: velocity plane (1 for x, 2 for y, 3 for z)
if veldims(1) > 1
    velplane = 1;
    vdatadims = [veldims(1), datadims];
    gvenc = gvx;
else
    if veldims(2) > 1
        velplane = 2;
        vdatadims = [veldims(2), datadims];
        gvenc = gvy;
    else
        if veldims(3) > 1
            velplane = 3;
            vdatadims = [veldims(3), datadims];
            gvenc = gvz;
        else
            velplane = 0;
            gvenc = 0;
        end
    end
end

% read binary VnmrJ fid file:
%  function [dta, fheader, bheader] = readfid(filename, n)
%   note: -1 is for no baseline correction
%  data: returned fid(s) (a np * ntraces / 2 by nblocks array)
data = readfid(strcat(filename, '/fid'), -1);
```

```

% replace data with full data set if collected piecewise:
if nargin == 4
    data = piecedata;
end

% reshape data into three dimensions:
%  (time, k-space) to (time, k-space2, k-space1)
%  note 1: in two-dimensional data, the dimension with the second array ...
%   order actually comes first in the data, because it is arrayed over ...
%   each value of the dimension with first order
%  note 2: because the gradients are typically arrayed from negative to ...
%   positive (steps), and because the spin echo inverts this, the first ...
%   k-space indices are both in positive k-space
if velplane == 0
    rawdims = [size(data, 1), datadims];
else
    rawdims = [size(data, 1), vdatadims];
end
tdata = reshape(data, rawdims);
if velplane > 0
    if plane == 0
        tdata = permute(tdata, [1, 3, 2]);
        permdims = size(tdata);
    else
        if plane ~= 0 && plane < 4
            tdata = permute(tdata, [1, 3, 4, 2]);
            permdims = size(tdata);
        else
            tdata = permute(tdata, [1, 3, 4, 5, 2]);
            permdims = size(tdata);
        end
    end
else
    permdims = size(tdata);
end

% flip z-dimension if present:
if plane > 1 || onedimindex == 3
    tdata = flipdim(tdata, 2);
end
if velplane == 3
    velzindex = ndims(tdata);
    tdata = flipdim(tdata, velzindex);
end

% trim points before echo:
ttdata = tdata((enct * sw):end, :, :, :, :);

% preeallocate final apodized array:
fapo_ttdata = zeros(size(ttdata));
```

```

% save full-velocity data prior to trimming for apodization:
vttdata = ttdata;

% excise dataset with no velocity-encode for apodization:
if velplane > 0
    if plane == 0
        ttdata = vttdata(:, :, 2);
    else
        if plane ~= 0 && plane < 4
            ttdata = vttdata(:, :, :, 2);
        else
            ttdata = vttdata(:, :, :, :, 2);
        end
    end
end

% define data for apodization fitting:
if plane == 0
    kzero = ttdata(:, midpoints);
    kspace1 = (ttdata(1, :))';
else
    if plane ~= 0 && plane < 4
        kzero = ttdata(:, midpoints(1), midpoints(2));
        kspace1 = (ttdata(1, :, midpoints(2)))';
        kspace2 = squeeze(ttdata(1, midpoints(1), :));
    else
        kzero = ttdata(:, midpoints(1), midpoints(2), midpoints(3));
        kspace1 = (ttdata(1, :, midpoints(2), midpoints(3)))';
        kspace2 = squeeze(ttdata(1, midpoints(1), :, midpoints(3)));
        kspace3 = squeeze(ttdata(1, midpoints(1), midpoints(2), :));
    end
end

% determine exponential apodization fit:
ttrim = 0;
while abs(kzero(end - ttrim)) < exp_thresh * max(abs(kzero))
    ttrim = ttrim + 1;
end
tkzero = kzero(1:(end - ttrim));
exp_fit = polyfit((1:size(tkzero))', log(abs(tkzero)), 1);
lambda = -exp_fit(1);

% determine gaussian apodization fit 1:
kt_index1 = 1;
while abs(kspace1(midpoints(1) - kt_index1)) > gauss_thresh * ...
 max(abs(kspace1))
    kt_index1 = kt_index1 + 1;
    if kt_index1 < midpoints(1) - 1
        continue
    else
```

```
        break
    end
end
ktrim1 = midpoints(1) - kt_index1;
tkspace1 = kspace1((ktrim1 + 1):(end - ktrim1));
gauss_fit1 = polyfit((1:size(tkspace1))', log(abs(tkspace1)), 2);
sigma1_actual = sqrt(-1 / (2 * gauss_fit1(1)));
sigma1 = sigmas * sigma1_actual;

% determine gaussian apodization fit 2:
if plane > 0
    kt_index2 = 1;
    while abs(kspace2(midpoints(2) - kt_index2)) > gauss_thresh * ...
     max(abs(kspace2))
        kt_index2 = kt_index2 + 1;
        if kt_index1 < midpoints(2) - 1
            continue
        else
            break
        end
    end
    ktrim2 = midpoints(2) - kt_index2;
    tkspace2 = kspace2((ktrim2 + 1):(end - ktrim2));
    gauss_fit2 = polyfit((1:size(tkspace2))', log(abs(tkspace2)), 2);
    sigma2_actual = sqrt(-1 / (2 * gauss_fit2(1)));
    sigma2 = sigmas * sigma2_actual;
end

% determine gaussian apodization fit 3:
if plane == 4
    kt_index3 = 1;
    while abs(kspace3(midpoints(3) - kt_index3)) > gauss_thresh * ...
     max(abs(kspace3))
        kt_index3 = kt_index3 + 1;
        if kt_index1 < midpoints(2) - 1
            continue
        else
            break
        end
    end
    ktrim3 = midpoints(3) - kt_index3;
    tkspace3 = kspace3((ktrim3 + 1):(end - ktrim3));
    gauss_fit3 = polyfit((1:size(tkspace3))', log(abs(tkspace3)), 2);
    sigma3_actual = sqrt(-1 / (2 * gauss_fit3(1)));
    sigma3 = sigmas * sigma3_actual;
end

% split into velocity lobes:
for velindex = 1:max(veldims)
    if velplane > 0
        if plane == 0
```

```
            ttdata = vttdata(:, :, velindex);
        else
            if plane ~= 0 && plane < 4
                ttdata = vttdata(:, :, :, velindex);
            else
                ttdata = vttdata(:, :, :, :, velindex);
            end
        end
    end

% create filters and apply them:
filterarray = exp(-lambda * (0:(size(ttdata, 1) - 1)))';
bigfilter = repmat(filterarray, [1, datadims]);
apo_ttdata = bigfilter .* ttdata;
filterarray1 = exp(-(((1:datadims(1)) - midpoints(1)).^2 / 2 / sigma1^2))';
filterarray1 = reshape(filterarray1, [1, datadims(1)]);
bigfilter1 = repmat(filterarray1, [size(ttdata, 1), 1, datadims(2:end)]);
apo_ttdata1 = bigfilter1 .* apo_ttdata;
if plane == 0
    fapo_ttdata(:, :, velindex) = apo_ttdata1;
else
    filterarray2 = exp(-(((1:datadims(2)) - midpoints(2)).^2 / 2 / ...
     sigma2^2))';
    filterarray2 = reshape(filterarray2, [1, 1, datadims(2)]);
    if plane < 4
        bigfilter2 = repmat(filterarray2, [size(ttdata, 1), ...
         datadims(1), 1]);
        apo_ttdata2 = bigfilter2 .* apo_ttdata1;
        fapo_ttdata(:, :, :, velindex) = apo_ttdata2;
    else
        bigfilter2 = repmat(filterarray2, [size(ttdata, 1), ...
         datadims(1), 1, datadims(3)]);
        apo_ttdata2 = bigfilter2 .* apo_ttdata1;
        filterarray3 = exp(-(((1:datadims(3)) - midpoints(3)).^2 / 2 / ...
         sigma3^2))';
        filterarray3 = reshape(filterarray3, [1, 1, 1, datadims(3)]);
        bigfilter3 = repmat(filterarray3, [size(ttdata, 1), ...
         datadims(1), datadims(2), 1]);
        apo_ttdata3 = bigfilter3 .* apo_ttdata2;
        fapo_ttdata(:, :, :, :, velindex) = apo_ttdata3;
    end
end

% close for loop for velocity indexing:
end

% set dimensions of zero-filled array:
zfdims = [(zf_time + 1) * permdims(1), permdims(2:end)];
if zf_space ~= 0
    if velplane == 0
        zfdims(2:end) = 2.^(floor(log2(permdims(2:end))) + zf_space) + 1;
```

```
    else
        zfdims(2:end-1) = 2.^(floor(log2(permdims(2:end - 1))) + ...
         zf_space) + 1;
    end
end

% Fourier transform direct dimension:
%  (time, k-space2, k-space1) to (frequency, k-space2, k-space1)
fdata1 = fftshift(fft(fapo_ttdata, zfdims(1), 1), 1);

% generate a frequency range based on spectral width:
%  if there is an offset frequency, adjust frequency data
%  convert to chemical shift in ppm
freq = (linspace(sw/2, -sw/2, zfdims(1)))';
corr_freq = freq + tof;
cs_ppm = corr_freq / sfrq;

% sum frequency data for spectral range determination:
%  sdata is a vector
sdata = sum(sum(sum(sum(abs(fdata1), 2), 3), 4), 5);
[peak freqind] = max(sdata);

% set spectral range:
%  freq_range is +/- 100 Hz (~ +/- 1 ppm at 9.4 T)
%  spect_range matches this based on zero-filling
%  pick out relevant chemical shifts
spect_bars = 100 * size(freq, 1) / sw;
spect_range = (freqind - spect_bars):(freqind + spect_bars);
csi_ppm = cs_ppm(spect_range);

% trim fdata based on spectral range:
tfdata1 = fdata1(spect_range, :, :, :, :);

% Fourier transform in spatial dimensions:
tfdata2 = fftshift(fft(tfdata1, zfdims(2), 2), 2);
if plane == 0
    tfdata = tfdata2;
else
    tfdata3 = fftshift(fft(tfdata2, zfdims(3), 3), 3);
    if plane ~= 0 && plane < 4
        tfdata = tfdata3;
    else
        tfdata = fftshift(fft(tfdata3, zfdims(4), 4), 4);
    end
end

% generate density arrays:
%  original dimensions or zero-filled (if specified)
%  sum spectra over spect_range
%  first dimension (rows) is image-space 2 (negative to positive)
%  second dimension (columns) is image-space 1 (negative to positive)
```

```
img = squeeze(sum(tfdata, 1));

% determine chemical shift for each voxel:
[cs_max, cs_ind] = max(abs(tfdata));
cs_ind = squeeze(cs_ind);

% generate csi image array:
tfdatasize = size(tfdata);
csimgsize = tfdatasize(2:end);
csimg = zeros(csimgsize);
for na = 1:csimgsize(1)
    if size(csimgsize, 2) == 1
        csimg(na)= csi_ppm(cs_ind(na));
    else
        for nb = 1:csimgsize(2)
            if size(csimgsize, 2) == 2
                csimg(na, nb)= csi_ppm(cs_ind(na, nb));
            else
                for nc = 1:csimgsize(3)
                    if size(csimgsize, 2) == 3
                        csimg(na, nb, nc)= csi_ppm(cs_ind(na, nb, nc));
                    else
                        for nd = 1:csimgsize(4)
                            csimg(na, nb, nc, nd)= csi_ppm(cs_ind(na, ...
                             nb, nc, nd));
                        end
                    end
                end
            end
        end
    end
end

% set all low signal voxels to NaN (not a number):
amplitude = abs(img) / max(max(max(max(abs(img)))));
img(amplitude < signal_thresh) = NaN;
csimg(amplitude < signal_thresh) = NaN;

% determine field of view for plots (in mm):
%  factor of ten is conversion from cm to mm
gact_us = gact * 10^6;
if gact_us <= 200 % triangles
    scale_tri = 48/89;
    steps_strength = scale_tri * 100 / 32767;
    area1 = steps_strength * max(genc1) * gact_us / 2;
    if plane > 0
        area2 = steps_strength * max(genc2) * gact_us / 2;
        if plane == 4
            area3 = steps_strength * max(genc3) * gact_us / 2;
        end
    end
```

```
end
if gact_us > 200 % trapezoids
    ramp_time = 100;
    rr = ramp_time / gact_us;
    scale_trap = 12 * (1 - rr) / (22 + rr - rr^2);
    steps_strength = scale_trap * 100 / 32767;
    area1 = steps_strength * max(genc1) * (gact_us - 100);
    if plane > 0
        area2 = steps_strength * max(genc2) * (gact_us - 100);
        if plane == 4
            area3 = steps_strength * max(genc3) * (gact_us - 100);
        end
    end
end
fov1 = 10 * (imagedims(1) - 1) / (gammabar_xe * 2 * area1);
posmax1 = fov1 / 2;
if plane > 0
    fov2 = 10 * (imagedims(2) - 1) / (gammabar_xe * 2 * area2);
    posmax2 = fov2 / 2;
    if plane == 4
        fov3 = 10 * (imagedims(3) - 1) / (gammabar_xe * 2 * area3);
        posmax3 = fov3 / 2;
    end
end

% determine position in zero-filled image-space (in mm):
switch plane
    case 0
        switch onedimindex
            case 1
                xpos = linspace(-posmax1, posmax1, zfdims(2));
                ypos = 0;
                zpos = 0;
            case 2
                xpos = 0;
                ypos = linspace(-posmax1, posmax1, zfdims(2));
                zpos = 0;
            case 3
                xpos = 0;
                ypos = 0;
                zpos = linspace(-posmax1, posmax1, zfdims(2));
        end
    case 1
        xpos = linspace(-posmax1, posmax1, zfdims(3));
        ypos = linspace(-posmax2, posmax2, zfdims(2));
        zpos = 0;
    case 2
        xpos = linspace(-posmax1, posmax1, zfdims(3));
        ypos = 0;
        zpos = linspace(-posmax2, posmax2, zfdims(2));
    case 3
```

```
        xpos = 0;
        ypos = linspace(-posmax1, posmax1, zfdims(3));
        zpos = linspace(-posmax2, posmax2, zfdims(2));
    case 4
        xpos = linspace(-posmax1, posmax1, zfdims(4));
        ypos = linspace(-posmax2, posmax2, zfdims(3));
        zpos = linspace(-posmax3, posmax3, zfdims(2));
end

% determine phase difference and velocity:
%  phase difference should not approach pi
if velplane > 0
    if plane == 0
        phasefinal = squeeze(img(:, 1)) .* conj(squeeze(img(:, end)));
    else
        if plane ~= 0 && plane < 4
            phasefinal = squeeze(img(:, :, 1)) .* ...
             conj(squeeze(img(:, :, end)));
        else
            phasefinal = squeeze(img(:, :, :, 1)) .* ...
             conj(squeeze(img(:, :, :, end)));
        end
    end
    phase_angle = angle(phasefinal);
    venc = 1 / (gammabar_xe * max(gvenc) * (100 / 32767) * (gvt * 1e6)^2);
    velocity = 1e6 * venc * phase_angle / pi; % cm s-1
    min_angle = round(100 * min(min(min(phase_angle)))) / 100;
    max_angle = round(100 * max(max(max(phase_angle)))) / 100;
end

% save data:
dataname = strcat(filename(1:end - 4), '_data');
if velplane == 0
    save(dataname, 'sfrq', 'nt', 'plane', 'xpos', 'ypos', 'zpos', ...
     'img', 'csimg')
else
    save(dataname, 'sfrq', 'nt', 'plane', 'xpos', 'ypos', 'zpos', ...
     'img', 'csimg', 'velplane', 'phase_angle', 'velocity', ...
     'min_angle', 'max_angle')
end
```

Appendix D

Graduate Research Conference Abstract

"Remote Detection of NMR/MRI with Atomic Magnetometry at the Earth's Magnetic Field"

-Presented October 2, 2008 to the Department of Chemistry, UC Berkeley

Nuclear magnetic resonance (NMR) and magnetic resonance imaging (MRI) are non-invasive techniques, which use inductive detection to measure nuclear magnetization. Large, cryogenically-cooled magnets (1.5 to 22.3 T) are required, as the sensitivity of inductive detection increases at higher fields. Moving to lower field strength can make NMR/MRI less expensive and more portable, and allows imaging of samples with magnetic susceptibility gradients that distort images at high fields. It also enables imaging inside of metallic materials, which is impossible with standard inductive detection at high fields due to radio frequency screening. Improved sensitivity at lower fields can be realized using several techniques, one of which is optical atomic magnetometry (AM), which can be made portable and inexpensive.

In AM, a cell filled with alkali metal vapor is subject to a magnetic field that produces Zeeman splitting of the energy states. Optical pumping at the D1 transition of the alkali atom causes precession in the magnetic field, which in turn causes optical rotation of the light (known as Faraday rotation), the measurement of which allows calculation of the applied magnetic field. With remote detection techniques the pre-polarization, encoding, and detection steps are spatially separated and can therefore be individually optimized (see Xu [69] Fig. 1). This allows for better sensitivity by concentrating the sample in close proximity to the detection cells, improving the so-called "filling factor". It also reduces the need for frequency matching of alkali resonance to nuclear resonance as longitudinal magnetization is measured (as opposed to transverse magnetization).

In our system two 1 cm^3 ^{87}Rb-enriched vapor cells with anti-relaxation coating are used. A gradiometric setup is employed to reduce common-mode noise. We perform most imaging at or around Earth's field ($\approx$ 50 µT), with a magnetometric sensitivity of approximately

80 fT/Hz$^{1/2}$ (for this geometry). Both NMR and MRI (spatial information) studies of water flow have been performed using this apparatus. Images of water flow inside of metallic materials (solid and porous samples) and fluid mixing have been acquired by selective polarization of the spins using simple permanent magnets. We have also measured the relaxivity of gadolinium (used for T_1-weighted imaging in MRI) at Earth's field for the first time.

I will be exploring improvements to system sensitivity including alternate pre-polarization techniques such as T_1 relaxation agents, hyperpolarized xenon, and dynamic nuclear polarization. Improved sensitivity will allow low-field imaging of microfluidic flow, and I will be investigating the potential biochemical and analytical applications this will enable. Detecting neuronal currents may be possible at low-field, by bringing their low frequency electrical activities into resonance with magnetic spin precession. My current work involves exploiting the temperature dependence of the relaxation of hyperpolarized ^{129}Xe to image combustion at high-field, with the goal of microscale combustion analysis using AM. AM has the potential to be a portable, inexpensive, sensitive, environmentally-friendly, and non-invasive detection method with numerous applications.

Appendix E

Combustion Project Reference Material

E.1 Original Combustion Project Idea

-From “Microfluidics Projects - Partial Summary,” June 30, 2008

There is considerable interest in new methods to probe combustion processes on the microscale. Using xenon gas or a parahydrogen-derived fuel as a tracer, we can first examine combustion in open and confined flames, then smoldering combustion and, finally, microscale combustion devices including microfluidic channels, turbines, and miniature rocket nozzles. These devices are an important contribution to the Lawrence Berkeley National Laboratory (LBNL) energy initiative because they have power densities far greater than conventional batteries.

E.2 51st Experimental NMR Conference

E.2.1 Abstract Summary

“Hyperpolarized Xenon Magnetic Resonance Imaging of Combustion Processes”
-Submitted January 12, 2010

There is considerable interest in new methods to probe the chemistry and thermodynamics of enclosed combustion processes. This study exploits the sensitivity of the chemical shift of xenon-129 to temperature and pressure to visualize combustion, beginning with MRI of an open diffusion flame. Combustion MRI is challenging due to the high temperatures and fast dynamics involved. A modified chemical shift imaging pulse sequence with velocity and acceleration compensation was used to generate chemical shift images of xenon-129 during combustion with a homebuilt water-cooled probe. This method can be applied to smoldering combustion, and remotely-detected imaging of microscale combustion processes including flames in microfluidic channels, miniature turbines and rocket nozzles, which are of interest due to their relatively high power densities.

E.2.2 Full Abstract

“Hyperpolarized Xenon Magnetic Resonance Imaging of Combustion Processes”
-Submitted January 12, 2010

There is considerable interest in new methods to probe the chemistry and thermodynamics of enclosed combustion processes. The use of nuclear magnetic resonance imaging (MRI) to visualize combustion is challenging due to the high temperatures and fast dynamics involved. A previous study sought to directly acquire proton images of burning methane jets using cooled sample chambers and relaxation-optimized single-point imaging (SPRITE) [22] to circumvent these issues. However, this strategy only partially ameliorated these problems, as the reaction itself leads to a loss of sensitivity due to the low proton thermal polarization and low spin density.

A second approach involves the imaging of a reporter or tracer molecule that is not itself involved in the combustion reaction, but whose magnetic properties change as a function of the thermodynamic parameters of interest. The spin polarization of hyperpolarized (HP) ^{129}Xe can be enhanced four to five orders of magnitude over the thermal equilibrium, which enables imaging of HP ^{129}Xe gas at low density, but with high sensitivity. Moreover, the chemical shift of ^{129}Xe is sensitive to both temperature and vapor densities [34]. An earlier study utilized HP ^{129}Xe as a reporter for the combustion of methane over a nanoporous material bed, using NMR spectroscopy (2D-EXSY) to investigate mixing within the regions of the flame [1]. By using HP ^{129}Xe, our study exploits the sensitivity of the chemical shift to temperature and pressure to visualize combustion processes, beginning with MRI of an open diffusion flame of dimethyl ether (DME).

HP ^{129}Xe is premixed with DME and combines with oxygen at a flame (Figure E.1a) that is contained inside of a water-cooled, four foot long ceramic tube that thermally isolates it from the bore of the magnet (9.4 T). A smaller ceramic tube contains the flame itself and protects the 15 mm RF coil (coated with mica tape) from the direct flame. A modified chemical shift imaging (CSI) pulse sequence with velocity and acceleration compensation was used to generate density-weighted images (Figure E.1b and E.1c) and chemical shift-weighted images (not shown) of ^{129}Xe with and without active combustion.

This method can be applied to imaging of confined processes, such as smoldering combustion, and remotely-detected imaging of microscale combustion processes including flames in microfluidic channels, miniature turbines and rocket nozzles. These devices are of interest because they have power densities far greater than conventional batteries, and are an alternative to fuel cells for portable power applications based on hydrocarbon fuels instead of chemical batteries.

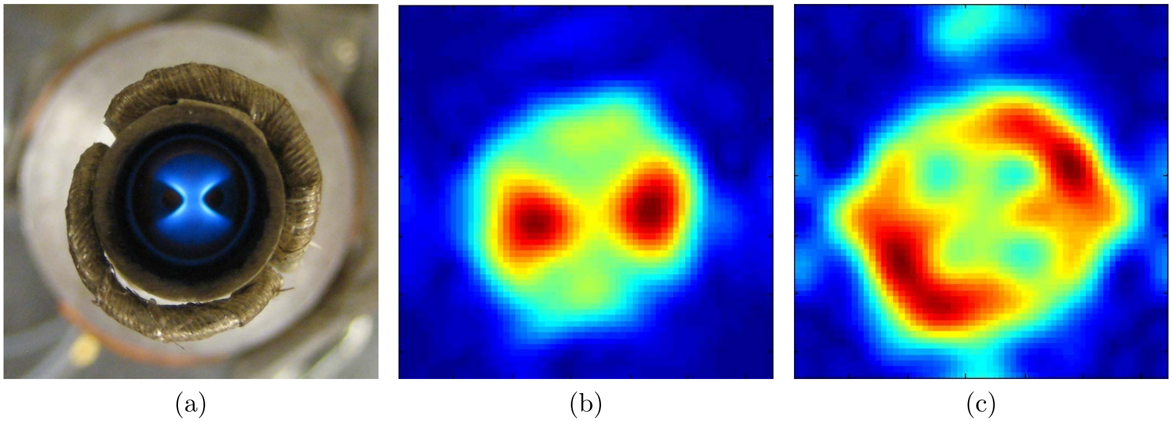
(a) (b) (c)

Figure E.1: (a) A photograph of the homebuilt coil outside of the 12.7 mm ceramic tube containing the flame (≈ 20 mm in height, blue). Channels along the horizontal and vertical axes deliver Xe/DME and oxygen respectively. (b) ^{129}Xe density-weighted image before combustion. (c) Image during combustion.

E.2.3 Poster

"Hyperpolarized Xenon Magnetic Resonance Imaging of Combustion Processes"

-Presented at: 51st Experimental Nuclear Magnetic Resonance Conference (ENC), Daytona Beach, FL. April 18-23, 2010 (Poster 078)

Abstract

There is considerable interest in new methods to probe the chemistry and thermodynamics of enclosed combustion processes. This study exploits the sensitivity of the chemical shift of xenon-129 to temperature and pressure to visualize combustion, beginning with magnetic resonance imaging (MRI) of an open diffusion flame. A chemical shift imaging pulse sequence with velocity and acceleration compensation was used to generate chemical shift images of xenon-129 during combustion with a homebuilt water-cooled probe. This method can be applied to smoldering combustion, and remotely-detected imaging of microscale combustion processes including flames in microfluidic channels, miniature turbines and rocket nozzles, which are of interest due to their relatively high power densities.

Background

Combustion MRI is challenging due to the high temperatures and fast dynamics involved. A previous study sought to directly acquire proton images of burning methane jets using cooled sample chambers and relaxation-optimized single-point imaging (SPRITE) [22] to circumvent these issues. However, this strategy only partially ameliorated these problems, as the reaction itself leads to a loss of sensitivity due to the low proton thermal polarization and low spin density.

A second approach involves the imaging of a reporter or tracer molecule that is not itself involved in the combustion reaction, but whose magnetic properties change as a function of the thermodynamic parameters of interest. The spin polarization of hyperpolarized (HP) ^{129}Xe can be enhanced four to five orders of magnitude over the thermal equilibrium, which enables imaging of HP ^{129}Xe gas at low density, but with high sensitivity. Moreover, the chemical shift of ^{129}Xe is sensitive to both temperature and vapor densities [34]. An earlier study utilized HP ^{129}Xe as a reporter for the combustion of methane over a nanoporous material bed, using NMR spectroscopy (2D-EXSY) to investigate mixing within the regions of the flame [1]. By using HP ^{129}Xe, our study exploits the sensitivity of the chemical shift to temperature and pressure to visualize combustion processes, beginning with MRI of an open diffusion flame of dimethyl ether (DME). During combustion the increased temperature and decreased density is expected to lead to a decreased chemical shift.

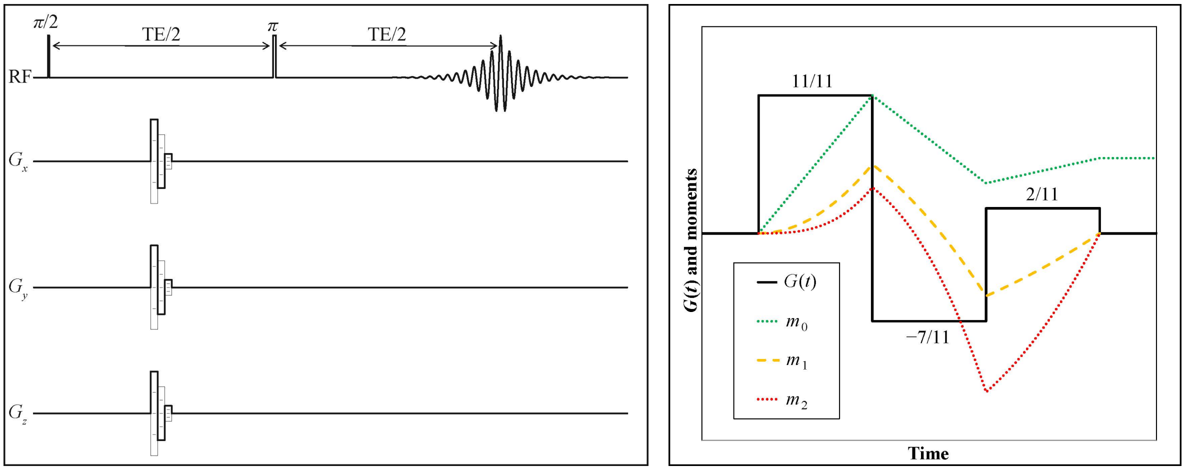

(a) (b)

Figure E.2: Spectroscopic imaging pulse sequence (a) with gradient moment nulling [7] (b) for both velocity (m_1) and acceleration (m_2) compensation. Four 200 ms acquisitions are averaged and zero-filled to 400 ms, per phase-encode cycle.

Approach

A chemical shift imaging (CSI) pulse sequence with velocity and acceleration compensation was employed (Figure E.2). HP ^{129}Xe is premixed with DME and combines with oxygen at a flame that is contained inside of a water-cooled, four foot long ceramic tube that thermally isolates it from the bore of the magnet (9.4 T). A smaller ceramic tube contains the flame itself and protects the 15 mm RF coil (coated with mica tape) from the direct flame (Figure E.3). Initial studies were performed with mullite tubes before switching to 99.8% alumina (Figure E.4). Shimming is performed at room temperature prior to ignition using a continuous sparking mechanism lowered into the tube while it is inside the magnet.

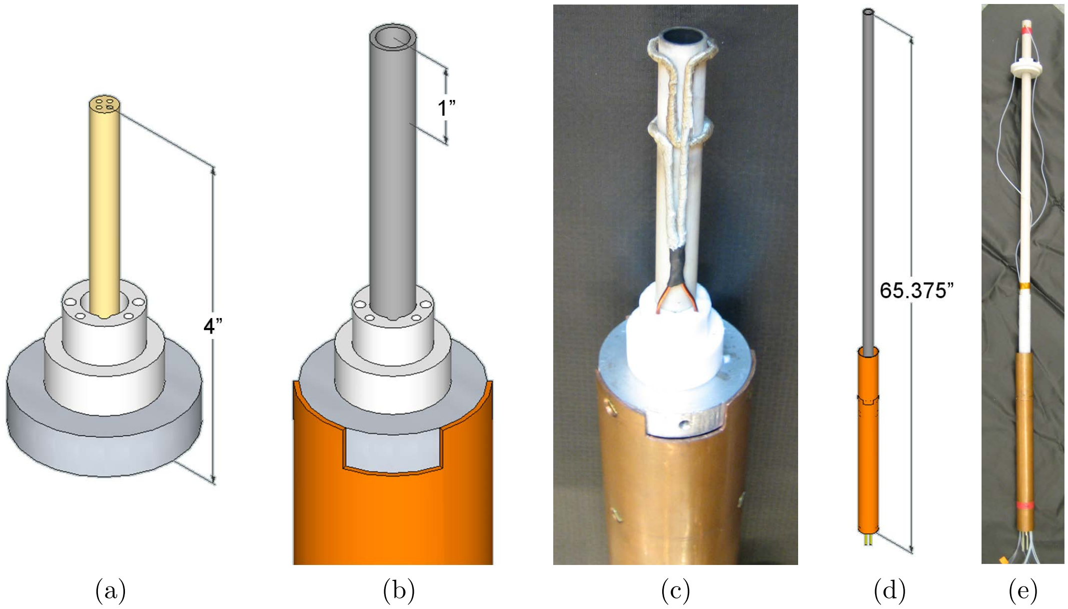

(a) (b) (c) (d) (e)

Figure E.3: A diffusion flame begins where premixed Xe/DME meets with oxygen at the top of a four-bore alumina tube (a). A second alumina tube protects the coil and contains the flame (b)-(c). The larger water-cooled ceramic tube is also shown (d)-(e). Flow rates for Xe, DME, and oxygen are approximately 0.30, 0.05, and 0.14 standard liters per minute respectively. Purging nitrogen gas helps to clear the larger ceramic tube of exhaust and assists in the cooling process.

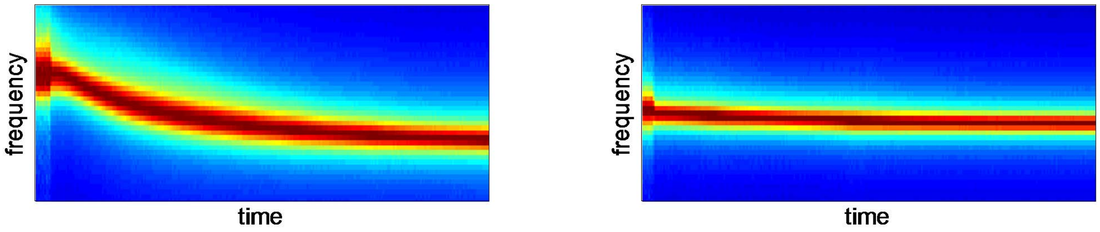

(a) (b)

Figure E.4: Acquisition during five minutes of cooling (flame extinguished at 10 seconds) demonstrates that the use of less-expensive mullite tubes containing 0.5% iron oxide (a) leads to magnetic susceptibility effects on the Xe chemical shift and linewidth, which are minimized with alumina tubes containing 20 times less iron oxide (b).

Results

^{129}Xe images and chemical shift-encoded images of ^{129}Xe with and without active combustion were acquired (Figure E.5). Two-dimensional phase-encoded images (9 × 9) take approximately 2.5 minutes to acquire. Three-dimensional CSI and velocity imaging are possible and are currently being investigated. This method can be applied to imaging of confined processes, such as smoldering combustion, and remotely-detected imaging of microscale combustion processes including flames in microfluidic channels, miniature turbines and rocket nozzles [18]. These devices are of interest because they have power densities far greater than conventional batteries, and are an alternative to fuel cells for portable power applications based on hydrocarbon fuels instead of chemical batteries.

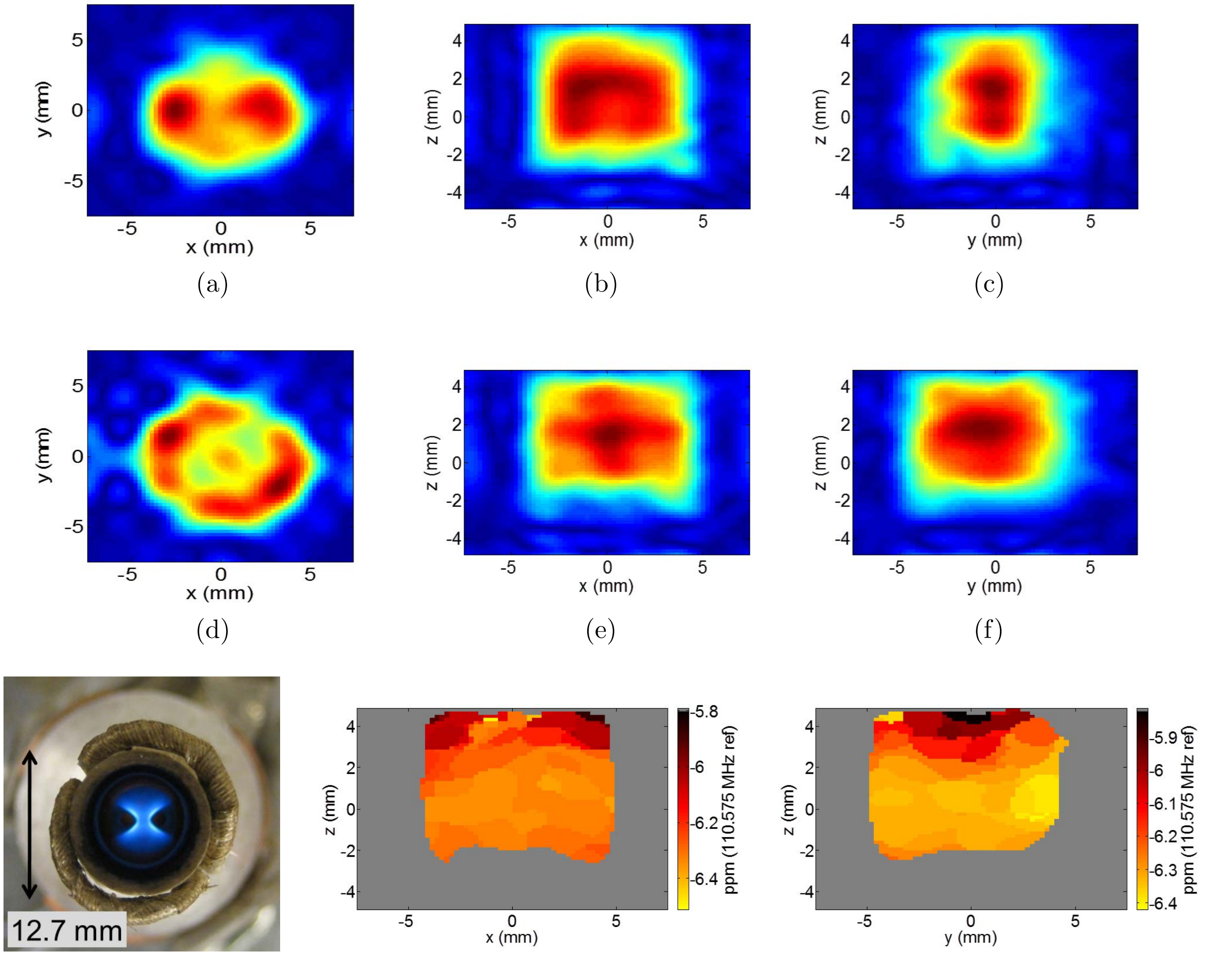

(a) (b) (c)

(d) (e) (f)

(g) (h) (i)

Figure E.5: (a),(d) Axial ^{129}Xe images before and during combustion. (g) An axial photograph of the homebuilt coil outside of the 12.7 mm ceramic tube containing the flame ($\sim$ 20 mm in height, blue). Channels along the horizontal (x) and vertical (y) axes deliver Xe/DME and oxygen respectively. (b),(c);(e),(f) Coronal and sagittal ^{129}Xe images before and during combustion. (h),(i) Coronal and sagittal chemical shift-encoded images indicating increasing chemical shift with height along the flame. All images were zero-filled to 64×64 prior to Fourier transform.

E.3 EUROMAR 2011

E.3.1 Abstract

"CSI and Velocimetry of Enclosed Diffusion Flames Using HP ^{129}Xe"
-Submitted July 20, 2011

There is considerable interest in new methods to probe the chemistry and thermodynamics of enclosed combustion processes. Hyperpolarized (HP) ^{129}Xe gas MRI enables sensitive and noninvasive analysis of chemical composition and velocity [27] within opaque samples. By taking advantage of both the temperature sensitivity of the chemical shift [1] as well as the inertness of ^{129}Xe, temperature and velocity distribution images of an enclosed flame can be acquired. Previous attempts to analyze high-temperature combustion reactions using NMR employed 2D-EXSY [1] of HP ^{129}Xe and SPRITE [22] proton imaging. In the present study, a homebuilt, water-cooled probe was fabricated, including electronics that are able to withstand high temperatures (> 2000 K). HP ^{129}Xe is premixed with a combustible gas (methane or dimethyl ether) and meets with pure oxygen at an enclosed diffusion flame centered within a 15×25 mm insulated coil. A spin echo pulse sequence with velocity and acceleration compensated phase-encodes, is used to generate temperature-weighted, 3D chemical shift images (CSI) as well as 3D velocity maps of the flame region. This technique can be applied to studying confined combustion processes such as microturbine engines on MEMS devices.

E.3.2 Poster

"CSI and Velocimetry of Enclosed Diffusion Flames Using HP ^{129}Xe"
-Presented at: EUROMAR 2011 Conference, Frankfurt, Germany. August 21-25, 2011 (Poster 263); won Poster Award

Abstract

There is considerable interest in new methods to probe the chemistry and thermodynamics of enclosed combustion processes. Hyperpolarized (HP) ^{129}Xe gas MRI enables sensitive and noninvasive analysis of chemical composition and velocity [27] within opaque samples. By taking advantage of the both the temperature sensitivity of the chemical shift [1] as well as the inertness of ^{129}Xe, temperature and velocity distribution images of an enclosed flame can be acquired. Previous attempts to analyze high-temperature combustion reactions using NMR employed 2D-EXSY [1] of HP ^{129}Xe and SPRITE [22] proton imaging. In the present study, a homebuilt, water-cooled probe was fabricated, including electronics that are able to withstand high temperatures (> 2000 K). HP xenon is premixed with a combustible gas and meets with pure oxygen at an enclosed diffusion flame centered within a 15 (ID) $\times$ 25 (H) mm insulated saddle coil. A spin echo pulse sequence with velocity and acceleration compensated phase-encodes, is used to generate temperature-weighted, 3D chemical shift images (CSI) as

well as 3D velocity maps of the flame region. This technique can be applied to studying confined combustion processes such as microturbine engines on MEMS devices.

Background

The ability to easily acquire temperature and velocity information from high-temperature combustion reactions would enable improvements in devices that utilize enclosed flames, such as microturbines used to power MEMS devices. However, commonly used techniques for imaging these reactions have limitations which prevent non-invasive imaging of enclosed flames (FLIR: surfaces only; ultrasound: solid phase only; fluoroscopy: invasive; thermocouples: 1D and invasive; particle velocimetry: open flames only). The wealth of information available in magnetic resonance spectra can be used to reconstruct temperature and velocity maps of enclosed combustion reactions. Gas NMR is difficult due to the low spin density of the commonly-used ^{1}H and ^{13}C nuclei. By employing the inert nucleus HP 129Xe as a tracer, with polarizations 10,000 times above thermal levels, we can learn information about the reaction from the effects it has on ^{129}Xe. The chemical shift of ^{129}Xe is temperature-dependent, and using pulse sequences optimized for flowing systems, both temperature and velocity maps can be generated from the MRI datasets.

Approach

The diffusion flame burns at the outlet of a four bore alumina tube. Methane premixed with HP ^{129}Xe is delivered from opposite bores and meet with pure oxygen at the flame (Figure E.6a). A probe was fabricated that could not only withstand the high flame temperatures (approaching 2000 °C), but also had an optimal filling factor for the flame. A saddle coil wrapped in high-temperature mica tape was wound around an alumina tube that contains the flame, and is connected to tuning electronics which are isolated from the flame (Figure E.6b). A four foot long alumina stack is used to insulate the flame from the magnet and employed both water and air cooling. Pure alumina was used due to the temperature-dependent magnetic susceptibility effects observed with mullite (Figure E.6c, E.6d). Due to the rapid flow through the coil, a purely phase-encoded pulse sequence was required. To acquire information about both the chemical shift and velocity, pulses with gradient moment nulling were employed (Figure E.7). Total encoding time was kept to a minimum so that readout could occur while the spins were still well within the coil.

CSI Results

Three-dimensional ^{129}Xe chemical shift images were generated using the data with no velocity-encoding gradients applied. The reference was set to the room temperature xenon frequency (i.e. no oxygen or methane present). The addition of oxygen and methane, and concomitant decrease in xenon, leads to a downfield shift (Figure E.8a). When the flame is lit, there is an upfield shift in the warmer, lower region of the flame and the CSI results in a qualitative temperature map.

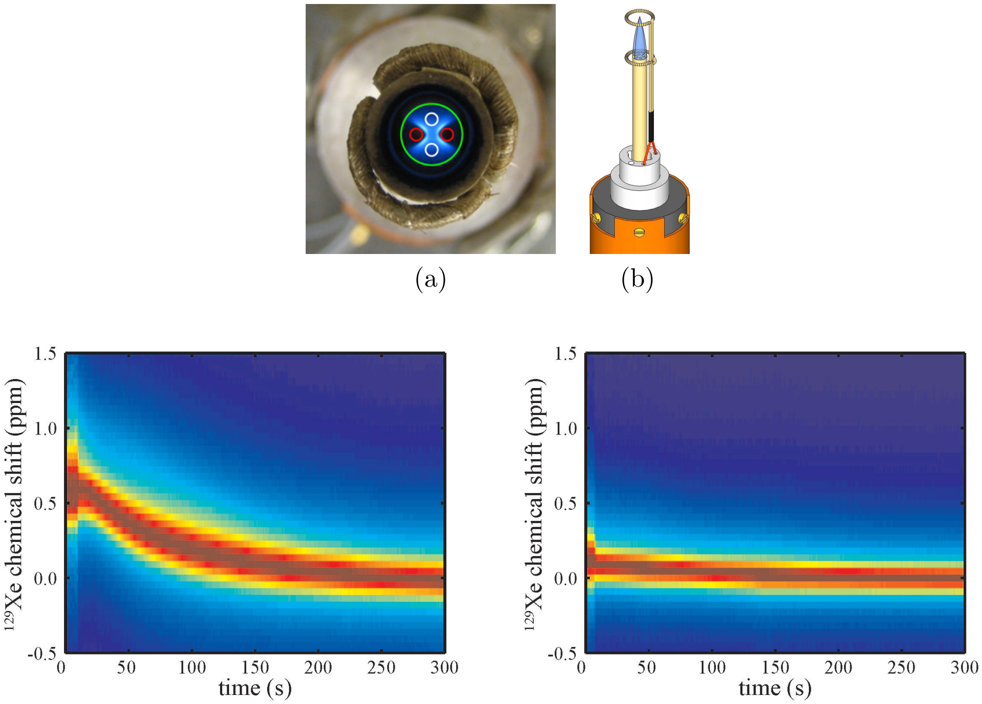

(a) (b)

(c) (d)

Figure E.6: (a) A picture of the flame at the outlet of the four-bore tube, the outline of which has been added in green. A mixture of HP ^{129}Xe and fuel (red) meets with pure oxygen (white) here. (b) A drawing of the probe detailing the coil, a 15 (ID) × 25 (H) mm mica tape insulated saddle. Not shown are the two alumina tubes surrounding the flame and coil. (c) Cooling curve of the chemical shift with mullite tubes present. (d) Cooling curve after changing all ceramic tubes to 99.8% alumina.

Velocimetry Results

Through application of bipolar velocity gradient lobes of appropriate strength, the full velocity space can be imaged without aliasing. The x, y, and z velocity was determined at each point of both the unlit and lit flame. Calculated velocities fell in the range of $\approx \pm 300$ cm s^{-1}, correlating well with predictions based on flow rates. The subtracted velocity images (lit flame minus unlit jet) are presented in Figure E.9. As shown, the greatest increase in velocity is found in the lower region of the flame, where the upward ($+z$) velocity increase dominates.

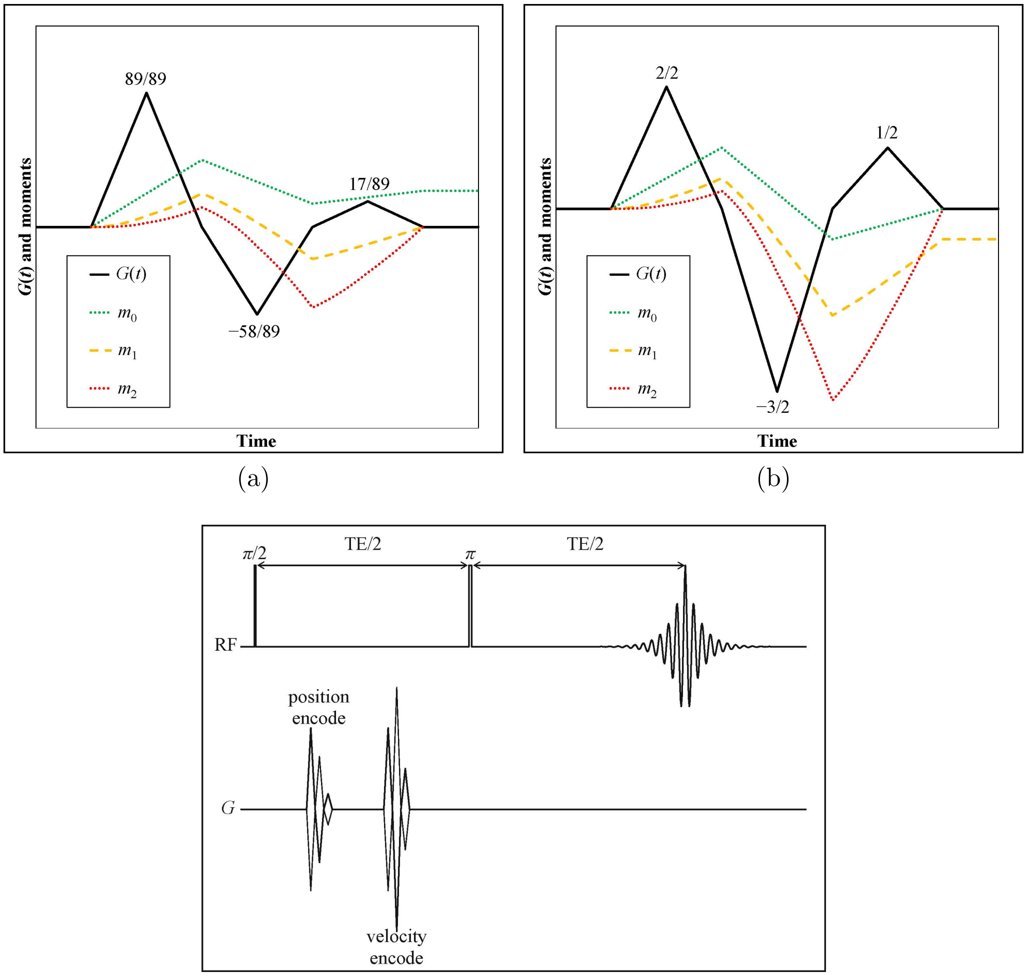

(a) (b)

(c)

Figure E.7: Gradient moment nulling triangular lobe ratios for: (a) position-encoding (m_0) with velocity (m_1) and acceleration (m_2) compensation and (b) velocity-encoding with position and acceleration compensation. The full pulse sequence (c) is a purely phase-encoded spin echo with a TE of 8 ms. The spins travel through the coil in approximately 100 ms. Total gradient durations for the two lobes in the data presented here are 480 µs and 600 µs respectively. A full phase cycle at each point of the $9 \times 9 \times 17 \times 3 \times 3$ k-space is acquired in less than 7 hours ($nt = 4$, TR $= 500$ ms).

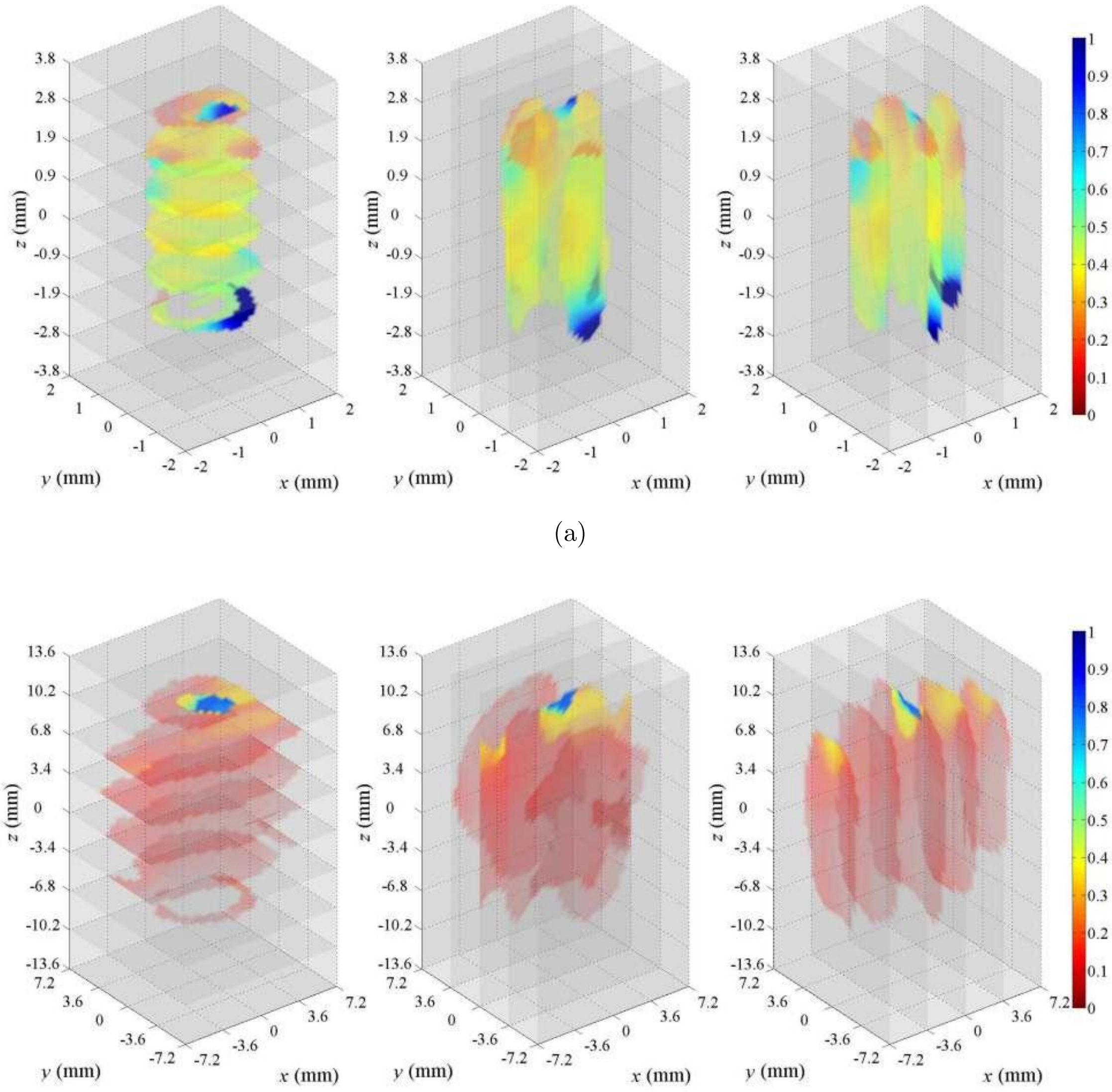

(a)

(b)

Figure E.8: Axial, coronal, and sagittal slices of the 3D ^{129}Xe CSI of the unlit (a) and lit (b) methane flames. The unlit image was acquired with all gases flowing (HP ^{129}Xe, CH_4, O_2). Chemical shift (δ) reference is room temperature xenon alone (110.574 MHz). Data are first apodized and then zero-filled from $9 \times 9 \times 17$ to $33 \times 33 \times 65$ prior to Fourier transform.

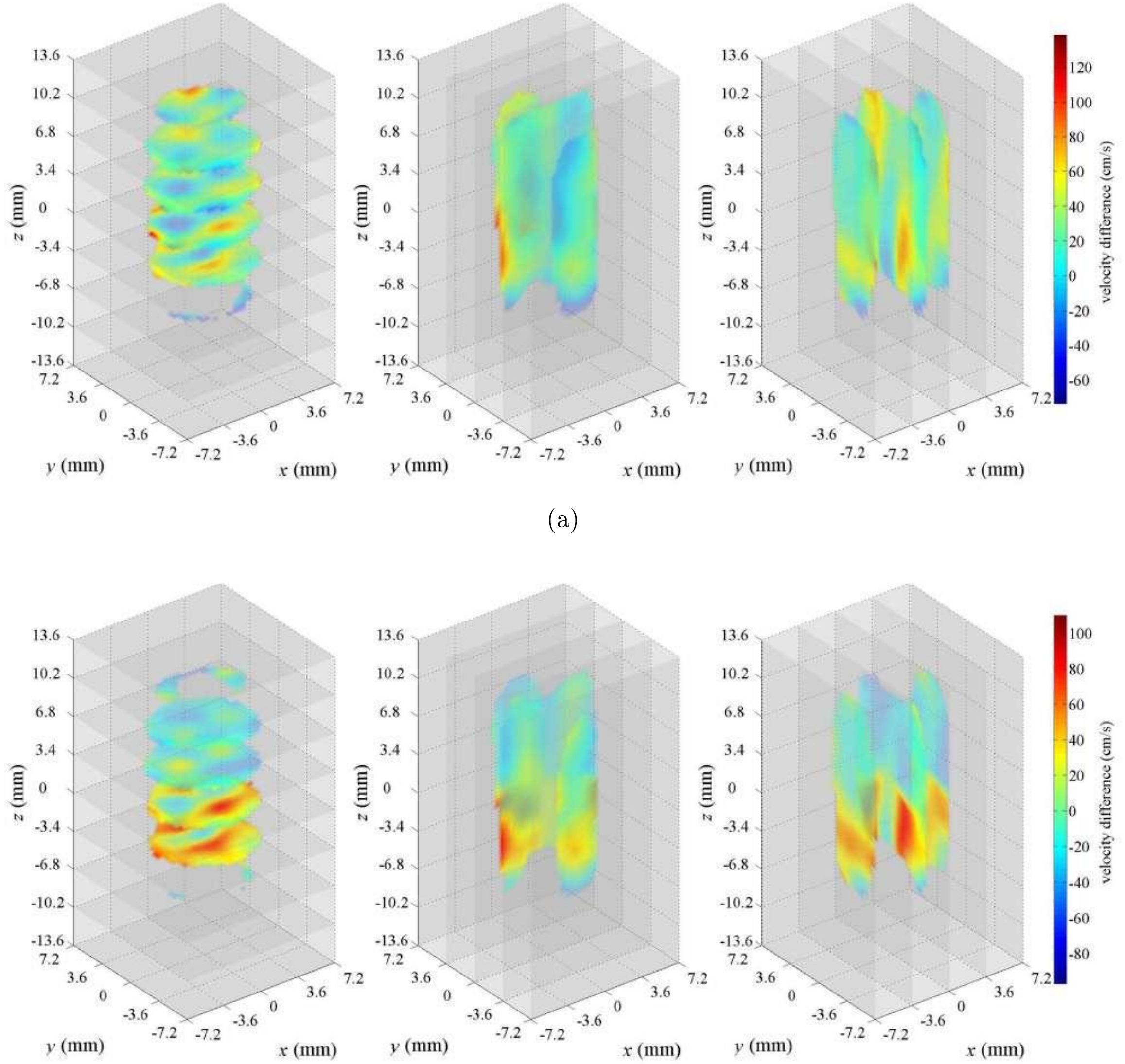

(a)

(b)

Figure E.9: Slices of the velocity difference (lit minus unlit) images: (a) difference in velocity along the z-axis, (b) difference in total (scalar) velocity. Calculated velocity was subtracted at each point of the zero-filled data set. Red indicates an increased velocity when the flame is lit; blue a decrease.